Development of A Hybrid Wind-Wave Energy Converter to Enhance Power Output and Efficiency

Sadegh Khaleghi

A thesis submitted to

Auckland University of Technology

in fulfilment of the requirements for the degree of

Doctor of Philosophy (PhD)

April 2022

Department of Electrical and Electronic Engineering

Abstract

Airflow rate has a significant impact on the performance of oscillating water column (OWC) wave energy converters (WEC). A novel method is proposed in this work that improves airflow rate and output power by integrating a mechanical component referred to as a windcatcher with a conventional OWC or known as a hybrid OWC. A non-linear two-dimensional computational fluid dynamics (CFD) approach is used, together with the Reynolds Averaged Navier-Stokes (RANS) technique, to explore the hydrodynamic performance of the proposed system. Simulation studies are conducted and the results of the proposed hybrid OWC are superior in terms of airflow rate and output power compared to a conventional design. Furthermore, as the amplitude of the oscillatory element of the turbine airflow rate is reduced, the results reveal a consistency in generating power in the proposed hybrid OWC system. As a result, the proposed hybrid OWC converter produces much more power than a conventional model.

There are two parts to this study. The results of the first part of the study reveal that the geometry of the proposed system is not perfect, and there is a discrepancy between the simulation result and the maximum turbine airflow rate, which is the sum of wind and wave airflow rate. As a result, the geometry should be modified to achieve optimum turbine airflow rate. Therefore, the effect of changing key geometric variables such as turbine height, orifice width, and orifice output angle on the performance of the proposed hybrid system is analyzed in the second part of this study. The turbine flow rate, chamber pressure, orifice flow rate, and turbine power output are selected to monitor the performance of the proposed system under different geometrical situations. Eventually, the values of the chosen geometrical parameters at which the proposed system achieves the best performance indicators are determined.

ATTESTATION OF AUTHORSHIP

I hereby declare that this submission is my work and that, to the best of my knowledge and belief, it contains no material previously published or written by another person (except where explicitly defined in the acknowledgements), nor material which to a substantial extent has been submitted for the award of any other degree or diploma of a university or other institution of higher learning.

Signature

Sadegh Khaleghi

Acknowledgements

I would like to thank my supervisors Professor Tek Tjing Lie, Dr Craig Baguley and Professor Sascha Kosleck for their help and advice with this PhD. My gratitude extends to the Faculty of Design and Creative Technology for the funding opportunity to undertake my studies at the School of Engineering, Computer and Mathematical Science, Auckland University of Technology. Additionally, I would like to express gratitude to Prof. Sascha Kosleck for his treasured support which was influential in shaping my theoretical methods and critiquing my results. I would like to thank my friends, lab mates, colleagues and research team for their help and support. My most sincere appreciation also goes to my partner, without her tremendous understanding and encouragement in the past few years, it would be impossible for me to complete my study.

Table of Contents

List of Tables

List Of Figures

Nomenclature

Acronym	Description
A	wave height applied at the inlet boundary (m)
A_1	area of the inlet of windcatcher (m^2)
A_2	area of the outlet of the windcatcher (m^2)
A_e	the effective area of the opening (m^2)
A_r	reference area (m^2)
b	chamber length (m)
b_s	system width (m)
C_{Abs}	the OWC energy absorption
C_d	coefficient of discharge of the opening in the windcatcher
c_g	celerity
$C_{Internal}$	the OWC internal energy extraction
C_L	energy losses
$C_{Overall}$	overall pneumatic energy extraction
C_p	the difference in the pressure coefficient of the air between both the inlet and the outlet of the windcatcher
C_R^2	reflected energy
C_S	the OWC stored energy
CFD	computational fluid dynamic
C_R	wave reflection coefficient
CWR	capture width ratio
D	the outside diameter of the turbine rotor (m)
D_ω	cross-diffusion term
D_ω^+	the positive portion of the cross-diffusion term
E_A	quantity of wave energy received by the OWC structure (J m^{-1})
E_E	energy converted to electricity from the turbine (J m^{-1})
E_I	amount of energy accessible in the approaching waves (J m^{-1})
E_i	overall wave energy

Acronym	Description
E_L	energy losses in the conversion cycle (J m^{-1})
E_R	energy reflected waves by the solid structural elements (J m^{-1})
E_S	energy collected within the chamber (J m^{-1})
E_S'	instantaneous potential energy accumulated in OWC heave oscillation (J m^{-1})
f_w	turbine's geometry characteristic
f_P	turbine's geometry characteristic
FE	finite element
g	gravitational force (m s^{-2})
G_k	the kinetic energy produced by turbulence
$\tilde{G}_k$	production of turbulence kinetic energy caused by mean velocity gradients
G_ω	creation of a specific dissipation rate (ω)
h	specific enthalpy (J kg^{-1})
H	incident wave height (m)
h_t	enthalpy at the turbine outlet (J kg^{-1})
H_R	reflected wave height (m)
H_w	height of the water column oscillation (m)
h_w	water depth (m)
I	unit tensor
K	loss coefficient
k	turbulence kinetic energy
L	incident wavelength (m)
L_b	length from the opening to the bottom (m)
LES	large eddy simulation
L_T	length of the opening segment of windcatcher (m)
L_v	power loss due to viscous causes in the turbine and its connecting ducts
m	the instantaneous value of mass
M-OWC	multi-oscillating water column
$\dot{m}_{pq}$	mass transfer from phase p to phase q

Acronym	Description
$\dot{m}_{qp}$	mass transmission from phase q to phase p
N	rotational speed (rad s^{-1})
OE	ocean energy
OWC	oscillating water column
OWSC	oscillating wave surge converter
P	power output (W)
p	static pressure
p_{cr}	critical pressure
P_E	fraction of time-averaged harvested power
p_E	exterior pressure of windcatcher
p_{hyd}	hydrodynamic energy absorbed by the OWC
P_I	incoming wave power (W)
P_i	average incident wave power
p_I	interior pressure of windcatcher
$P_{orifice}$	power at the orifice
p_t	the pressure differential
PTO	power take-off
p_v	pressure loss at the valve
p_w	wind pressure
$q(t)$	airflow rate through the turbine ($m^3 s^{-1}$)
$q_{OWC}(t)$	airflow rate provided by the OWC ($m^3 s^{-1}$)
$q_{windcatcher}(t)$	airflow rate provided by the windcatcher ($m^3 s^{-1}$)
R	air specific gas constant
RANS	Reynolds averaged Navier-Stokes
RSM	Reynolds stress model
S	strain rate magnitude
s	specific entropy (J kg^{-1} K^{-1})
S_m	mass delivered to the continuous phase from the distributed second phase

Acronym	Description
SST	shear-stress transport
T	absolute temperature
T_s	the temperature of the thermodynamic state in which its pressure is equal to the pressure $p_t + p_a$ at the turbine outlet and its specific entropy is equivalent to that of the surrounding ambiance
T_w	wave period
u	specific internal energy (J kg^{-1})
u_{in}	velocity within the quadrants of an input tube
u_{out}	velocity within the quadrants of an output tube
u_w	Inlet air velocity of windcatcher (m s^{-1})
$\overline{u}_i$	mean velocity components
u_i'	fluctuating velocity components
v_H	velocity at the windcatcher's top wall
v_r	radial velocity
v_x	axial velocity
WEC	wave energy converter
w_v	the flow rate through the valve (kg s^{-1})
y	distance to the adjacent surface
Y_k	turbulence-induced dissipation of k
Y_ω	turbulence-induced dissipation of ω
z_I	elevation of the entry to the windcatcher from the chamber, relative to the bottom surface of the chamber (m)
α^*	turbulent viscosity, resulting in a low-Reynolds-number adjustment
αA_r	the valve's useful area of entry
β	the angle formed by the incident wave's direction and the positive direction of the x-axis
Ψ	dimensionless pressure coefficient
η	vertical oscillation of the water volume relocated from the still water level
$\dot{\eta}$	the OWC's vertical velocity

Acronym	Description
Γ_k	effective diffusivity of k
Γ_ω	effective diffusivity of ω
ε	turbulence dissipation rate
ε_{hyd}	efficiency of system
Φ	dimensionless flow coefficient
$\phi(x,y,z)$	total velocity potential
φ_0	velocity potential for a rising wave due to the flat coastline without the device's regional topography
φ_S	velocity potential of the waves
μ	molecular viscosity
μ_t	turbulent viscosity
ω	angular frequency of the wave (rad s^{-1})
$\prod$	dimensionless power coefficient
Δp_{in}	pressure loss across the windcatcher quadrant
Δp_{out}	pressure loss across the exit quadrant
$\Delta P(t)$	instantaneous differential pressure
ρ	water density (kg m^{-3})
$\overline{\rho}$	average density value across the length of the quadrant
ρ^*	standard density
$-\rho\overline{u_i' u_j'}$	Reynolds stresses
θ	the angle of the air inlet of the windcatcher
$\overline{\tau}$	stress tensor
σ_k	turbulent Prandtl numbers for k
σ_ω	turbulent Prandtl numbers for ω

Chapter: 1 Introduction

This chapter will present the motivation and objectives of the study. In addition, it will also explain the broad goal of this research endeavour, as well as its scope and significance.

1-1- The rationale of the Study

Ocean waves are a clean energy resource with the potential to make a significant contribution to the global energy demands as progress is made toward a more sustainable world. A key attraction is the predictability of energy supply, which is advantageous in terms of stabilizing electrical grids compared to less predictable solar and wind energy resources. **Error! Reference source not found.** depicts the theoretical potential of wave energy for different regions. However, the potentially useable wave energy capacity on a global basis is estimated to be between 2000 and 4000 TWh/year [1], which is far less than the global theoretical potential of wave energy (29500 TWh/year) shown in **Error! Reference source not found.**. This reveals that marine energy development is still in its infancy, specifically in the context of wave power. Therefore, it is vital to develop a framework to efficiently capture and harvest the energy delivered by the waves. Another important issue is the need for proper construction to survive in the sea environment, especially in storm situations where the wave power increases dramatically. Floating equipment capable of being installed offshore has been introduced in recent decades. The systems can be designed and optimized to take advantage of both potential and kinetic energy, either separately or simultaneously [2]. The future of this industry is difficult to forecast since there are no large-scale wave farms; however, as technology advances, new chances to develop wave energy harvesting become available [3].

Table 1-1: Wave energy potential around the world [4].

Regions	Wave energy potential (TWh/year)
New Zealand, the Pacific Islands, and Australia	5600
Asia	6200
South America	4600
North America and Greenland	4000
Africa	3500
Western and Northern Europe	2800
Central America	1500
The Mediterranean Sea and Atlantic Archipelagos	1300
Total	29,500

Error! Reference source not found. depicts the total wave power distribution for distinct coastal habitats, as reported by the National Oceanic and Atmospheric Administration's Wave Watch III data [5]. As shown by these statistics, sites in North America have more wave energy potential than sites in Europe, even though this region conducts the majority of wave energy converter (WEC) studies. From **Error! Reference source not found.** it is apparent that the power that can be extracted from wave energy is greatest around Australia, followed by the United States and Chile, with Portugal and France having substantially smaller values.

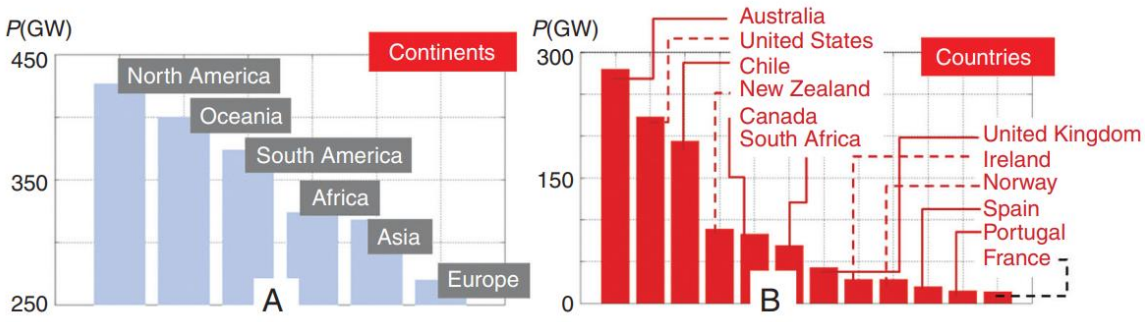

Figure 1-1: Figure Estimated yearly means wave power for (a) continents and (b) countries [5].

The development of novel solutions that enhance the performance of existing WEC technologies is the aim of this research. The WEC has a lot of opportunities for boosting energy conversion and benefiting society while lowering the carbon footprint and preventing additional damage to the ecosystem. Unlike solar energy, which is dependent on clear weather, and wind energy, which is hard to anticipate and requires a large area of space, wave energy is a constant source that can be incorporated into other systems.

1-2- Offshore Energy Convertors

Offshore Renewable Energy has a great potential to play a major role in supplying the energy demand and facing climate change impacts. There are different types of offshore energy converters including wind and wave energy and each category has different models based on the type of generation, foundation, and type of transmission. In this section, a complete overview of offshore wave and wind energy including different types, current possibilities for improvement and the main challenges are discussed.

1-2-1- Offshore Wave Energy Converters

Wave energy converters (WECs) transform the kinetic and potential energy generated by a passing wave into practical mechanical or electrical energy that can be used for a variety of applications range of applications. These range from the supply of clean energy to the electrical grid to pumping for saltwater desalination. The methods employed for wave energy conversion are numerous, as evident

from the knowledge that 1000 patents in the area exist worldwide [6]. The first WEC was invented in France, and the first WEC patent was acquired in 1799. Yoshio Masuda invented the predecessor of contemporary wave energy systems in Japan in 1940 [6].

Error! Reference source not found. defines various types of WECs based on their operating characteristics and operating location, which can be onshore, nearshore, or offshore. As shown, WECs are classified into eight main categories, namely: “attenuator, point absorber, oscillating wave surge converter, oscillating water column, overtopping/terminator device, submerged pressure differential, bulge wave, and rotating mass”. The only model which is most prevalent in onshore systems is the oscillating water column in which the air is trapped in a semi-submerged cylinder and compressed to cause rotation of a turbine and produce power as a result [7]. In the following paragraph, the mechanisms of each WECs technology in harvesting energy will be discussed in more detail.

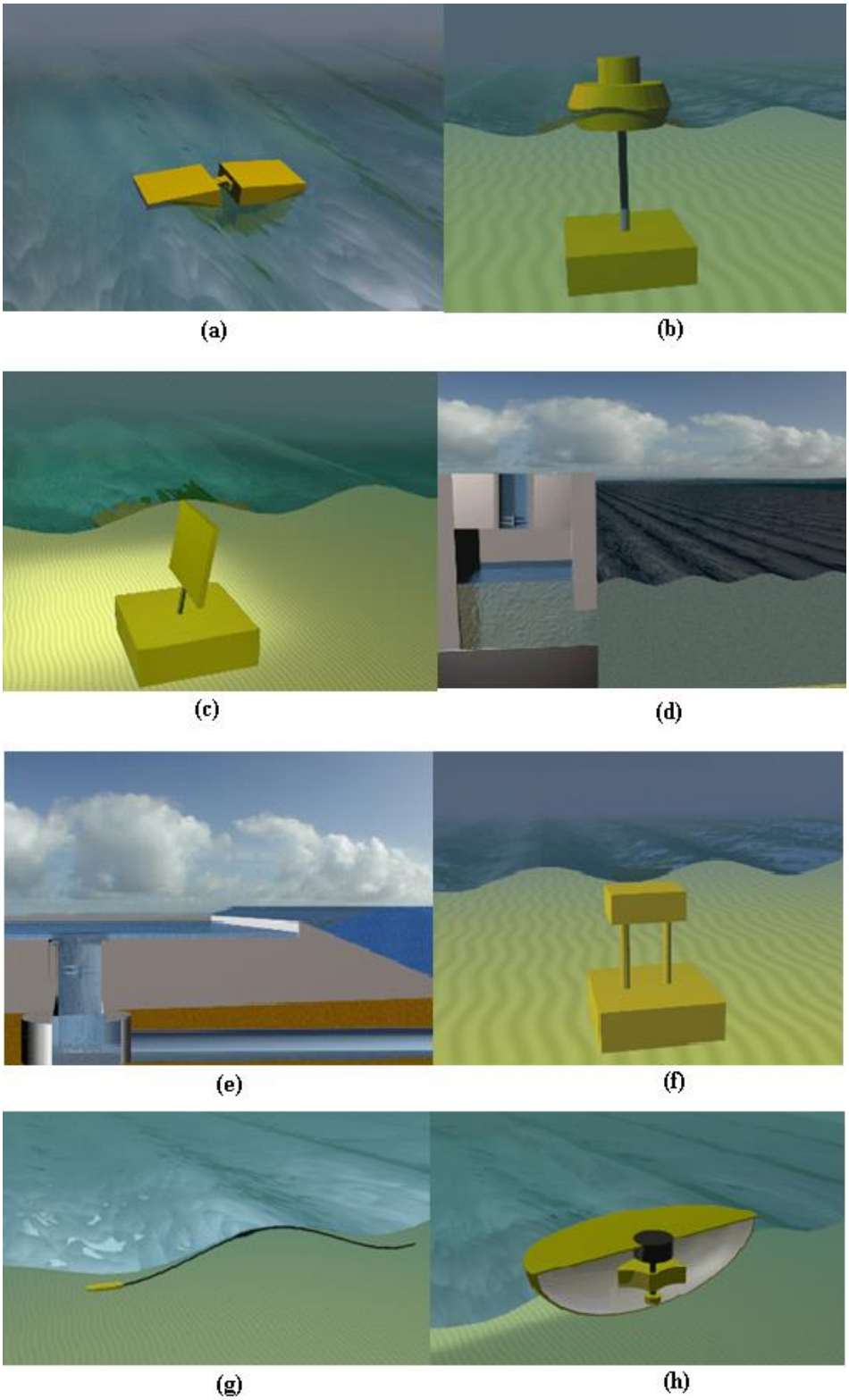

Figure 1-2: Main classifications of WECs: (a) attenuator, (b) point absorber, (c) oscillating wave surge converter, (d) oscillating water column (OWC), (e) overtopping device, (f) submerged pressure differential, (g) bulge wave, (h) rotating mass [8].

1-2-1-1- Attenuator

Error! Reference source not found. a shows the schematic of an attenuator device. The attenuator is a piece of floating equipment that runs parallel to the axis of the wave and harvests energy when passing waves resulting in a difference in velocity between the two arms. The initial commercial form of this mechanism looks like a snake called Pelamis Wave Power and can have a total length of 150m with a rated power of 750kW and can be installed in water depths more than 50m [9].

The current commercial Pelamis wave energy converter farm which has 22.5MW output power can be considered the first commercial offshore wave energy converter and has 120m long and 3.5m wide and wights 750t the first phase of the project was installed in 2008 in Portugal [10].

1-2-1-2- Point absorber

As shown in **Error! Reference source not found.**b, the point absorber is equipment with a smaller size compared to the wavelength. The pressure difference allows the floating structure to be lifted and down on the water's surface or immersed beneath the water's surface. This type of converter can absorb wave energy in all directions and they install offshore at the surface of the water. The first commercial project consisted of 12-21 floater heaving floaters and to generate the power it was connected to a hydraulic system which converts vertical motion into a rotational movement that drives the hydraulic system [11].

1-2-1-3- Oscillating wave surge converter

Oscillating wave surge converters are presented in **Error! Reference source not found.**c. The oscillating wave surge converter typically has a hinged deflector perpendicular to the axis of the wave and slides back and forth, taking advantage of the wave's horizontal particle motion. In reaction to the movement of the waves, the arm fluctuates as a pendulum on a pivoting connection. One of the commercial scale projects is Oyster 800 which is a nearshore wave energy device and can be deployed to up to 15m of water depth with an output power of 800kW [12].

1-2-1-4- Oscillating water column (OWC)

Error! Reference source not found.d depicts the schematic of an OWC. The oscillating water column (OWC) is a partly immersed cylindrical construction, which is accessible to the ocean under the water's

surface, confining a cylinder of air on top of a column of water. The water column rises and falls as a result of the waves, which compresses and decompresses the air column. This confined air is permitted to flow to and from the atmosphere through a turbine, which may normally revolve in either direction regardless of the airflow. The turbine's spin is utilized to create power.

1-2-1-5- Overtopping/terminator device

As shown in **Error! Reference source not found.**e, the overtopping device collects ocean water from incident waves in a reservoir above the ocean surface. The water is subsequently discharged to the ocean via a typical low-head turbine that produces electricity. The low-head turbines are types of turbines that generate hydroelectric energy when the water's head is less than 20 meters, approximately [8]. To concentrate the wave power, the overtopping mechanism might additionally employ collectors.

1-2-1-6- Submerged pressure differential

An illustration of the submerged pressure differential mechanism is shown in **Error! Reference source not found.**f. This type of WEC is a submerged point absorber that employs the pressure difference between wave crests and troughs above the system. It is made up of two primary parts: a fixed seabed air-filled cylindrical chamber and a mobile top cylinder. The water pressure above the equipment presses the air inside the cylinder as a wave crest passes over it, pushing the top cylinder down. The water pressure on the equipment (i.e., submerged pressure differential) decreases as a trough passes over it, while the higher cylinder lifts. This equipment has the benefit of not being vulnerable to the harmful knocking stresses experienced by floating devices, as well as having a lower visual effect.

1-2-1-7- Bulge wave

Error! Reference source not found.g depicts the bulge wave technique, which comprises a water-filled rubber tube tethered to the seabed and oscillating in the waves. Water flows into the tube through the stern, and the incoming wave generates pressure fluctuations down the length of the tube, resulting in a 'bulge.' As the bulge moves down the tube, it gathers energy that can be employed to power a typical low head turbine at the bow from which the water is subsequently returned to the ocean.

1-2-1-8- Rotating mass

Error! Reference source not found.h shows the schematic of a rotating mass device. Two types of

rotation are employed to gather energy from the movement of the hemisphere (as shown in **Error! Reference source not found.**h) in the waves, surging and oscillating. Linear acceleration is caused by the motion of an uneven mass or a gyroscope. In both situations, the motion is linked to an electricity generator located within the equipment.

To create an overall perspective, the previous sub-sections provided a brief illustration of different categories of WECs. However, among the discussed classifications, this study focuses mainly on the OWC system; thus, previous research will be reviewed in the following sections.

1-2-2- Offshore Wind Energy Converter

The first industry-scale offshore wind converter installed in Denmark with around 5MW output power encompasses 11 turbines. The increase in deployment of offshore converters was mainly in the vicinity of Europe and other countries just started in 2010 [13]. The world installation capacity is led by China having 6.1GW of offshore wind in 2020 and this year was the highest year for offshore installation, but offshore wind today is only 2% of what is forecasted to get to net zero by 2050. Europe still experiencing the highest growth in installing offshore energy conversion technology from 1.5GW in Netherland to around 700MW Belgium and UK and Germany have an installed capacity of 483 and 237MW respectively. Statical data in [14] confirms that the global offshore market grew by around 22% each year which led to around 35GW of offshore wind installation and Europe remains the largest offshore market by 70% and North America only has 42MW capacity of offshore converters.

One way to categorize different offshore wind energy converters is based on types of generators: DFIG, SCIG and SPMG [15]. DFIG works based on a frequency converter and has a working principle similar to synchronous conventional generators, but more maintenance is required for this type. The rotor of the SCIG has a few copper or aluminium bars which makes this type of generator more reliable and robust. Lastly, the SPMG have the highest number of poles among all types, and they might have no gear.

Another way to categorise offshore wind converters is based on the type of transmitting the output power to shore. Generally, there are three types of transmission systems of HVAC, HVDC-LCC and

HVDC-VSC. An onshore substation with transformers and other assets is needed for HVAC and the problem with this system is that the voltage drops for long distances. HVDC-LCC consists of an offshore substation, DC cables for power transmission and an onshore converter station one advantage of this transmission system is that distance has no negative effect on voltage drop. HVDC-VSC uses the technology of IGBT, and GTO converter and the working principle is very similar to HVDC-LCC.

Having the right and reliable foundation is another necessary part of an offshore energy converter to prevent damage during harsh weather conditions and to ensure that the device can work in a stable working environment. The main foundation types can be categorized into three main types gravity base, monopiles and tabular metallic foundations. Gravity base foundation needs a complete phase of seabed preparation and because of that, they cannot be used for water depth deeper than 10m. This type of foundation relies on the weight of the device and structure which can provide reliable support during bad weather conditions. The monopile type uses a single deep metal foundation that should be placed in the seabed. Seabed preparation is not necessary, and this type can be used up to 30m of water depth. A tabular metallic foundation uses three or four legs installed at a depth higher than 20m in the seabed. Among all foundation types, monopiles can be considered the most popular and used more than others.

Another important parameter that should be considered in the design stage is choosing the right area of deployment. In general, there are three main types of suitable, excluded areas and suitable areas with environmental constraints. Suitable areas are the most suitable areas to install and use offshore energy converters with less environmental impact. Another type is excluded areas which should be excluded from installation because of the risk of high environmental impact and suitable areas with environmental constraints can be used to install offshore plants but a detailed risk assessment analysis is necessary to capture the environmental impact.

In order to boost the deployment of offshore energy conversion, it is very important to show the long-term and short-term price viability for using offshore wind energy converters to encompass the costs, electricity price and tariffs. Having long and short-term scenarios can provide an approximation for cost and carbon tax and address the potential in the coming competitive markets [16]. To create more opportunities to take offshore wind farms to areas and regions where it is impossible to be directly

connected to the lands, it is important to focus on opportunities of exporting hydrogen from offshore plants. Different levels of cost, net present value and energy expenditure can be captured along with sensitivity analysis on different costs including electrolyzer cost, capacity factor, electrolyzer system efficiency, plant distance to shore and the Levelized cost of electricity [17]. Having offshore wind farms as a practical source of energy requires considering the high maintenance cost as well as the possible conflicts. The possible complexity of interactions between maintenance service and windfarm owners can be challenging and so, focusing on optimizing offshore windfarm contracts can help minimise the possible conflict of interest. One way of analysis is by first evaluating the current state of the contract and introducing a multi-objective based on defining fixed and variable fees under the use of supervisory control and data acquisition (SCADA) systems or online supervising the asset health condition [18]. Some countries have a plan to reach 100% use of renewable energies and to achieve that they use an economic model to increase the offshore energy conversion potential. Analyzing the economic impact of deploying windfarms in Scotland using Input-Output (IO) and Computable General Equilibrium (CGE) to capture both expenditure and operational costs could be a good example of that [19].

One practical concept in economic feasibility is using offshore renewable energies in real-world commercial scenarios like the availability of generation during a day and the price in the market at different hours. Two scenarios are considered in [20] based on the first current generation of 25.2 MW and the second having 150 MW including future development of hydrogen integration. In the first case study, it is considered that hydrogen production is only at night and in the second scenario night and afternoon generation are possible. It is found that higher electricity prices and lower capacity factors ended up having more expensive hydrogen and the second scenario can have lower generation costs because of generating using lower operational and capital costs. One way to capture the cost of power transmission is by considering a 40years lifecycle cost analysis for using infrastructure to transmit the high voltage direct current using 222 km submarine cables considering. The cash flow for a project defined in Bozcaada and Gokce Bozcaada and Gokceadaada in Turkey showed that the project is viable both from cash flow and profit analysis [21].

Showing the viability of using offshore energy converters was the main reason for a scientist to focus

on ways of improving the current technology in this area. One challenging issue in improving the current technologies is found to be layout optimization which depends on design constraints and hydrodynamic interactions. To solve and optimize the offshore converters, numerical modelling and optimization methods have been used and applied to a wide range of case studies including focusing on designing offshore perks, layout optimization techniques, computational intelligence, neural computation, evolutionary computation etc. It is concluded that larger parks could have a higher park effect leading to possible lower performance [22]. Optimizing the placement of offshore converters has been expanded to different types of offshore energy converters including fully submerged buoy-type wave energy converters.

The analysis of output power for an array of buoy converters in a wave farm using a novel multi-swarm cooperative co-evolution algorithm for different cities of Brisbane, Darwin, Sydney, Tasmania and Adelaide showed that the model can improve output power by 2-9% just by optimizing the arrangement [23]. A wide range of research was conducted around the possibility and potential sites for offshore energy conversion using wind speed assessment and wind turbine installation around Iranian islands and results showed great opportunities for islands such as Kharg, Siri and Abu Musa to deploy offshore wind energy and turbine generators [24].

The performance of any type of converter can be improved by improving the design parameters and focusing on optimizing the design parameters before the construction process. The effect of geometry parameters of external support on the hydrodynamic performance of an Oscillating Water Column Wave Energy Converters was investigated numerically and practically and it was concluded that using external support for this type of converter can increase the Capture Width Ratio and can shift the performance towards higher frequency waves. The rigid motion of an offshore floating converter can have a negative effect on the performance of the device. A study in [25] performed three phases of experiments on fixed, free-floating and moored conditions with three mooring settings and the results concluded that body motions can decrease the capture width ratio and 45 degrees for moored conditions performed best among all conditions.

Despite the opportunities mentioned in this part, there are a couple of challenges with offshore energy

convertors which should be considered at the design and development stage. The first concern is long-term economic viability including the cost of installation, commissioning, operation and maintenance costs and it is concluded that it is necessary to include financial risk management in any type of analysis [26]. The second challenge in using an offshore energy converter is the cost of building the foundation which can be 20% higher than the same onshore windfarm and the total price for the tower and foundation can also be around three times more expensive than the same onshore model [27]. Another obstacle in using offshore wind farms is the operation and maintenance costs per unit of power including designing a control and monitoring system to ensure that the whole plan is profitable [28]. The constraint in choosing a generator is another factor to be considered and among all types of available generators, using the SCIG generator is the best option because of its robustness in harsh situations.

1-3- Scope and Significance

The focus of this thesis is the design of a hybrid wave-wind WEC that can be integrated into the windcatcher mechanism. A theoretical foundation is provided to assist in understanding why a hybrid energy system is more efficient.

In today's industry, there are offshore wind farms with a wide range of WEC systems. These technologies have a historical past, but even with the advances made recently, it is still not as cost-effective as expected. As a result, more work remains to enhance the design of these systems so that they can be used more effectively in the future. Over a thousand ideas have been patented since the commencement of the development stage, of which two hundred have progressed to the point of prototype experimentation and just a few have been built [29]. When compared to other resources, the progress of energy conversion from wave equipment has always lagged. The biggest stumbling block to its advancement is its economic outlook, which has yet to satisfy the requisite future expectations to make these systems a worthwhile investment. The significant requirements for investment spending for cost-effective commercialization are regarded as one of the main limitations of WECs. Integrating the primary design with other renewable energies, which is the goal of this study, is an appealing way to compensate for the high cost.

The research proposed in this thesis proposes an innovative way of increasing the airflow rate and, hence, the output produced energy by adding a mechanical construction called a windcatcher to the chamber of an oscillating water column (OWC). In addition, a new proposed turbine location is presented. This, in combination with the windcatcher, provides to produces unidirectional airflow through the turbine with a decreased oscillation portion, resulting in more uniform power output. Besides, the overall system performance is influenced by its geometrical factors. As a result, the geometry must be modified to produce an optimum turbine airflow rate. Therefore, the geometric enhancements and optimizations of the primary model of the hybrid wave-wind WEC are described in this work.

1-4- Contributions

Based on the previous studies [30-34], CFD simulations that handle the Navier–Stokes equations are the preferred technique for simulating the complexities associated with the evaluation of a WEC. Another motivation for using CFD simulation is the requirement to include two phases in detail to simulate the issue. The CFD models can provide a detailed examination of the behaviour of working fluids in the cylinder and its vicinity, as well as the complicated geometries. Therefore, this work evaluates a novel construction for OWCs that considers the interaction of wind with the OWC construction to enhance the airflow velocity through the turbine blades by using CFD simulations. This unique construction was established by adding a windcatcher to the conventional OWC version to augment power generation performance by integrating wind flow into the pressurized airflow generated by the motion of the water column within the device's primary cylinder. By mounting on the tops of buildings to catch the high-speed wind flow, windcatchers have been employed for natural ventilation for years. The presented novelty in this study is a two-sided design of windcatchers, although other varieties of windcatchers can also be employed with the proposed system in this study. Moreover, an innovative location for the turbine is developed to manipulate the airflow generated by pressurized air in the cylinder as well as the wind flow generated by the windcatcher's entrance. Besides, the influence of major geometrical factors such as turbine height, orifice width, and orifice output angle on the

suggested hybrid system's performance (i.e., orifice flow rate, chamber pressure, turbine flow rate, and power) is investigated and analyzed.

1-5- Publication

Sadegh Khaleghi, Tek Tjing Lie and Craig Baguley, “Design and Output Power Evaluation for A Novel Hybrid Wave-Wind Energy Converter,” *Journal of Ocean Engineering*, 2022. https://doi.org/10.1016/j.oceaneng.2022.111573.

Chapter: 2 Literature Review

This chapter will provide background knowledge and an overview of the recent developments in various types of OWCs. Following that, the recent theoretical and practical research to improve the mechanism and performance of the converter are captured and explained and the main challenges are addressed.

2-1- OWC technology

Yoshio Masuda, who developed a 120W OWC in Japan in 1965, was the first person to present using the OWC idea [35]. The OWC principle has also been employed in multiple varieties around the world, and it is preferred for its simplicity of operation with no immersed moving components, structural durability, convenience of maintenance, and adaptability to be employed in different situations.

Error! Reference source not found. depicts the fundamentals of the OWC energy conversion stages. As seen, two stages are essential for energy conversion. The first one is the conversion of hydrodynamic interaction into mechanical energy, in which the momentum of the waves pressurizes the air, which is used by the air turbine. The generator is then used in the second stage to convert mechanical power to electrical current [36].

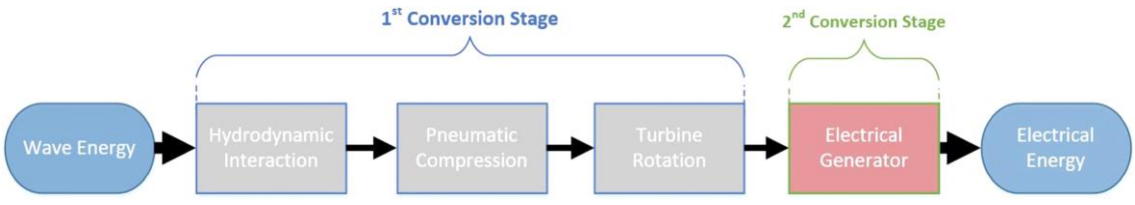

Figure 2-1: Processes for converting wave energy in an oscillating water column [36].

The OWC idea harvests energy by employing waves' surface motion to compress the air inside a column. As shown in **Error! Reference source not found.**, the surface raises as the peak of the wave crosses and falls with the tunnel of the wave, creating bidirectional airflow and pressure variations within the cylinder. A turbine capable of accomplishing rectification by itself is necessary for these bidirectional airflow devices to allow for continued spinning in one path while the flow constantly changes direction past the turbine. The Wells turbine, developed by Prof. Alan Arthur Wells of Queens University, is the most frequently deployed turbine in OWCs [37]. This turbine solves the obstacle of alternating airflow rate using symmetric airfoils, which allow the turbine to spin in one direction independent of the airflow path. Additional turbine choices, including the self-rectifying bidirectional impulse turbine [38] and Savonious turbine [39], have been proposed and future developments in this field are being investigated.

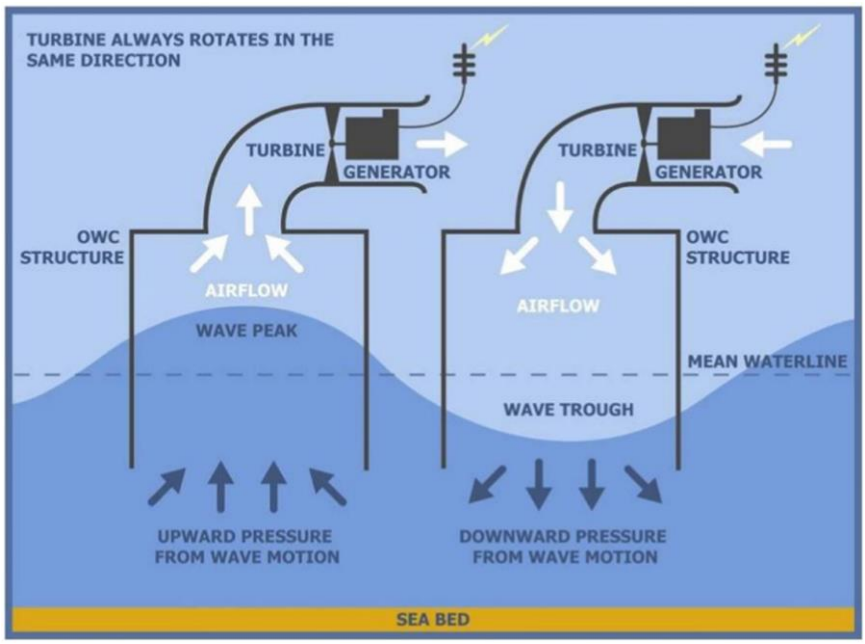

Figure 2-2 The main idea of OWC [37].

2-1-1- Multi-resonant OWCs

Most multi-resonant devices are self-tuning versions of the OWC concept meaning that they function effectively over a wider frequency band founded on the assumption that various lengths of the water column affect the resonant period of the OWC [40], with the moveable surface being

the primary wave radiator. The Ocean Energy (OE) Buoy, based on the backward bent bend duct buoy concept is one example of an OWC multi-resonant device [41], with an L-shaped cylinder exposing the intake to the travelling wave, as shown in **Error! Reference source not found.**.

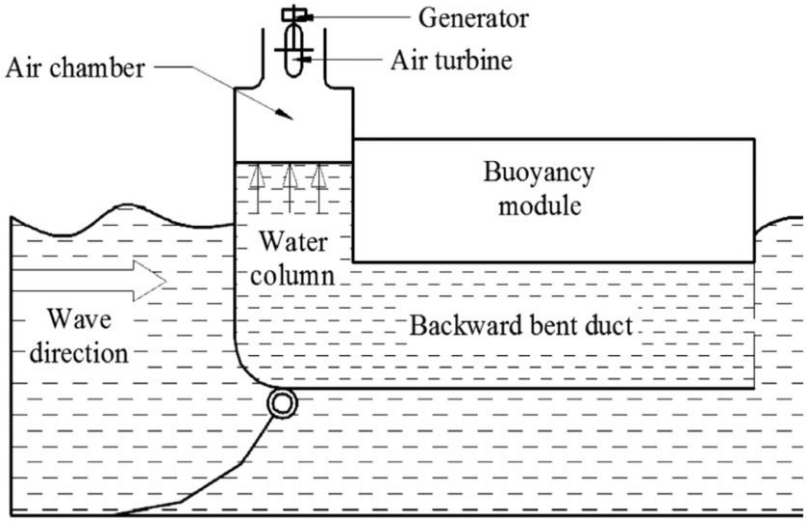

Figure 2-3 The schematic of a backward bent duct buoy [41].

2-1-2- Multi-oscillating water columns

The multi-oscillating water column (M-OWC) concept, also known as the multi-chamber oscillating water column [42], is a configuration of OWC installations that are connected in terms of construction, airflow, PTOs, or generators. However, one of the drawbacks of OWC functioning is the variable energy output caused by bidirectional airflow, which is the fundamental issue that more current M-OWC designs normally try to address. Although the self-rectifying turbine technique is well developed, it remains an ineffective phase in the energy conversion process, which gives the M-OWC a significant privilege.

It is critical to identify the three primary M-OWC sub-classes as reported by Delmonte et al. [36]. **Error! Reference source not found.**a shows an OWC array that comprises many unique OWCs that operate in solitary with separate turbines and generators but are placed in a shared framework to form one system. **Error! Reference source not found.**b depicts a segmented M-OWC for which the turbines of numerous OWCs stay separate but are structurally connected to run the

same generator. **Error! Reference source not found.**c shows a modular M-OWC, which utilizes a series of cylinders that provide airflow that is coupled or collected and adjusted upstream of the turbine. As a result, the merging of the different OWC units happens prior to the PTO phase to provide continuous unidirectional airflow. The M-OWC could be extensively classified further into sub-groups, particularly the segmented or modular M-OWCs. Modular M-OWCs, for instance, can be open or enclosed devices. Closed devices generate large and small pressure channels downstream and upstream of the PTO, resulting in a significant pressure difference. As a result, a controlled volume of working fluid is in rotation. Open devices use large pressure upstream and ambient pressure downstream of the PTO.

When a device runs exclusively on unidirectional airflow, the process of inhaling and exhaling does not proceed throughout the whole system, as it does with a standard OWC. As a result, the phrases upstream and downstream relate to the distinct functioning situations, which is the constant directional variation of airflow [29].

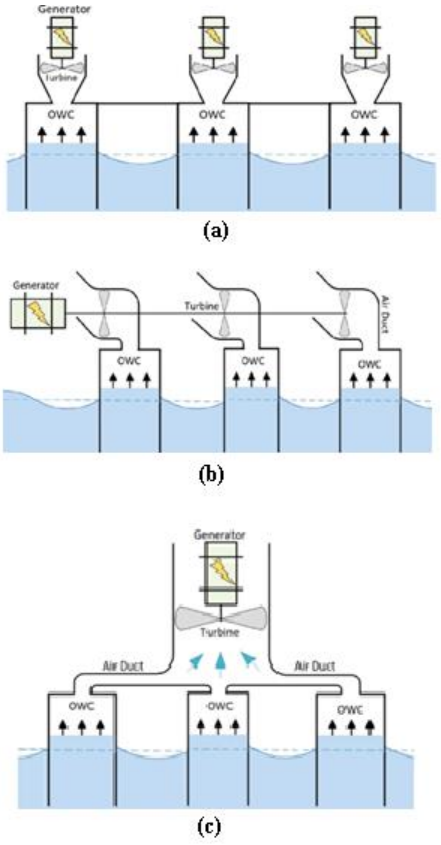

Figure 2-4: Multi-oscillating water columns: (a) OWC Array design; (b) segmented M-OWC design; (c) Modular M-OWC design [36].

2-1-3- Floating OWCs

A two-cylinder system called MORE was originally examined in a MARINET project [43]. It was based on the M-OWC Sea breath idea, which is shown in **Error! Reference source not found.**. Such a floating system is made up of numerous OWC cylinders aligned with wave propagation. As the wave tops and bottoms pass, each OWC generates large and small pressures. Unidirectional valves enable pressurized air from each cylinder to collect in a central high channel during the compression phase. Furthermore, unidirectional valves permit flow from the low-pressure channel to occupy the cylinder when the water content drops, resulting in negative pressure. The high and low-pressure channels, as shown in **Error! Reference source not found.**, form a closed device with a theoretically more consistent high-pressure flow difference throughout the turbine. The benefit of these devices is that there will continuously be a consistent intake of air, even in less-than-ideal situations.

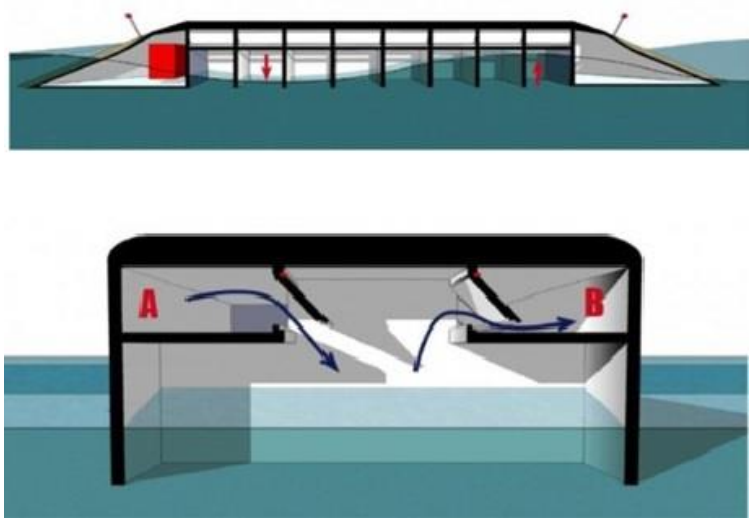

Figure 2-5: Sea breath device as the floating concept [43].

The LEANCON device [29] is a hovering V-shaped M-OWC that generates large and small pressure air channels using an array of various small OWC cylinders, as shown in **Error! Reference source not found.**. The ‘V' shape, enables the WEC to collect a wider breadth of the

wave. The huge quantity of cylinders, in theory, create an equilibrium of forces as localized peak and weak pressures act within the cylinders. The structure is small, with air channels incorporated into the structural construction and a PTO system consisting of turbines placed between peak and weak pressure channels according to unidirectional flow. The device's shape, as well as the collection of cylinders angled with their entrances facing the incident wave peak, are designed to reduce the wave force of impact. Additionally, the anchorage location, which is optimal when on the bow, aids the WEC in aligning with the wave axis, because the two arms create a stabilizing function [29]. The majority of OWCs are onshore or semi-immersed floating constructions, except for a fully submerged shallow sea, V-shaped breakwater incorporated converter [44]. This M-OWC type, which is installed on the seafloor, employs a closed cycle unidirectional airflow device comprising unidirectional valves and strong and small pressure connectors, as shown in **Error! Reference source not found.** (Stellenbosch equipment). When immersed, the chances of component failure reduce, but components are subjected to accelerated overall corrosion rates [44].

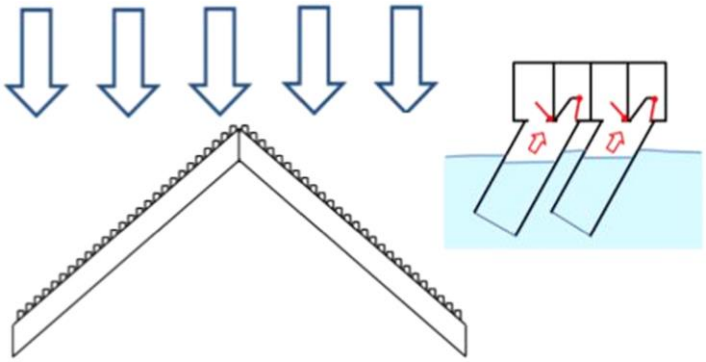

Figure 2-6: The orientation and working premise of LEANCON [45].

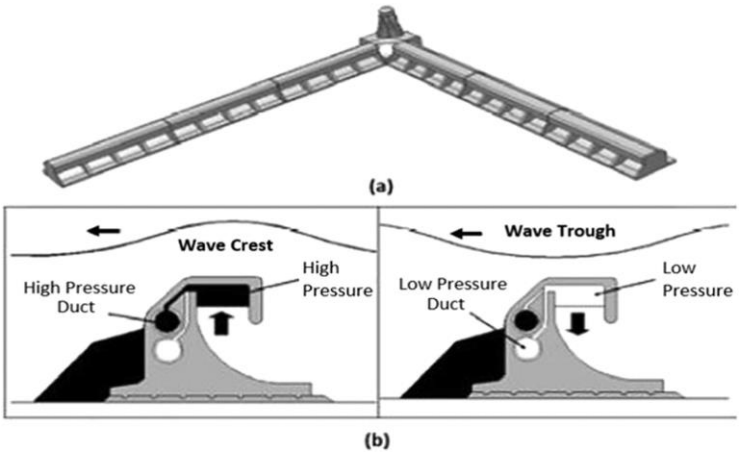

Figure 2-7: Stellenbosch equipment configuration and operation concept [44].

Recently, experimental works with a 1:25 magnitude immersed single cylinder prototype of the concept have shown a total conversion rate of 22%. The design is already being investigated for certain purposes and further improvement [46]. Despite this fact, the practical optimization of the SWEC is still under development [47].

2-1-4- Multi-resonant M-OWCs

Resonance and the ability to tune to resonance are appealing qualities in singular OWCs. While different M-OWC concepts can solve the airflow problem, if a larger bandwidth or the potential for more resonant peaks can be developed, the M-OWC concept will undoubtedly stand out [29].

2-1-5- Performance comparison

According to the equipment performance comparison compiled by Babarit [48], the M-OWCs' effectiveness (i.e., the efficiency of power extraction) ratings do not demonstrate considerable increases over the singular OWCs such as the (OE) Buoy. OWCs are particularly economical with fixed oscillating wave surge converters (OWSCs) especially compared to different forms of WECs, as shown in **Error! Reference source not found.**. With only a few highly inconsistent performances of small-scale M-OWCs, it is difficult to say if they will be economical at this level. The modular type M-OWC capabilities and estimations have been insufficient to remain competitive with various singular OWCs. The CWR data summarized by Babarit [48] and shown

in **Error! Reference source not found.** effectively provides the evaluations and demonstrates that for OWCs, like with other WEC categories, no equipment functionality considerably surpasses the others.

Table 2-1: Mean and standard deviation of capture width ratio (CWR) for different WEC categories [48].

Property	**Approach**	**OWCs**	**Overtopping devices**	**Heaving devices**	**Fixed OWSCs**	**Floating OWSCs**
Capture width ratio (%)	Mean	29	17	16	37	12
	STD	13	8	10	20	5
Characteristic dimension(m)	Mean	20	124	12	18	33
	STD	10	107	7	14	24

In this chapter, the various categories of the WECs have been described. Besides, among the presented WEC systems, the OWC system has been illustrated in more depth since it will be the focus of the study. Moreover, the reasons for choosing OWC among different types of WECs to study in this thesis have been discussed. In the next chapter, the in-depth literature review in the OWC-related field will be presented. Then, research gaps analysis and the novelty of this study will be highlighted.

2-2- Integrated OWC and Breakwater Studies

Practically, there are two methods to reduce the cost of the OWC device's wave power. One is to increase the effectiveness of the wave power harvesting system directly using a sequence of optimization procedures, while the other one is to incorporate the OWC system into a novel marine construction. Many scholars have conducted analytical studies on the incorporation of an OWC into a breakwater. The hydrodynamic properties of a two-dimensional OWC, consisting of a narrow vertical surface-piercing obstacle beside a perpendicular wall were investigated by Evans et al. [49]. The theoretical results that were presented showed that an OWC could recover all the input wave power due to wave reflection from the wall. Rezanejad et al. [50] analyzed the

effectiveness of a 2D dual-chamber nearshore OWC. The intake of the outer chamber had been discovered to be vital in setting the main resonance frequency, which considerably benefited overall electricity production. Ref. [51] investigated the influence of stepped lower part topography on the effectiveness of a 2D nearshore narrow-wall OWC and concluded that the introduction of an artificial step at the seabed, together with some adjustment, results in a greatly improved capacity of energy extraction for electricity generation.

Martins-Rivas and Mei [52, 53] studied the behavior of a narrow-wall OWC placed at the point of a thin static breakwater or alongside a straight coastline, developing theoretical methods based on the linear potential flow concept to handle three-dimensional wave radiation challenges. An integral equation for the horizontal velocity under the wall was used in their simulations to account for the singular behaviours in the velocity field along with the void under the thin wall of the OWC cylinder. The retrieved energy of the OWC erected at the point of a narrow breakwater had been proven to be rather unresponsive to incident wave path, while the response of an OWC located on a straight coast was shown to be completely reliant on wave path for a range of frequencies, the greatest result obtained when the incidence was normal. The energy absorbed by the OWC can be doubled due to wave reflection at the coastline.

Zheng et al. [54] established a theoretical framework of a coast-breakwater integrated OWC that took into account the impact of the thickness of the OWC cylinder wall. **Error! Reference source not found.** shows their investigated system. Their result proved that the thinner the cylinder wall, when applied to a constant outer radius, the greater and wider the prominent peaks of the frequency response of wave energy catch width.

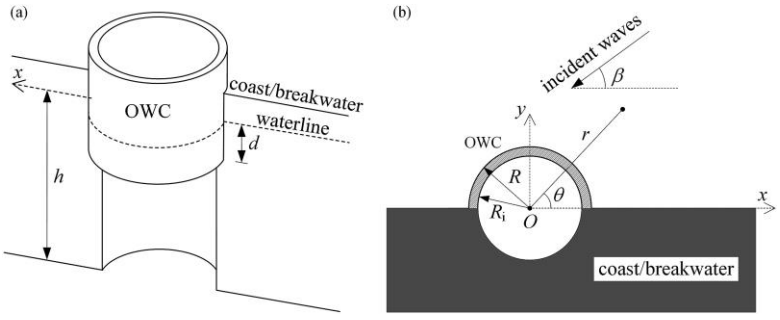

Figure 2-8: OWC incorporated into a coast/breakwater: (a) bird view; (b) top view [54].

2-3- Arrays of OWCs Studies

The ultimate objective of studying OWC systems is to provide power on a large scale. Therefore, it's important to analyze the performance of the arrays of OWC systems, which is investigated by several scholars. Wave farms comprising arrays of OWCs are anticipated to be developed to completely capture the potential wave energy in a location and produce substantial amounts of electricity for power grids. Cost-sharing advantages of deployment and electricity supply transmission can also be achieved for those OWCs deployed close to each other. Nihous [55] provided a methodology to forecast wave energy absorption from an array of OWCs based on analytical analysis of hydrodynamic concerns from an oscillating circular patch on the ocean surface. Further, diffraction effects were ignored in the analysis. Nader et al. [56] used a 3-D finite element (FE) technique modelling to analyze a limited array of stationary OWCs without the limitation of shallow draught. The array's complicated hydrodynamic relationships with the OWCs were emphasized. Moreover, **Error! Reference source not found.** shows the overall wave magnitude surrounding and within the four OWC equipment arrays for different values of spacing.

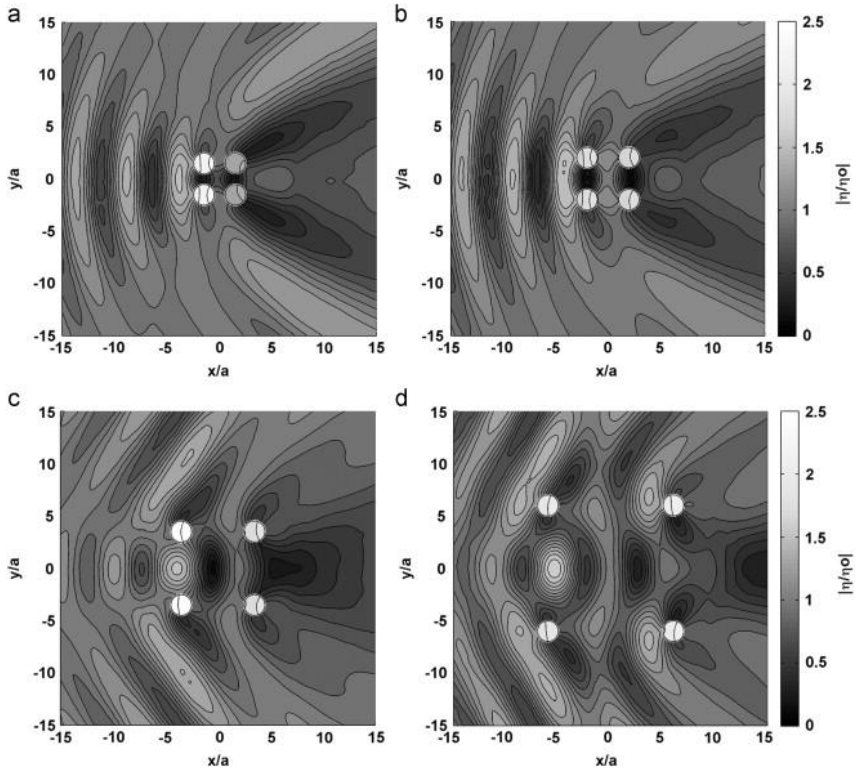

Figure 2-9: Overall wave magnitude surrounding and within the four OWC equipment arrays for different values of spacing (a) L/a=1, (b) L/a=2, (c) L/a=5, and (d) L/a=10 [56].

Subsequently, a more comprehensive simulation that took into consideration the air compressibility within the OWC cylinder was presented [57-59]. The results demonstrated that for specific wave frequencies, the array of stationary OWCs can capture more energy than the same number of OWCs working standalone. Konispoliatis and Mavrakos [60] designed an optimal analytical method to evaluate the behaviour of an array of floating OWCs. Significant enhancements in retrieved electricity were observed for arrays with specific distances between OWCs. An offshore dual-chamber OWC system subjected to frequent waves has been investigated by Ning et al. [61], experimentally as shown in **Error! Reference source not found.**. For the dual-chamber OWC mechanism, two distinct resonance frequencies were discovered.

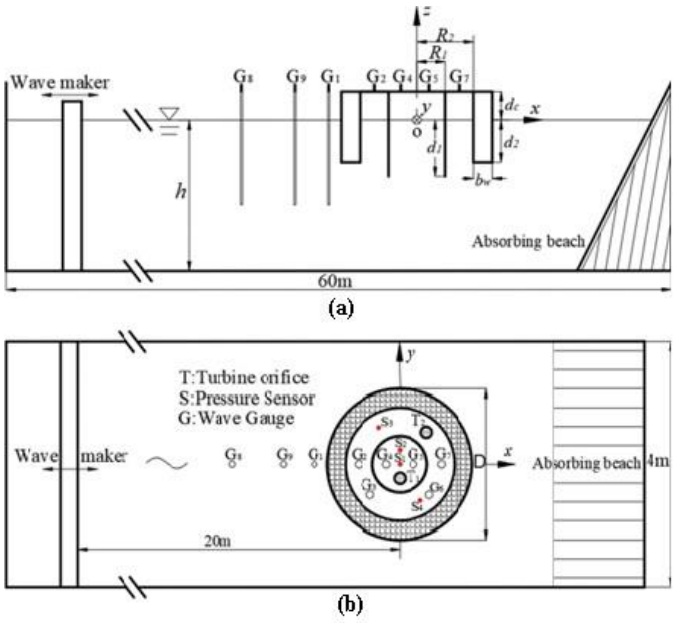

Figure 2-10: Experiment arrangements. (a) A side view of the OWC device and wave gauges; (b) a plan view of the orifices and pressure sensors [61].

2-4- Computational Fluid Dynamic (CFD) Studies

WECs account for a relatively small but theoretically important portion of the world's renewable energy sources. Nevertheless, to compete with offshore wind or solar energy, the WEC sector will need to develop successful prototypes that can be scaled up for commercialization purposes. To reliably evaluate performance indicators during the primary design phases, this approach necessitates the implementation of effective and trustworthy numerical modelling methods. The computational fluid dynamic (CFD) algorithms that solve the Navier-Stokes equations or the Reynolds averaged Navier-Stokes (RANS) problems provide the treatment of complicated nonlinearities that other approaches cannot manage. The linear and nonlinear potential flow approach, fully nonlinear potential flow approach, and CFD method, which solves the Navier–Stokes equations for single-phase or two-phase fluids, are the three most used procedures for numerical modelling of WECs. The most challenging problem with the CFD approach is accurately resolving the two-phase fluid interface within the chamber between the water and air. Horko [30] used an experimentally verified two-dimensional CFD simulation using the Fluent software to evaluate the impact of the OWC chamber's frontal lip on the device's hydrodynamic

behaviour. Ref. [30] discovered that modest adjustments to the chamber's frontal wall, such as increasing its thickness or giving curving, can result in significant gains in OWC effectiveness. Using Navier-Stokes equations, Xu et al. [31] developed a three-dimensional CFD model to study the hydrodynamics of a circular bottom-sitting OWC mechanism demonstrating that vortex shedding significantly increases spatial distinctness within the OWC cylinder. **Error! Reference source not found.** shows a three-dimensional representation of the OWC simulation and wave height patterns within the OWC cylinder presented by Xu et al. [31].

Ref. [32] introduced an incompressible three-dimensional CFD method to evaluate the stationary multi-chamber OWC equipment. The CFD findings are proven to be consistent with the experimental results.

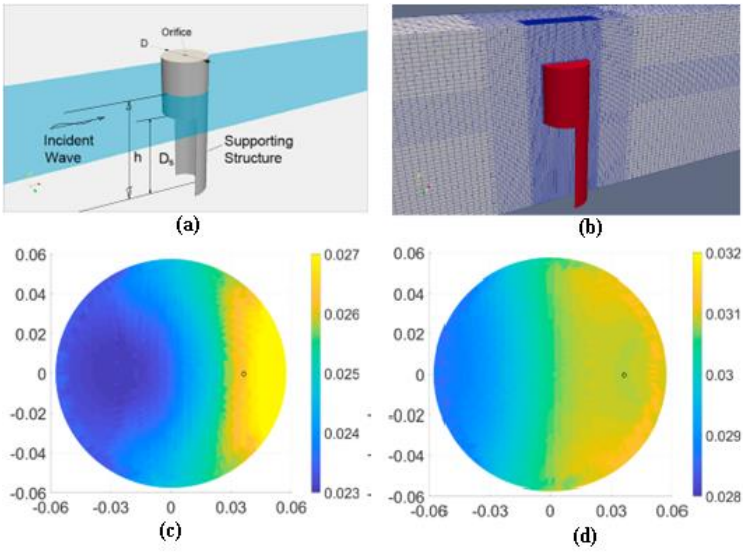

Figure 2-11: (a) a three-dimensional representation of the OWC simulation, (b) a perspective of the mesh setup around the OWC model (c) wave height patterns within the OWC cylinder for 0.7s time passed (d) wave height patterns within the OWC cylinder for 0.8s time passed [31].

Goeijenbier et al. [62] study the opportunities for structural optimization to further reduce the costs of OWCs. In a one-way linked hydraulic-structural numerical simulation, an OWC with an extra vertical channel is studied in a three-dimensional domain. The model included a fluid domain, which was the wave tank, as well as a solid domain, which was the OWC structure. It was discovered that by removing the structural domain and utilizing the discovered property that

water pressures are uniform across the crosswise width, a 2D model would be acceptable for feasibility study applications, which significantly reduces simulation complexity. **Error! Reference source not found.** depicts their results with the top row at the maximum inflow and the bottom row at the maximum outflow.

Wang and Zhang [63] carried out the numerical investigation of the hydrodynamic properties of an OWC mechanism linked with a submerged horizontal sheet using the CFD toolbox OpenFOAM. For an ideal structural design, the effects of changing the submerged depth and sheet length on relevant factors of a sheet-integrated device, such as energy absorption efficiency, reflection and transmission coefficient, and energy dissipation coefficient, were investigated. Furthermore, in terms of hydrodynamic characteristics and vorticity field, the unique WEC-sheet integrated system was compared to an OWC device positioned over an immersed breakwater at the same submerged level. The findings reveal that integrating a submerged horizontal sheet can significantly enhance the functionality of an OWC system and that a lesser submerged depth is far more able to achieve a fair transmission coefficient and be more advantageous for power production.

Elhanafi et al. [64] employed a nonlinear two-dimensional RANS-based CFD simulation to analyze the power equilibrium of an onshore OWC. The CFD simulation was validated using available physical data of cylinder differential air pressure and free surface level. It was discovered that the dampening used has a significant influence on the energy conversion operation. Additionally, during the inflow and outflow stages, both power take-off (PTO) damping, and wave height have an essential impact on vortex generation near the top and bottom cylinder mouths.

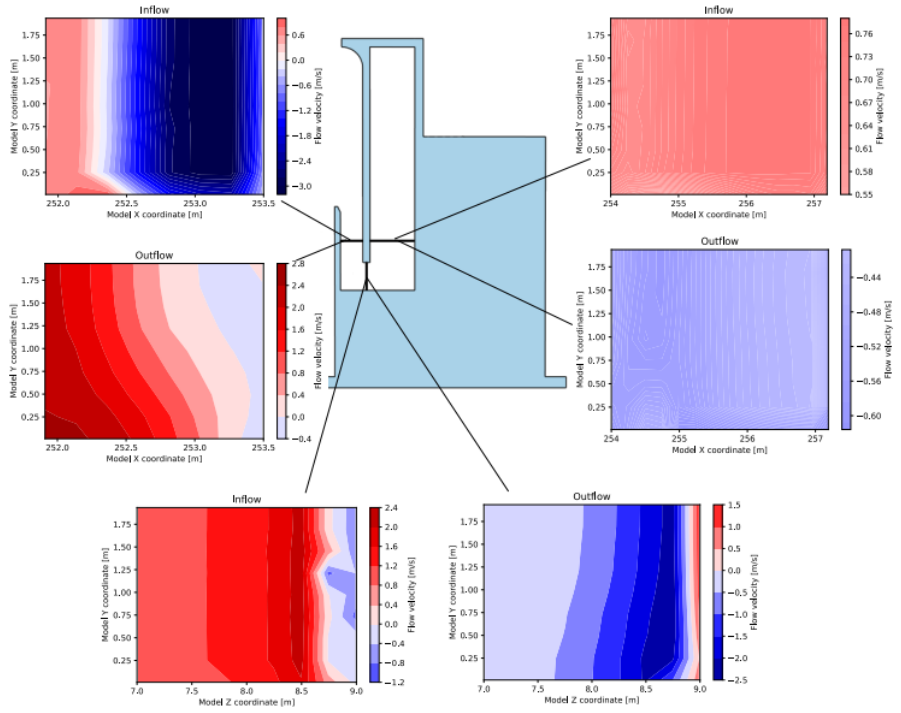

Figure 2-12: Flow velocity pattern in the channel at maximum outflow and inflow, beneath the front wall, and within the cylinder [62].

Lopez et al. [65] propose an extensive simulation of the impact of seabed morphology on the efficiency of OWCs. Different wave parameters, notably storm and post-storm situations, are studied. The simulation model was defined in ANSYS Fluent, and the variations in the seafloor for various wave situations were simulated. Their results reveal that the performance of energy extraction in the OWC is strongly controlled by the seabed equilibrium states associated with storm development. **Error! Reference source not found.** depicts their results for the mass transport for the different scenarios. As observed, **Error! Reference source not found.** illustrates the normal development of a storm: strong waves (H=4m) with flat seabed (case γ shown in **Error! Reference source not found.**), proceeded by seabed development (case P8B shown in **Error! Reference source not found.**) with the same wave situations. Following that, with that developed seabed (case β shown in **Error! Reference source not found.**), a decrease in wave energy (H=2m), followed by a depletion in the dimension of the seabed morphology under the same moderate wave situations (case P4B shown in **Error! Reference source not found.**).

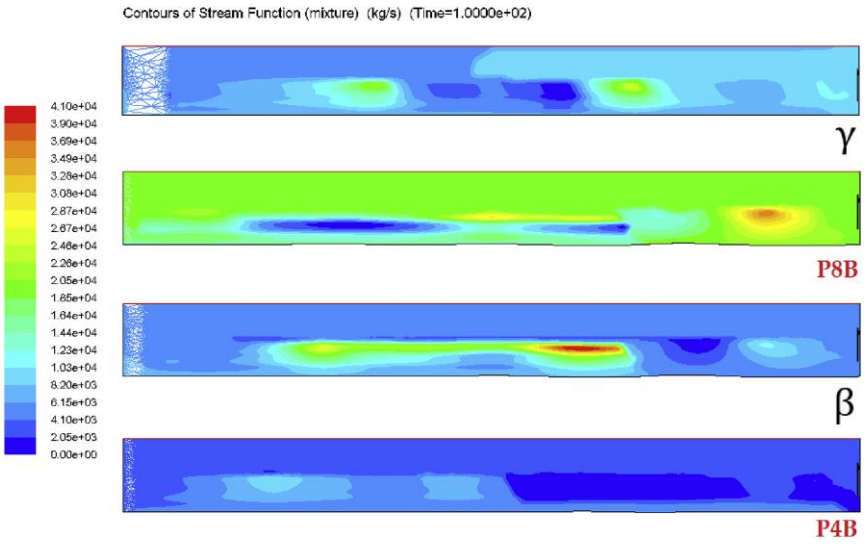

Figure 2-13: Stream contours of velocity (kg/s) for different scenarios [65].

Cabral et al. [66] investigate the efficiency of a novel hybrid WEC module integrating an OWC and a piece of overtopping equipment incorporated into a rubble mound breakwater, based on outcomes of a physical model study carried out at a geometrical ratio of 1:50, as shown in **Error! Reference source not found.**. Before the experimental measurements, the device's effectiveness was numerically refined using ANSYS Fluent. The hybrid WEC's wave power capture was computed, and the efficiency of the two capturing approaches was examined. It was proved that hybridization could result in technologies that are more efficient than their single components for a wider variety of wave circumstances.

For three-dimensional modelling of an OWC, a novel solution for wave and structure interaction is employed by Iturrioz et al. [33]. The RANS equations for two incompressible phases are solved using the CFD simulation, which was water and air. To verify the numerical findings, laboratory tests are carried out on a modest scale. The method is also used to better awareness of important mechanisms and demonstrates the possibilities for extensive investigation. Even though the experimental situation was two-dimensional, the three-dimensional field of the wave flume was numerically modelled to demonstrate OpenFOAM's potential. **Error! Reference source not found.** depicts CFD results achieved by Iturrioz et al. [33] for airflow velocity as time passes.

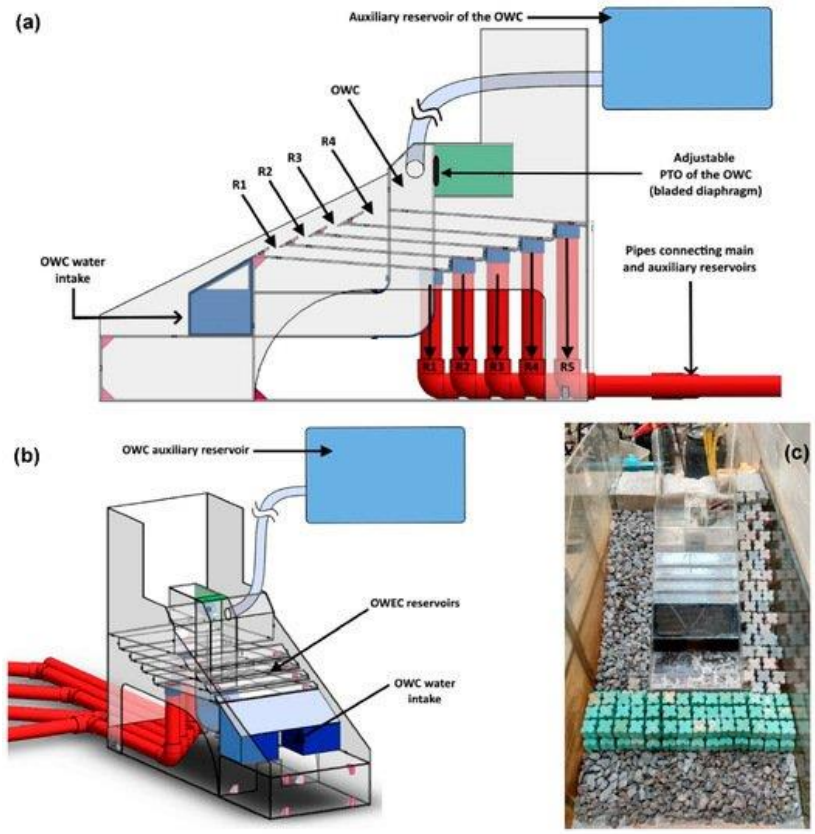

Figure 2-14: (a) Cross-section picture;(b) three-dimensional image of (c) the planned physical design with HWEC positioned in the centre of the breakwater during the Antifer blocks armour surface installation [66].

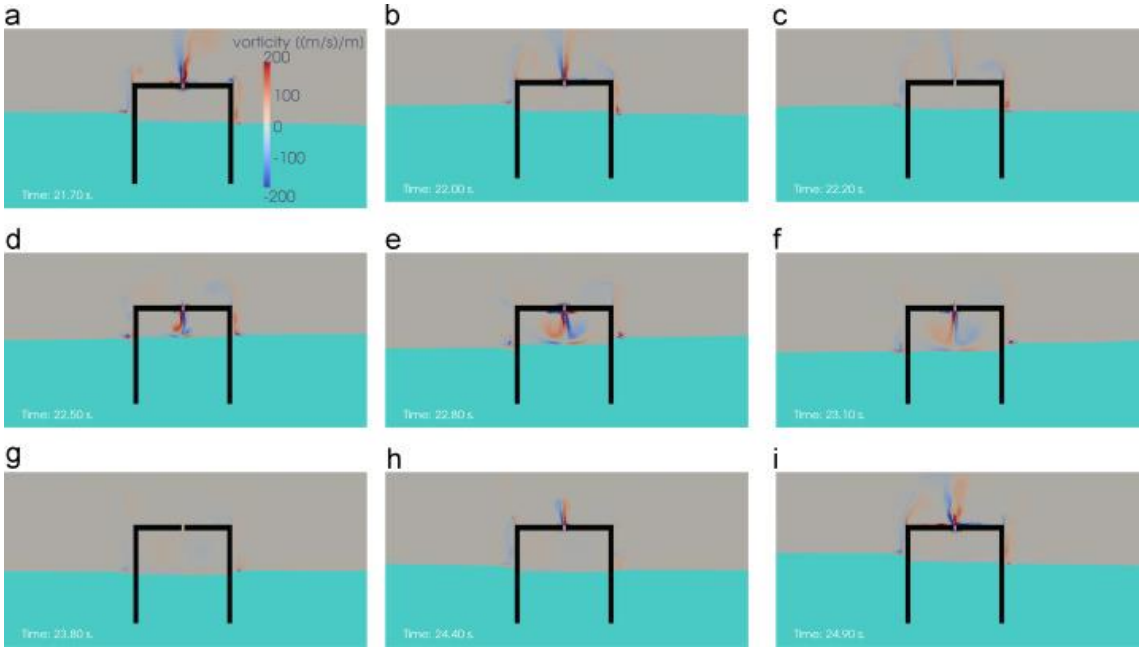

Figure 2-15: Airflow vorticity during a chamber pressurization-depressurization loop as time passes: (a) t=21.70 s; (b) t=22.00 s; (c) t=22.20 s; (d) t=22.50 s; (e) t=22.80 s; (f) t=23.10 s; (g) t=23.80 s; and (h) t=24.40 s; and (i) t=24.90 s [33].

2-5- Hybrid Wave-Wind Studies

Wind and wave behaviour are inextricably related. As a result, the design of hybrid technologies should be the next stage in the growth of the ocean renewable industry [37]. Hybrid developments integrate floating wind turbines with WECs to harvest energy from the offshore region while reducing initial costs. In this classification, current or existing harbour equipment could create hybrid technologies that combine electricity generation and harbour safety.

Cong et al. A novel integrated approach for the multi-application usage of offshore renewable energy resources that consists of an OWC device and an offshore wind turbine is developed in [67]. A monopile structure supports the wind turbine, and the associated OWC is concentric with the structure. The external shell of the OWC and the monopile structure are joined within the cylinder by four vertical reinforcing sheets. The outcomes show that by selecting an ideal turbine setting, wave power generated by the OWC can be a valuable complement to the integrated system. Furthermore, in certain wave situations, the wave forces on the OWC and the monopile can neutralize each other, resulting in an almost zero net wave force on the entire structure.

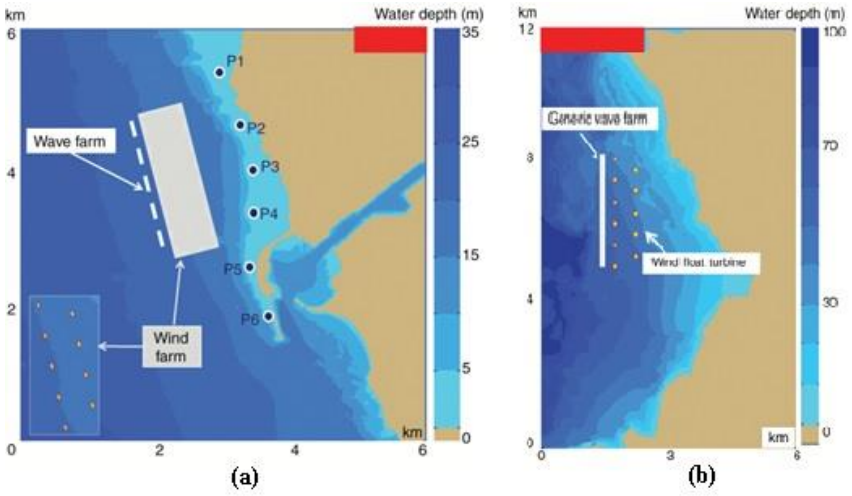

Figure 2-16: Integrated wind and wave system scenarios have been described for a variety of coastal ecosystems, including (a) Leixoes (Portugal) [68] and (b) Porto Ferro (Sardinia) [69].

Error! Reference source not found. [68, 69] depicts two case studies in which the influence of various wind-wave developments on the regional wave system was assessed. The research revealed that the shadow impact might be influenced by parameters such as wave path, the spatial alignment of the marine field, coastline, wave strength, and the farm's absorption capacity. To

protect a specific beach area, it is necessary to initially evaluate the regional wave behaviour and then determine an appropriate WEC layout, considering the chain consequences that may arise in nearby coastline regions.

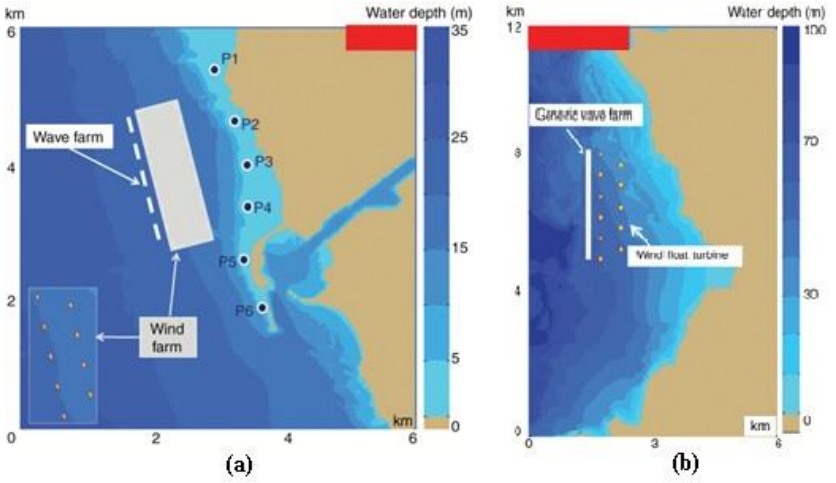

Figure 2-17: Integrated wind and wave system scenarios have been described for a variety of coastal ecosystems, including (a) Leixoes (Portugal) [68] and (b) Porto Ferro (Sardinia) [69].

2-6- Research gap and methodology

The research model introduced by [64] the hydrodynamic performance of an OWC device and performed energy balance analysis to explain the energy conversion chain for an OWC using a CFD model and results validated against a practical model designed by [70]. Fig 2-18 shows the detail of the numerical model used in [64] including the dimension of the numerical model and the position and structural details of the designed fixed OWC.

As mentioned before, chamber differential air pressure and airflow rate inside the orifice are the two most factors that can simulate the achievable output power from an OWCs. The main factor which has a direct effect on the air pressure inside the chamber of an OWC is the free surface movement inside the chamber which compresses and decompresses air inside the chamber. A 2D CFD model was designed to validate the airflow, air pressure and output power with the practical experiment in [70] with an error of less than 0.5% which shows the high capability of the CFD model in modelling practical experiments.

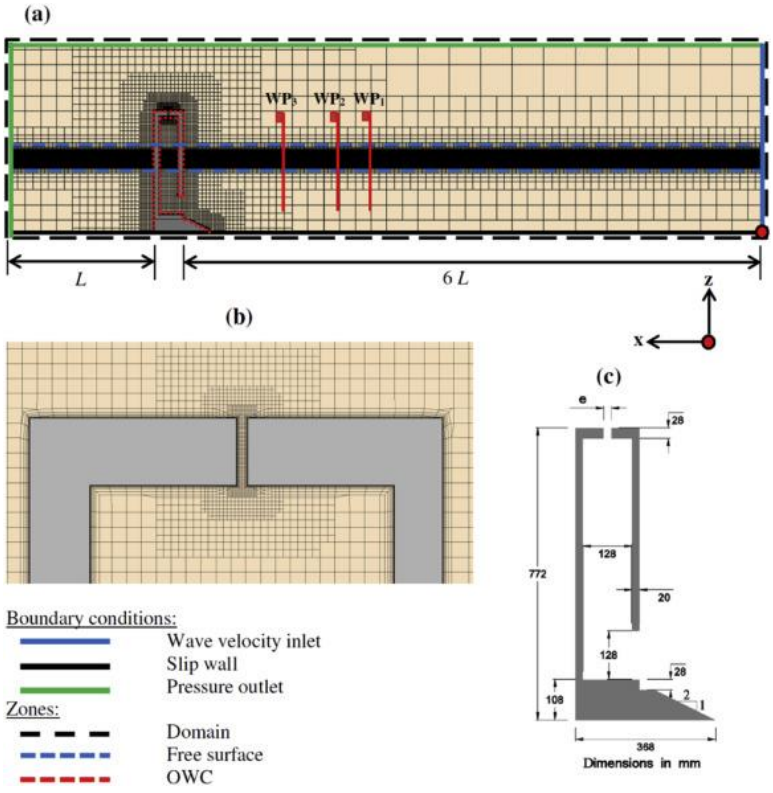

Figure 2-18: Concept design parameters and mesh details with the dimension details for the fixed OWC in [64].

The objective of the practical experiment in [70] was to perform an analysis of the influence of the main environmental parameters like wave conditions on OWC hydrodynamic performance. The authors performed 387 tests under different wave conditions and tidal waves, and they found that turbine damping has the most effect on the hydrodynamic performance of an OWC, so, selecting the right turbine is necessary to have the OWC in optimal working condition. This practical model is set up in a flume tank at the University of Santiago de Compostela which was 20 m long, 0.65 wide and 0.95 high.

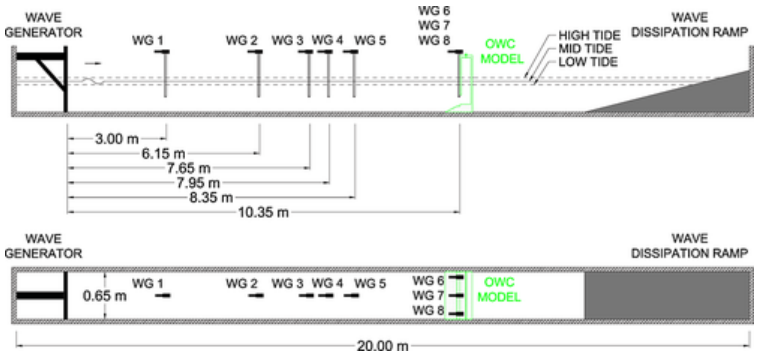

Figure 2-19: Detail of the experimental design including the placement of the sensor positioned along the tank in [70].

Waves are generated using a piston-type paddle which shows as the Wave Generator in Fig. 2-19 Eight gauges are positioned along the tank and OWC to measure the wave height along the tank and inside the chamber of the OWC. Table 2-2 explains the details of the practical design of the experiment in [70] including the detail of the converter and flume tank. Pressure and ultra-sonic sensor are used to measure the differential air pressure between the chamber and outside. The same model for flume tank and measurement elements are designed both in [64] and the current study in this thesis.

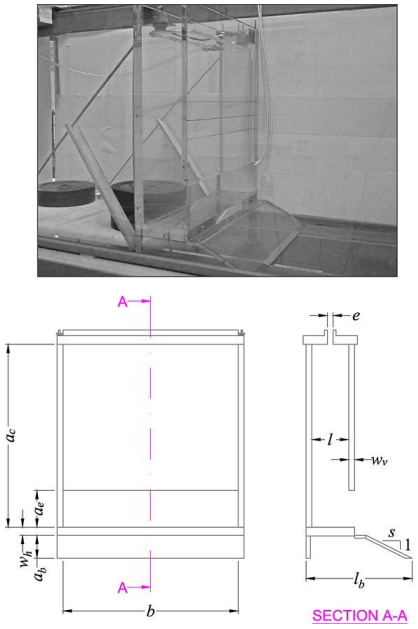

Figure 2-20: Fixed OWC employed in [70] with dimension details for orifice and chamber.

Table 2-2: Dimension details of the practical model used in [70]

Geometrical details	parameter	Dimension (m)
Chamber height	a_c	63.6×10^{-2}
Chamber width	b	60.8×10^{-2}
Chamber length	l	12.8×10^{-2}
Entrance height	a_e	12.8×10^{-2}
Horizontal wall thickness	W_n	02.8×10^{-2}
Vertical wall thickness	W_v	02.0×10^{-2}
Bedding height	a_b	08.0×10^{-2}
Bedding length	l_b	36.8×10^{-2}
Bedding slope	s	2

The hybrid model introduced in this research is a bottom-fixed converter and the initial research conducted in this thesis used the CFD model and design in [64] and validated the results with the practical experiment in [70] and then a new hybrid wave-wind model was proposed and compared with the validated results to show the improvements.

2-7- Research Gaps Analysis

A detailed research gap analysis of the literature was conducted, and the most recent studies on OWC systems are described in **Error! Reference source not found.**. As proven, despite prior studies' accomplishments, considerable research gaps remain undiscovered as in the followings:

- A substantial majority of studies have not considered a progressive evaluation of the two-phase interaction of air and water throughout the simulation procedure.
- A large number of studies have ignored a comprehensive analysis to account for the effect of incorporating wind energy into the OWC construction in terms of increasing airflow velocity through the turbine blades.
- Although the use of windcatchers for increasing thermal comfort was recently studied by a few researchers, none of them investigated the effect of employing the windcatchers arrangement on the OWC system performance. Besides, the advantage of using a two-

sided design of windcatchers is ignored in these systems.

- To achieve the best system performance, the proposed system should be evaluated in terms of airflow control. Previous research, on the other hand, did not suggest a novel turbine placement to manage both the airflow produced by compressed air in the cylinder and the wind flow provided by the windcatcher's entry.

Referring to **Error! Reference source not found.** and the discussed research gaps, the main objectives of the investigation presented in this thesis are discussed in the following section.

2-7-1- Research objectives

Based on the previous studies [30-34], CFD simulations that handle the Navier–Stokes equations are the preferred technique for simulating the complexities associated with the evaluation of a WEC. Another motivation for using CFD simulation is the requirement to include two phases in detail to simulate the system. The CFD models can provide a detailed examination of the behaviour of working fluids in the cylinder and its vicinity, as well as the complicated geometries. Therefore, this study evaluates a novel construction for OWCs that takes into account the interaction of wind with the OWC construction to enhance the airflow velocity through the turbine blades by using CFD simulations. The unique OWC construction is established by adding a windcatcher to a conventional OWC to evaluate the effect of integrating wind flow into the pressurized airflow generated by the motion of the water column within the device's primary cylinder. The windcatcher type employed for the novel OWC is two-sided. Moreover, an innovative location for the turbine is designed to manipulate the airflow generated by pressurized air in the cylinder as well as the wind flow generated by the windcatcher's entrance.

Table 2-3: List of recent studies on the OWC systems to find the research gaps

Study	Year	Brief description	Was the two-phase interaction of air and water are taken into account throughout the simulation procedure?	Was the effect of incorporating wind energy into the OWC construction examined in terms of increasing airflow velocity through the turbine blades?	Was the effect of using the windcatcher on the system performance investigated?	If so, was a two-sided design of windcatchers presented?	Was a novel turbine placement designed to control the airflow produced by pressured air in the cylinder as well as the wind flow provided by the windcatcher's entrance?
Horko [30]	2007	An experimentally validated two-dimensional CFD simulation using the Fluent program to assess the effect of the OWC chamber's frontal lip on the device's hydrodynamic performance.	No	No	No	No	No
Martins-Rivas and Mei [52]	2009	They investigated the behaviour of a narrow-walled OWC positioned at the tip of a thin static breakwater or alongside a straight shoreline, developing theoretical approaches based on the linear potential flow idea to deal with three-dimensional wave radiation difficulties.	No	No	No	No	No
Nader et al. [56]	2012	A three-dimensional finite element (FE) technique to examine a small array of stationary OWCs without the constraint of shallow draught.	No	No	No	No	No
Rezanejad et al. [51]	2013	They investigated the efficiency of a 2D dual-chamber nearshore OWC.	No	No	No	No	No
Iturrioz et al. [33]	2015	The CFD simulation was used to solve the RANS equations for two incompressible phases, which were water and air.	Yes	No	No	No	No
Elhanafi et al. [64]	2016	A nonlinear two-dimensional RANS-based CFD modelling to examine the power equilibrium of an onshore OWC.	Yes	No	No	No	No
Xu et al. [31]	2019	A three-dimensional CFD analysis was used to investigate the hydrodynamics of a circular bottom-sitting OWC system.	No	No	No	No	No

Study	Year	Brief description	Was the two-phase interaction of air and water are taken into account throughout the simulation procedure?	Was the effect of incorporating wind energy into the OWC construction examined in terms of increasing airflow velocity through the turbine blades?	Was the effect of using the windcatcher on the system performance investigated?	If so, was a two-sided design of windcatchers presented?	Was a novel turbine placement designed to control the airflow produced by pressured air in the cylinder as well as the wind flow provided by the windcatcher's entrance?
Shalby et al. [32]	2019	A three-dimensional incompressible CFD approach for evaluating stationary multi-chamber OWC technology	No	No	No	No	No
Lopez et al. [65]	2019	A thorough simulation of the effect of bottom morphology on OWC efficiency.	Yes	No	No	No	No
Cabral et al. [66]	2020	Investigation of the effectiveness of a specific hybrid WEC module that incorporates an OWC and a piece of overtopping equipment into a rubble mound breakwater	No	No	No	No	No
Goeijenbier et al. [62]	2021	In a three-dimensional domain, an OWC with an extra vertical channel is explored using a one-way connected hydraulic-structural numerical modelling.	Yes	No	No	No	No
Wang and Zhang [63]	2021	A numerical analysis of the hydrodynamic parameters of an OWC mechanism coupled with a submerged horizontal sheet employing the CFD toolbox OpenFOAM.	Yes	No	No	No	No
Present study	**2021**	**A novel hybrid wave-wind wave energy converter's design and output power evaluation**	**Yes**	**Yes**	**Yes**	**Yes**	**Yes**

2-7-2- Proposed methodology

To reliably measure the performance metrics of the novel WEC type investigated in this thesis during the primary design phases, fast and accurate numerical modelling techniques are needed. The methodology used in this thesis is based on such a modelling technique, as shown in the flowchart in **Error! Reference source not found.** and explored in depth in subsequent chapters.

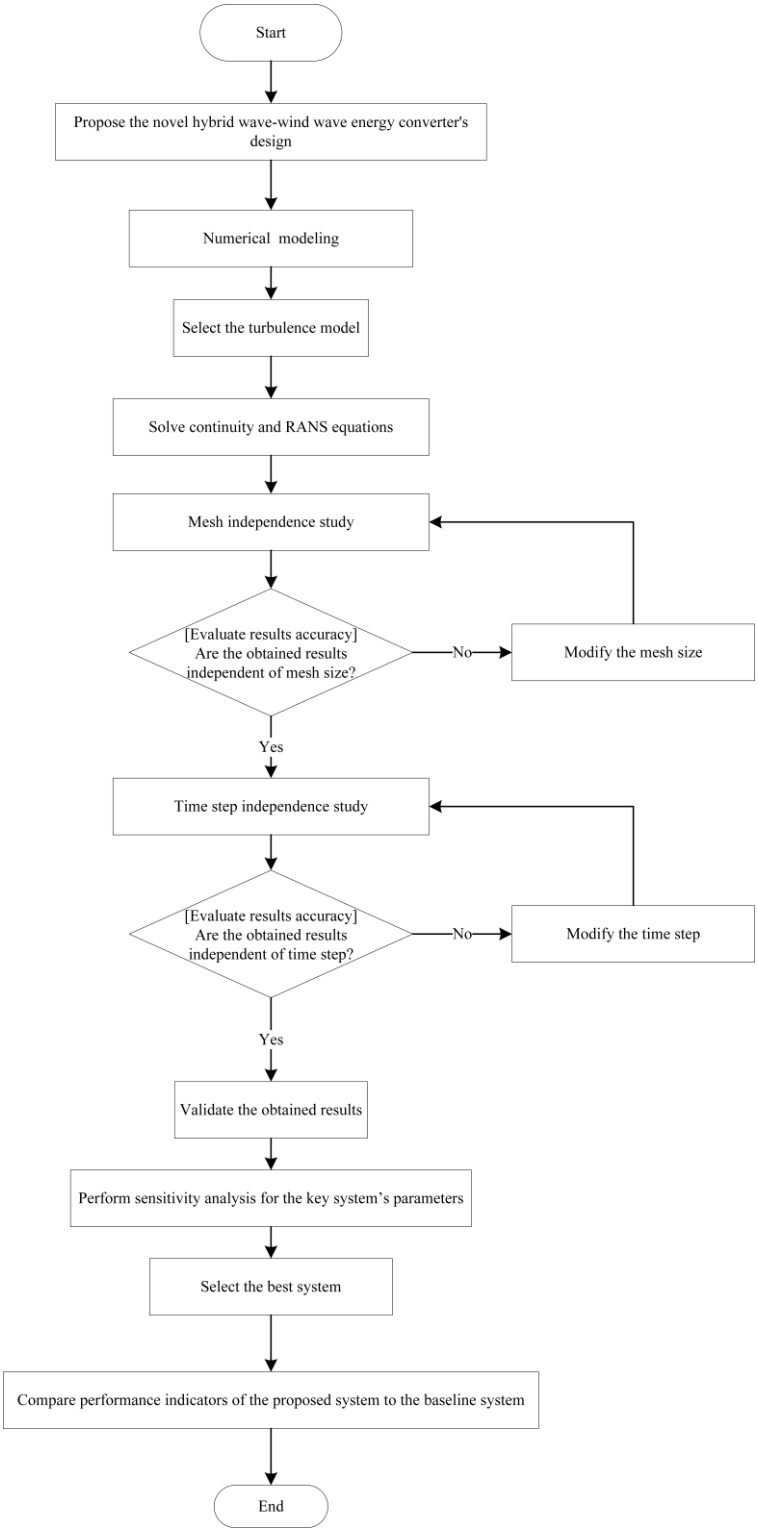

Figure 2-21: The flowchart of the CFD steps and process methodology.

Chapter: 3 Conceptual Design of a Hybrid Wind-Wave Energy Converter

3-1- Introduction

Wave energy, as stated in the literature review chapter, offers significant potential for power generation. Wind, on the other hand, creates waves when it passes over the sea's surface. There is an energy exchange from the wind to the waves as long as the waves spread slower than the wind speed above the waves. Air pressure differential between the upwind and leeward sides of a wave crest, as well as wind friction on the water surface, causes the water to go into shear stress, enabling the waves to increase. Therefore, investigating an integrated system, which employs wind and wave energy as two renewable energy sources to produce power simultaneously, has great importance. In this chapter, the description of investigated system has been proposed. Subsequently, the governing equation of the energy chain process will be discussed.

3-1-1- Windcatcher technology

One of the inspiring structures that can be used in hybrid wave-wind systems, is windcatchers. In this sub-section, the previous studies conducted on the windcatchers are presented. A windcatcher, also known as a wind tower, is a historic architectural component incorporated into buildings to provide air circulation and passive cooling. Windcatchers appear in a range of styles, including unidirectional, bidirectional, and multidirectional, and have been utilized for three thousand years in North Africa and the West Asian regions surrounding the Persian Gulf [71]. The operation of a windcatcher is driven by two fundamental forces: buoyancy force and external wind force, with the latter being the primary factor in windcatcher functioning. The buoyancy effect is a physical phenomenon caused by the presence of interior and exterior temperature differences. The number of openings in a windcatcher impacts its efficiency in such a way that as the number of openings increases, so does its efficiency. Nevertheless,

in areas where there is no predominant wind multi-opening windcatchers are the ideal solution. **Error! Reference source not found.** presents the schematic of a windcatcher [72].

Montazeri [73] investigated the efficiency of a two-sided windcatcher at various wind incidence angles experimentally, numerically, and theoretically. The best performance for a two-sided windcatcher was achieved at 90°, which was approximately 20% higher than at 0°. Also, it was discovered that the pressure coefficients at the windcatcher entrances had a considerable impact on windcatcher performance. The study also looked at the air short-circuiting impact, which was observed at higher air incident angle amounts. In windcatchers, air-short-circuiting happens when air enters via the supply duct and escapes quickly through the exhaust duct without circulation or mixing within the confined compartment, as shown in **Error! Reference source not found.**a. To solve the problem, Nejat et al. [74], presented an anti-short-circuiting device, as shown in **Error! Reference source not found.**b, and studied its ability to remove air short-circuiting in windcatchers and increase ventilation efficiency by CFD modelling and wind tunnel testing. The researchers reported that the windcatcher lacking an anti-short circuit device had an 8% larger CO2 content in the room, indicating that the anti-short circuit device windcatcher was more efficient at eliminating noxious fumes.

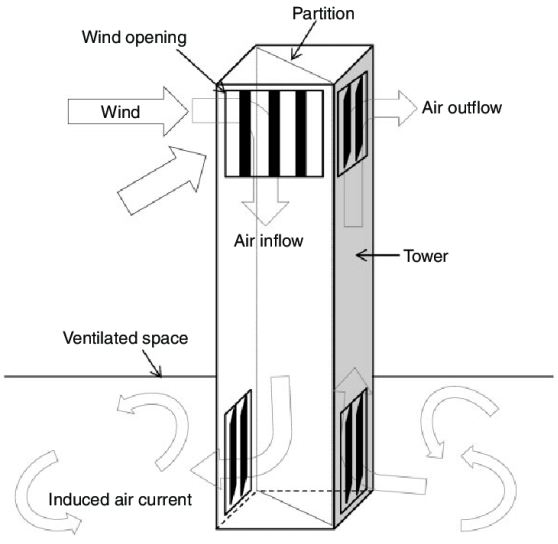

Figure 3-1: schematic of a windcatcher [72].

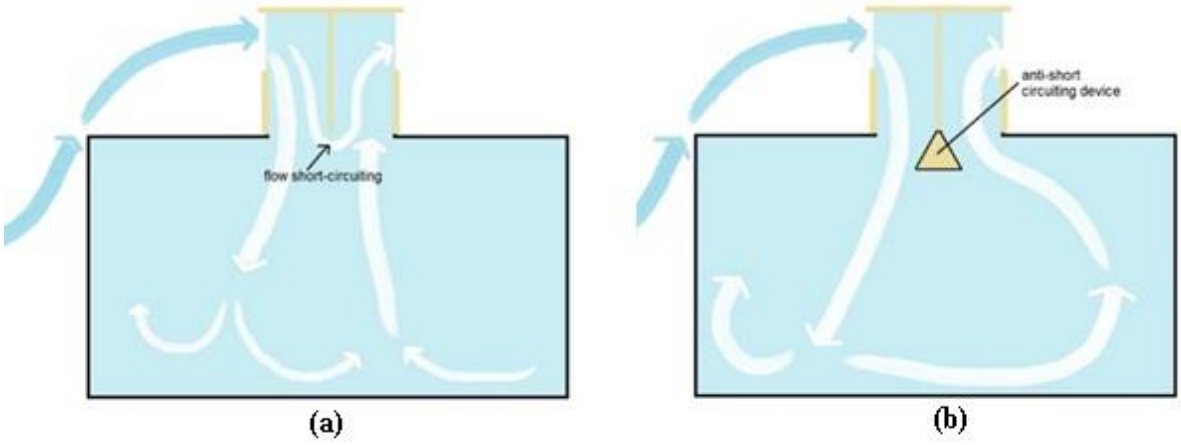

Figure 3-2: Anti-short-circuiting device incorporation in a two-sided windcatcher [75].

3-2- System Description

The proposed innovation in this study consisted of a novel design and the development of a new technique to increase the speed of the airflow within the turbine blades. This is accomplished by creating an innovative location for the turbine to utilize the compressed air produced by the movement of the free surface within a chamber of typical OWCs as well as wind speed on top of the ocean at the same time. This means that, in terms of operation, it would be able to operate both unidirectional and bidirectional turbines with this unique approach. Two different valves are used to adjust the direction of the airflow generated by the compressed airflow from the OWC primary chamber. As shown in **Error! Reference source not found.**, a windcatcher has been integrated into the primary OWC to capture the wind over the ocean and increase the turbine's power generation capability.

For both experimental and numerical modelling, studies like Refs. [76-78] employ an orifice or slot to represent pneumatic damping for Power Takeoff and turbine positioning. Therefore, in this thesis, the same approach has been used. Two distinct orifices are identified on both sides of the chamber in this study, and two valves are assigned to each orifice. The valves are built so that one valve opens when the free surface of water rises and pressurized air within the chamber forces high-speed air to the turbine blades, while the second valve closes at this period. The second valve opens in the second phase once the free surface within the chamber decreases; the air decompression phase begins at this point, and the first valve is closed. While the water level within the primary chamber rises throughout a wave cycle,

the air is compressed, and the first valve opens automatically, forcing airflow to the turbine blades. The second valve will be released to fill the chamber with air throughout the air decompression phase, while the first valve will be blocked. During this step, airflow is captured and sucked into the chamber till the water level returns to normal. Besides, the windcatcher's apertures will remain open throughout the cycle, resulting in a steady airflow rate going through the turbine blades.

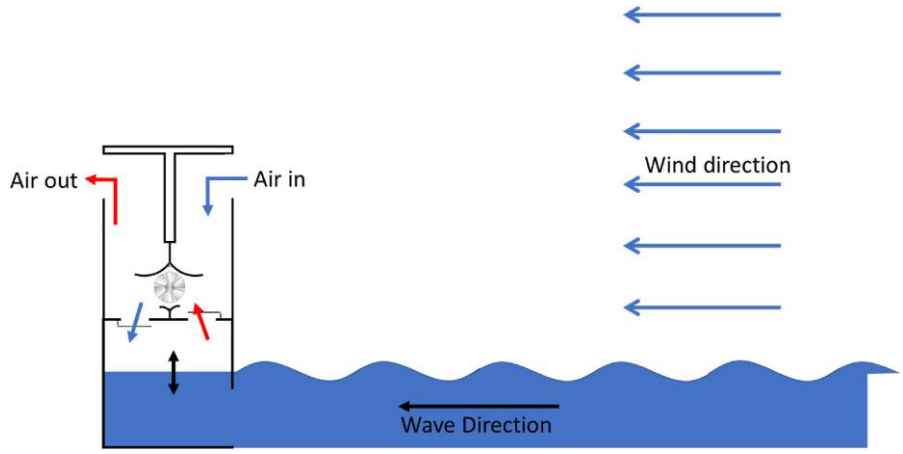

Figure 3-3: Schematic of the innovative OWC integrated with Windcatcher concept.

Fig 3-3 is designed to explain the main concept and parameters used in the research in this thesis. Blue arrows show the air coming to the device and red arrows show the air exiting the device. Red and blue arrows on top of the device demonstrate the inlet and outlet of the windcatcher and the ones on the down part of the device show the inlet and outlet valves and the turbine is placed in between the arrows showing the height and position of the PTO In the analysis performed in this thesis,

A CFD simulation is employed to model the valve opening and closing operation. The simulation procedure consists of two major parts. The left valve opens in the first stage, while the right valve closes. This is the point at which the free surface level of water within the chamber rises, compressing the air. The left valve opens, and the right valve closes in the next phase, which is the phase of air decompression since the free surface decreases inside the chamber. Because the mechanism of opening and closing is all reliant on the direction of the airflow rate, each valve undergoes opening and closing for half of the wave duration. As a result, the only path for airflow to leave the chamber is through the

left valve, and the only way for airflow to enter the chamber is through the right valve. Eventually, the findings from steps one and two are merged to demonstrate a complete interval of air compression and decompression within the chamber.

3-3- Energy Chain Process of Integrated Wave-Wind OWC

It is necessary to evaluate the impact of the converter's dominating variables on the energy conversion chain. Originally, these variables were investigated for the M-OWC, and the impact of modifying the pneumatic damping coefficient, and incoming wave height are also studied. Tseng et al. [79] presented the first wave modelling approach for a MOWC to demonstrate the sequence of energy conversion from the arriving wave to produced energy to the airflow within the Wells turbine. Only 28.5 per cent of the wave energy can be transformed into air energy, according to the model. Elhanafi et al. [64] investigate the influence of construction variables and wave parameters on the hydrodynamic efficiency and energy chain of OWCs in depth. A comprehensive wave-power model is developed in this study, taking into account the impact of the Windcatcher's airflow. This method is a finalized version of the model in [64], with an initial set-up for the design variables to get the highest functionality out of the newly suggested technology. The size of the Windcatcher openings, the height of the innovative PTO component on top of the chamber, the input wave characteristics, and the size of the orifice on top of the chamber are among these variables. By analyzing the energy production from wave energy via the extracted pneumatic power, this research addressed the path for future progression of OWCs integrated with the windcatcher as a single converter.

3-3-1- Energy balance equation in OWCs

It is getting highly necessary to gain a deeper knowledge of the influence that various design variables, including wave amplitude and pneumatic damping, have on the wave energy conversion chain. the OWC energy balance evaluation is carried out under the energy conservation concept, which is based on the idea that energy cannot be generated or destroyed but can be converted from one form to another, as stated in Eq. (3-1). The amount of energy accessible in the approaching waves (E_I) to the system is equivalent to the energy reflected waves by the solid structural elements (E_R), energy collected within

the chamber (E_S), energy converted to electricity from the turbine (E_E), and energy losses in the conversion cycle (E_L), which is based on the energy conversion law. The energy conversion process is given by Eq. (3-1) as follows::

$$E_I = E_R + E_E + E_S + E_L \quad \left[\frac{J}{m}\right] \qquad \text{Eq. (3-1)}$$

The system's input energy is the energy contained in the entering wave, which varies depending on wave height, water density, gravitational force, and wavelength. The relationship between these variables is depicted in Eq. (3-2):

$$E_I = \frac{1}{2}\rho g A^2 L \qquad \text{Eq. (3-2)}$$

where L represents the wavelength, ρ is the water density, g is the gravitational force, A and is the wave height applied at the inlet boundary.

Given that both the incident and reflected energy are related to the square of the wave height, the wave reflection coefficient (C_R) is calculated as the proportion of the reflected wave height (H_R) to the incident wave height (H). To clarify the reflected and incident waves, the instantaneous wave elevation in front of the OWC construction is measured at three sites in accordance with the probe spacing criteria for the Mansard and Funke [80] resolving approaches. With the reflection coefficient, the reflected wave energy may be calculated using Eq. (3-3) as follows:

$$E_R = E_I \times C_R^2 \qquad \text{Eq. (3-3)}$$

where E_A denotes the quantity of wave energy received by the OWC structure. Therefore, Eq. (3-4) indicates the greatest amount of accessible energy to be collected:

$$E_A = E_I - E_R = E_I\left(1 - C_R^2\right) \qquad \text{Eq. (3-4)}$$

Furthermore, the harvested pneumatic energy at the air turbine (E_E) is estimated per wave cycle by combining the instantaneous extracted power over one wave period (T_w), which is obtained by multiplying the instantaneous differential pressure shown by $\Delta P(t)$ among the chamber and the external site and the airflow rate through the turbine indicated by $q(t)$ as expressed in Eq. (3-5) [81]:

$$E_E = \int_0^T \Delta P(t).q(t)dt \qquad \text{Eq. (3-5)}$$

The airflow rate ($q(t)$) inside the turbine duct or orifice of a simplified concept of an OWC is primarily determined by the chamber size, orifice size, and wave properties applied to the inlet boundary; however, other factors, such as the size of the openings, the height of the windcatcher, and the details of the variables within the new system, must be considered when estimating the airflow rate inside the turbine duct of an OWC integrated with a windcatcher [81]. Moreover, the total airflow rate inside the proposed OWC is comprised of the airflow rate provided by the OWC and the flow rate of the windcatcher can be written as in Eq. (3-6):

$$q(t) = q_{OWC}(t) + q_{windcatcher}(t) \qquad \text{Eq. (3-6)}$$

The airflow rate provided by the OWC and windcatcher is calculated by Eq. (3-7) and Eq. (3-8), respectively:

$$q_{OWC}(t) = V_{free\ surface} \times A_{orifice} \qquad \text{Eq. (3-7)}$$

$$q_{windcatcher}(t) = C_d A_e v_H(t)\sqrt{\Delta C_p} \qquad \text{Eq. (3-8)}$$

where C_d is the coefficient of discharge of the opening in the windcatcher, which can be estimated as 0.62, and v_H is the velocity at the windcatcher's top wall, C_p is the difference in the pressure coefficient of the air between both the inlet and the outlet of the windcatcher. Further, the effective area of the

opening (A_e) is expressed in Eq. (3-9) as follows:

$$A_e = \frac{A_1 \times A_2}{\sqrt{A_1^2 + A_2^2}} \quad \text{Eq. (3-9)}$$

where A_1 and A_2 is the area of the inlet and outlet of the windcatcher, respectively.

Eq. (3-10) represents the instantaneous potential energy accumulated in OWC heave oscillation (E_S') apart from its rest position per unit chamber width, whereas Eq. (3-11) provides the average potential/stored energy during one wave interval (*Es*):

$$E_S' = \frac{\rho g \eta^2 b}{2} \quad \text{Eq. (3-10)}$$

$$E_S = \frac{1}{T_w} \int_0^T \frac{\rho g \eta^2 b}{2} dt = \frac{\rho g H_w^2 b}{16} \quad \text{Eq. (3-11)}$$

where b denotes the chamber length, H_w indicates the height of the water column oscillation, and η represents the vertical oscillation of the water volume relocated from the still water level.

According to the energy conservation principle in Eq. (3-1), the total energy losses in the OWC system (E_L) are the portion of the absorbed energy that was not delivered to the air for additional conversion at the turbine excluding the energy stored in the heave movement of the water column, and it is expressed in Eq. (3-12) as:

$$E_L = E_A - E_S - E_E \quad \text{Eq. (3-12)}$$

After defining each energy function in Eq. (3-12), by dividing both sides of Eq. (3-1) by the entering wave energy the dimensionless parameters have been obtained. This gives the various energy balance parameters, as summarized in a series of the equation shown in Eq. (3-13) [64]:

$$\begin{cases} C_{Overall} = \dfrac{E_E}{E_I} \\ C_R^2 = \left(\dfrac{H_R}{H} \right)^2 \\ C_{Abs} = \dfrac{E_A}{E_I} \\ C_{Internal} = \dfrac{E_E}{E_A} \\ C_L = \dfrac{E_L}{E_A} \\ C_S = \dfrac{E_S}{E_A} \end{cases}$$ Eq. (**3**-13)

where $C_{Overall}$ is the overall pneumatic energy extraction, C_R^2 represents the reflected energy, C_{Abs} denotes the OWC energy absorption, $C_{Internal}$ is the OWC internal energy extraction, C_L is the energy losses, and C_S represents the OWC stored energy.

It is worth noting that scholars frequently use the concept of overall efficiency to denote the fraction of time-averaged harvested power (P_E) described in Eq. (3-14) relative to incoming wave power (P_I) described in Eq. (3-15), besides the celerity (C_g) defined in Eq. (3-16) [82]:

$$P_E = \frac{E_E}{T_w}$$ Eq. (**3**-14)

$$P_I = \frac{E_I}{L} C_g$$ Eq. (**3**-15)

$$C_g = \frac{\omega}{2k} \left(1 + \frac{2kh}{\sinh(2kh)} \right)$$ Eq. (**3**-16)

where ω is the angular frequency of the wave, k is the wave number, and h is the depth of the water.

Based on Ref. [83], the energy in the water column heave can be transformed into usable pneumatic energy via the PTO, although some will be emitted as outgoing waves and some will be wasted as viscous losses. This is seen in Eq. (3-13), which shows that there is no direct coupling between the received and retrieved pneumatic power, and the only path to retrieve the absorbed power is via the water column heave movement. As a result, it is advantageous for the majority of cases, if not all of the incoming energy to proceed through this heave movement. As originally demonstrated by Mendes and Monteiro [84], the proportion of extracted energy from given stored heave energy relies mostly on the applied PTO damping, and there is constantly a portion of the stored energy that stays in the mechanism without being transformed to any other kinds, which is provided by Eq. (3-11). Furthermore, as the water elevation within the OWC chamber fluctuates due to continuous PTO damping, the energy stored in the chamber increases and dissipates across the wave cycle, as shown by Eq. (3-10). Therefore, the immediate shift in stored energy changes the several potential sinks for this energy, including pneumatic, reflected, and energy losses.

3-4- Turbine Governing Equations

The turbine experiences a pressure difference of $p_t = p - p_v$, where $|p_v|$ is the pressure loss at the valve. Furthermore, if the valve is completely open or if there is no throttle valve then $p_v = 0$. Without taking into account the influence of fluctuations in Reynolds number and Mach number, the turbine's efficiency properties can be expressed in dimensionless notation as Eq. (3-17) [85]:

$$\Phi = f_w(\Psi), \prod = f_p(\Psi) \qquad \text{Eq. (3-17)}$$

where Φ, Ψ and $\prod$ are dimensionless flow coefficient, pressure coefficient, and power coefficient, respectively, and they are expressed in Eq. (3-18) as:

$$\begin{cases} \Phi = \dfrac{w}{\rho^* N D^3} \\ \Psi = \dfrac{p_t}{\rho^* N^2 D^2} \\ \prod = \dfrac{P}{\rho^* N^3 D^5} \end{cases}$$ Eq. (**3-18**)

The outside diameter of the turbine rotor is shown by D, the rotational speed N, and the power output P. The parameter ρ^* represents a standard density, which is typically the stagnation density at the turbine inlet. The functions f_w f_P are affected by the turbine's geometry but not by its size or rotational speed. Because the turbine is considered to be self-rectifying w and p_t might be positive or negative, as do the associated dimensionless coefficients Φ Ψ.

3-5- Valves Governing Equations

It may be advantageous to use dimensionless parameters to describe the valves' opening positions. Considering that the flow through the valve is completely turbulent, the following Eq. (3-19) is presented [86]:

$$\alpha A_r = \frac{|w_v|}{\sqrt{2\rho|p|}}$$ Eq. (3-**19**)

where αA_r is the valve's useful area of entry, A_r is a reference area, which is equal to $\dfrac{\pi D^2}{4}$, and $w_v = -\dfrac{dm}{dt} - w$ is the flow rate through the valve. The dimensionless parameter α should have the following values as expressed in Eq. (3-20):

$$\begin{cases} \alpha = 0 & if \quad |p| < p_{cr} \\ \alpha = \dfrac{\left|\dfrac{dm}{dt}\right| - w_{cr}}{A\sqrt{2\rho p_{cr}}} & if \quad |p| = p_{cr} \end{cases}$$ Eq. (3-17)

In this case, w_{cr} is the critical value of w that corresponds to the critical pressure (p_{cr}), and it's a positive value.

3-6- Windcatcher Governing Equations

A windcatcher's cross-section is generally either rectangular or circular, but because a windcatcher with a rectangular cross-section performs better than the circular cross-section windcatchers [87], the assessment that follows is confined to rectangular cross-sections. The cross-section is considered to be separated into four segments with openings at the top. Wind at velocity u_w enters the windcatcher at an angle of θ degrees. The windcatcher's cross-sectional dimensions are $d_1 \times d_2$; the length of the opening segment is L_T , and the length from the opening to the bottom L_b . To simulate the operation of a windcatcher, energy and mass conservation are implemented using an approach based on the method reported by Etheridge and Sandberg [88]. The wind is considered to have a zero angle of incidence ($\theta = 0$) to simplify the presentation. For a quadrant that faces the wind, the flow will be from the outside into the chamber, and energy conservation yields are obtained as Eq. (3-21) [88],

$$\Delta p_{in} = p_E - p_I - \Delta\rho g z_I + p_w$$ Eq. (3-18)

where Δp_{in} is the pressure loss across the windcatcher quadrant, p_E and p_I are the exterior and interior pressures, respectively. Moreover, $\Delta\rho$ indicates the difference in air density between the chamber and the exterior, z_I represents the elevation of the entry to the windcatcher from the chamber, relative to the bottom surface of the chamber, and p_w denotes the wind pressure. Furthermore, for a quadrant in which air flows from the chamber to its exterior ad it is expressed as Eq. (3-22):

$$\Delta p_{out} = p_I - p_E + \Delta\rho g z_E - p_w \qquad \text{Eq. (3-19)}$$

where Δp_{out} denotes the pressure loss across the exit quadrant. In particular, the pressure produced by wind impact on the surface of a windcatcher quadrant can be associated with the velocity of air flowing inside or outside of the quadrant using the coefficient of pressure C_p, which is given as Eq. (3-23) [88]:

$$C_p = \frac{2\Delta p}{\rho_E u_w^2} \qquad \text{Eq. (3-220)}$$

In this case, Δp is the difference between the reference pressure and the static pressure on the windcatcher's front (p_w). Consequently, for air flow entering the chamber from the exterior, Eq. (3-18) can be expressed as Eq. (3-24) [88]:

$$\Delta p_{in} = \frac{1}{2}\rho_E u_w^2 C_p - g z_I \left(\rho_E - \rho_I\right) - p_I \qquad \text{Eq. (3-}\mathbf{24}\text{)}$$

Eq. (3-24) further considers that the air velocity outside the chamber is small and that changes in density induced by pressure variation with height can be ignored. Likewise, an output quadrant can be obtained as Eq. (3-25):

$$\Delta p_{out} = p_I - g z_E \left(\rho_I - \rho_E\right) - \frac{1}{2}\rho_E u_w^2 C_p \qquad \text{Eq. (3-}\mathbf{25}\text{)}$$

The density variation shown in Eq. (3-24) and Eq. (3-25) is considered to be exclusively due to temperature fluctuations, therefore Eq. (3-26) can be obtained [88]:

$$\begin{cases} \Delta p_{in} = \dfrac{1}{2}\rho_E u_w^2 C_p - \dfrac{g z_I p_E}{R}\left(\dfrac{1}{T_E} - \dfrac{1}{T_I}\right) - p_I \\ \Delta p_{out} = p_I - \dfrac{g z_E p_E}{R}\left(\dfrac{1}{T_I} - \dfrac{1}{T_E}\right) - \dfrac{1}{2}\rho_E u_w^2 C_p \end{cases} \qquad \text{Eq. (}\mathbf{3\text{-}26}\text{)}$$

where, T represents temperature, while R indicates the air-specific gas constant. The pressure drops

Δp_{in} and Δp_{out} reflects the losses imposed by the windcatcher, which can be stated in a variety of ways, such as employing a standardized loss coefficient [89]. Nevertheless, because the windcatcher has many diverse parts, it is necessary to obtain an understanding of how each part affects the windcatcher function, and so the losses are defined in terms of a loss coefficient K, where in particular Eq. (3-27):

$$K_{in,out} = \frac{2\Delta p_{in,out}}{\rho u^2} \qquad \text{Eq. (3-21)}$$

As a result, Eq. (3-26) can be rearranged as in Eq. (3-28):

$$\begin{cases} \frac{1}{2}\bar{\rho}u_{in}^2 K_{in} = \frac{1}{2}\rho_E u_w^2 C_p - \frac{gz_I p_E}{R}\left(\frac{1}{T_E} - \frac{1}{T_I}\right) - p_I \\ \frac{1}{2}\bar{\rho}u_{out}^2 K_{out} = p_I - \frac{gz_E p_E}{R}\left(\frac{1}{T_I} - \frac{1}{T_E}\right) - \frac{1}{2}\rho_E u_w^2 C_p \end{cases} \qquad \text{Eq. (3-28)}$$

In Eq. (3-28), u_{in} and u_{out} indicate the velocity within the quadrants of an input and output tube, respectively, and $\bar{\rho}$ is an average density value across the length of the quadrant.

3-7- Calculation of the Hydrodynamic Forces Acting on the OWC

Considering water flow is incompressible, inviscid, and irrotational, the hydraulic behavior is described by a series of equations expressed in Eq. (3-29) as follows:

$$\begin{cases} \frac{\partial^2\phi}{\partial x^2} + \frac{\partial^2\phi}{\partial y^2} + \frac{\partial^2\phi}{\partial z^2} = 0 \qquad \textit{for the fluid} \\ \frac{\partial^2\phi}{\partial t^2} + g\frac{\partial\phi}{\partial z} = 0 \qquad \textit{for the free surface} \end{cases} \qquad \text{Eq. (3-29)}$$

Furthermore, the boundary conditions of Eq. (3-29) are given by Eq. (3-30) as,

$$\begin{cases} \dfrac{\partial \phi}{\partial z} = 0 & \textit{for the sea bottom} \\ \dfrac{\partial \phi}{\partial z} = 0 & \textit{for the fixed solid boundary} \\ \dfrac{\partial \phi}{\partial z} = n_z & \textit{for the lower end of OWC} \end{cases} \qquad \text{Eq. (3-22)}$$

Laplace's equation for irrotational flow is represented by Eq. (3-29) and n_z represents the z-component of the unit perpendicular n facing the fluid. If the movement is harmonic with wave frequency ω, the total velocity potential $\phi(x, y, z)$ can be represented by Eq. (3-31) as follows:

$$\phi(x, y, z) = [\varphi_0 + \varphi_S] e^{-i\omega t} + \varphi_r \dot{\eta} \qquad \text{Eq. (3-231)}$$

where $\dot{\eta}$ is the OWC's vertical velocity and φ_0 is the velocity potential for a rising wave due to the flat coastline without the device's regional topography. It can be stated by Eq. (3-32) as follows:

$$\varphi_0 = \frac{2g\zeta_a \cosh k(z+h)}{\omega \cosh kh} \cos(kx \cos\beta) e^{iky \sin\beta} \qquad \text{Eq. (3-24)}$$

β is the angle formed by the incident wave's direction and the positive direction of the x-axis. By fulfilling the boundary conditions, the velocity potential of the waves, φ_S, generated by the regional topography near the system is derived by Eq. (3-33) as,

$$\frac{\partial \varphi_S}{\partial n} = -\frac{\partial \varphi_0}{\partial n} \qquad \text{Eq. (3-33)}$$

The magnitude of the wave generating force on the OWC is represented by Eq. (3-34) as follows:

$$F_d = -\rho \iint i\omega (\varphi_0 + \varphi_S) n_z dS \qquad \text{Eq. (33-325)}$$

The radiation potential's hydrodynamic force impacting the bottom end of the OWC can be represented in terms of additional mass (m) and radiation damping coefficients B. The following relationships as

expressed in Eqs. (3-35) and (3-36) can be used to describe these coefficients:

$$m = -\rho \,\mathrm{Re} \iint n_z \varphi_r dS \qquad \text{Eq. (3-35)}$$

$$\beta = -\rho\omega \,\mathrm{Im} \iint n_z \varphi_r dS \qquad \text{Eq. (3-36)}$$

3-8- OWC Efficiency

Efficiency is calculated by evaluating the output energy and the theoretical input wave energy for a specific situation. Equations for both the theoretical energy of the incident wave and the energy absorbed by the OWC, are provided to calculate efficiency.

McCormick [90] demonstrated that the equations for overall wave energy (E_i) and average incident wave power (P_i) across a wave cycle employing Stokes 2nd order theory are expressed by Eqs. (3-37) and (3-38) as:

$$E_i = \frac{\rho g}{8} H^2 \left[1 + \frac{9H^2}{64k^4 h_w{}^6} \right] \qquad \text{Eq. (3-37)}$$

$$P_i = \frac{\rho g}{8} H^2 c_g b_s \left[1 + \frac{9H^2}{64k^4 h_w{}^6} \right] \qquad \text{Eq. (33-38)}$$

where b_s is the system width, c_g represents the celerity, H denotes the wave height, and h_w is the water depth.

The horizontal size of the inside chamber is considered to be small in comparison to the predominant wavelength, such that the interior water surface is adequately flat in long waves to be regarded as a body in heave. In the case of shorter wavelength waves, the interior surface may be non-flat, causing

the water column to pitch and heave. Although this has ramifications for the system's natural period, the mean energy absorbed by the OWC system is principally determined by the heave movement of the water column and the dynamic air pressures within the system. Brendmo et al. [91] demonstrated that, albeit it's an estimation, it provides remarkable consistency when the wavelengths under discussion are long in comparison to the basic horizontal size of the interior OWC surface. As a result, considering that the interior surface of the OWC operates as a piston, the hydrodynamic energy (p_{hyd}) absorbed by the OWC may be calculated using the basic energy formulation given by Eq. (3-39) as,

$$Power = \frac{Force \times displacement}{Time} \qquad \text{Eq. (33-39)}$$

Eq. (3-39) can be rewritten by replacing the product of $Pressure$ and $Area$ for $Force$ and considering that the hydrodynamic energy is transmitted to the air column and it is expressed as Eq. (3-40):

$$P_{hyd} = Pressure \times Area. \frac{dS}{dT} \qquad \text{Eq. (3-26}\mathbf{0}\text{)}$$

where $Area$ is the surface area of the water level within the chamber, $Pressure$ represents the pressure inside the chamber, and $\frac{dS}{dT}$ denotes the differentiated position of the water level within the chamber or the velocity of the OWC piston.

As a result, knowing the pressure generated within the chamber and the surface fluctuations inside the chamber, the hydrodynamic power transferred to the OWC can be calculated. Because this is a forced oscillation situation, the OWC oscillations have the same frequency as the incoming wave. The pressure generated within the system will have the same frequency as well, although there may be a phase mismatch between the pressure and flow rate.

The absorbed energy with regard to time is calculated by multiplying pressure by flow rate. The mean of this absorbed energy across an integer multiple of wave cycles yields the mean p_{hyd} of the OWC for

the situations under consideration.

In application, the OWC efficiency after the next stage of conversion can be measured by evaluating the power flux of the turbine. Due to numerical challenges in modeling a turbine in this study, a basic orifice was used to demonstrate representational similarities to the pressure drop related to the airflow flowing through a turbine. Considering that the studies focus on hydrodynamic rather than pneumatic conversion efficiency, this is deemed acceptable.

The power at the orifice ($P_{orifice}$), can be calculated by Eq. (3-41) as follows:

$$P_{orifice} = Pressure \times \int velocity.dA \qquad \text{Eq. (33-27)}$$

This finding is rather theoretical for experimental work because it is nearly impractical to correctly quantify the air velocity profile across the orifice. It is nevertheless of importance when undertaking numerical assessment since it is easy to identify all relevant parameters and a comparison with the hydrodynamic energy may give an indicator of the system's pneumatic losses.

The efficiency of a system is determined by the ratio of the energy received by the system to the energy incident on it. This is defined as ε_{hyd} and has been calculated by Eq. (3-42) as follows:

$$\varepsilon_{hyd} = \frac{P_{hyd}}{P_{wave}} \qquad \text{Eq. (3-28}\mathbf{2}\text{)}$$

Chapter: 4 Research Methodology

4-1- Introduction

Wave energy converters are a modest but potentially substantial part of the worldwide renewable energy mix. Nevertheless, to compete with offshore wind or solar power, the WEC industry will need to develop effective prototypes, which will prepare the path for up-scaled commercialization and the use of economies of scale. To accurately evaluate performance indicators during the initial design phases, this path necessitates the use of precise and trustworthy numerical modelling approaches.

The three primary methodologies for numerical modelling of WECs are linear and nonlinear potential flow concepts, fully nonlinear potential flow concepts, and computational fluid dynamics (CFD), which solves the Navier–Stokes equations for single-phase or two-phase fluids. The key challenge with CFD approaches is accurately resolving the two-phase fluid interface between the water and air within the chamber, especially if the air phase is compressible. CFD Navier-Stokes models, which have a significant computational cost but may attain great accuracy when analyzing fully nonlinear systems [16], are the most sophisticated class of numerical models. As processing power improves, these methods can now be used to address current engineering challenges [92].

When compared to practical experiments, numerical modelling can provide more detailed information and has no scaling limits. The first results provided by CFD must be confirmed against experimental data, which is the primary restriction in numerical CFD modelling. The major findings are verified with [70], and a series of numerical studies on the efficiency of the novel developed converter is then examined in depth.

4-2- Governing Equations

To solve the continuity and momentum equations, a numerical CFD program is built in this research utilizing Ansys Fluent. The influence of air compressibility has been ignored in the suggested CFD

model because it only exists in large-scale models [59, 93-96]. To monitor the interaction of water and air in simulations, RANS and continuity equations are implemented in the modelling, and Volume OF Fluid is engaged to calculate and analyze the motion of the free surface level of water and air. The mass conservation equation, generally referred to as the continuity equation, is defined by Eq. (4-1) as follows:

$$\frac{\partial \rho}{\partial t} + \nabla.\left(\rho \vec{v}\right) = S_m \qquad \text{Eq. (4-1)}$$

Where ρ is density, $\vec{v}$ velocity, and S_m is the source term. The mass conservation equation, in its basic version, is applicable for both incompressible and compressible flows. The source term S_m is the mass delivered to the continuous phase from the distributed second phase. The continuity equation is provided for two-dimensional axially symmetric geometry as Eq. (4-2) [97]:

$$\frac{\partial \rho}{\partial t} + \frac{\partial}{\partial x}\left(\rho v_x\right) + \frac{\partial}{\partial r}\left(\rho v_r\right) + \frac{\rho v_r}{r} = S_m \qquad \text{Eq. (4-2)}$$

where x represents the axial coordinate, r denotes the radial coordinate, v_x reflects the axial velocity, and v_r represents the radial velocity.

Moreover, the conservation of momentum for a non-accelerating regime known as the internal reference frame is presented as Eq. (4-3) [97]:

$$\frac{\partial}{\partial t}\left(\rho \vec{v}\right) + \nabla.\left(\rho \vec{v}\vec{v}\right) = -\nabla p + \nabla.\left(\bar{\tau}\right) + \rho \vec{g} + \vec{F} \qquad \text{Eq. (4-3)}$$

where p is the static pressure, $\rho \vec{g}$ and $\vec{F}$ are the gravitational body force and external body forces, caused by interaction with the dispersion phase. $\bar{\tau}$ denotes the stress tensor and obtained as Eq. (4-4),

$$\bar{\tau} = \mu\left[\left(\nabla \vec{v} + \nabla \vec{v}^{T}\right) - \frac{2}{3}\nabla.\vec{v}I\right] \qquad \text{Eq. (4-4)}$$

where μ denotes molecular viscosity, I represents unit tensor, and the second term on the right-hand side denotes the impact of volume dilation. The axial and radial momentum conservation equations for two-dimensional axially symmetric geometry are presented in **Error! Reference source not found.** and **Error! Reference source not found.**, respectively:

$$\frac{\partial}{\partial t}\left(\rho v_x\right)+\frac{1}{r}\frac{\partial}{\partial x}\left(r\rho v_x v_x\right)+\frac{1}{r}\frac{\partial}{\partial r}\left(r\rho v_r v_x\right)=-\frac{\partial p}{\partial x} +\frac{1}{r}\frac{\partial}{\partial x}\left[r\mu\left(2\frac{\partial v_x}{\partial x}-\frac{2}{3}\left(\nabla.\vec{v}\right)\right)\right]+\frac{1}{r}\frac{\partial}{\partial r}\left[r\mu\left(\frac{\partial v_x}{\partial r}+\frac{\partial v_r}{\partial x}\right)\right]+F_x \qquad \text{Eq. (4-5)}$$

$$\frac{\partial}{\partial t}\left(\rho v_r\right)+\frac{1}{r}\frac{\partial}{\partial x}\left(r\rho v_x v_r\right)+\frac{1}{r}\frac{\partial}{\partial r}\left(r\rho v_r v_r\right)=-\frac{\partial p}{\partial r} +\frac{1}{r}\frac{\partial}{\partial r}\left[r\mu\left(2\frac{\partial v_r}{\partial r}-\frac{2}{3}\left(\nabla.\vec{v}\right)\right)\right]+\frac{1}{r}\frac{\partial}{\partial x}\left[r\mu\left(\frac{\partial v_r}{\partial x}+\frac{\partial v_x}{\partial r}\right)\right]+F_r \qquad \text{Eq. (4-6)}$$

where $\nabla.\vec{v}$ is defined as Eq. (4-7),

$$\nabla.\vec{v}=\frac{\partial v_x}{\partial x}+\frac{\partial v_r}{\partial r}+\frac{v_r}{r} \qquad \text{Eq. (4-7)}$$

4-2-1- Choosing a turbulence model

Turbulent flows are defined by their fluctuating velocity fields. These changes mix transmitted quantities like momentum, energy, and species concentration, causing them to fluctuate as well. These oscillations are too computationally pricey to model properly in actual engineering calculations due to their small dimension and excessive frequency. Alternatively, the instantaneous governing equations can be time-averaged, ensemble-averaged, or otherwise modified to reduce the resolution of small scales, yielding a unique series of equations that are computationally less pricey to compute. Nonetheless, the revised equations include extra unknown variables, which must be determined in terms of known quantities using turbulence models. However, no single turbulence model is exclusively recognized as preferable for all types of problems. The physics contained in the flow, the known procedure for a certain type of problem, the level of precision necessary, the attainable computer

resources, and the amount of time given for the simulation will all influence the selection of the turbulence model [98].

Time-dependent Navier-Stokes equation solutions for high Reynolds-number turbulent flows in complicated geometries that aim to converge to the smallest scales of the motions are difficult to be achieved for some time. To make the Navier-Stokes equations solvable so that small-scale turbulent fluctuations do not have to be manually simulated, two methods can be used, namely the Reynolds-averaging approach and filtering approach. Both strategies incorporate new terms into the governing equations that must be modelled. The Reynolds-averaged Navier-Stokes (RANS) formulas determine the transport of averaged flow characteristics over the entire range of turbulence sizes. As a result, the RANS-based simulation technique significantly decreases the associated computational cost and resources, and it is frequently used in actual engineering situations. In ANSYS FLUENT, a complete series of models are accessible, comprising Spalart-Allmaras, $k-\varepsilon$ and its variants, $k-\omega$ and its variants, and the Reynolds stress model (RSM). The RANS concept is frequently used to compute time-dependent flows with unsteadiness [99].

The large eddy simulation (LES) is an alternate technique that directly computes big eddies in a time-dependent simulation utilizing the Navier-Stokes equations that have been filtered. The logic underlying LES is that by simulating less turbulence, the inaccuracy generated by turbulence modeling can be decreased. It is also considered to be simpler to establish a universal model for small scales since they are more isotropic and less influenced by macroscopic characteristics such as boundary conditions than larger eddies. Filtering is a mathematical adjustment of the exact Navier-Stokes equations to eliminate eddies smaller than the filter size, which is commonly regarded as the mesh size when spatial filtering is being used, like in ANSYS FLUENT. The filtering mechanism, like Reynolds-averaging, introduces new unknown terms that must be represented in order to attain closure [100].

LES for high Reynolds number flows necessitates a substantial amount of computer capacity. This is mostly due to the requirement to precisely resolve the energy-containing turbulent eddies in both the space and time domains, which becomes especially important in near-wall areas where the scales to be handled become much smaller. Wall functions combined with a coarse near-wall mesh can be used to

lower the cost of LES for wall-bounded flows, with varying degrees of effectiveness. Nonetheless, the effects of utilizing wall functions for the flow in issue must be carefully considered. LES, for the same reasons, needs extremely precise spatial and temporal discretization [101].

4-2-1-1- The Reynolds averaging concept

The solution variables in the instantaneous Navier-Stokes equations are divided into mean (time-averaged) and fluctuating components in Reynolds averaging. The velocity components are expressed in Eq. (4-8) as follows [102]:

$$u_i = \overline{u}_i + u_i' \qquad \text{Eq. (4-8)}$$

where $\overline{u}_i$ and u_i' denote the mean and fluctuating velocity components, respectively. The same is true for pressure and other scalar quantities expressed by Eq. (4-9):

$$\phi = \overline{\phi} + \phi' \qquad \text{Eq. (4-9)}$$

The averaged momentum equations are obtained by substituting equations of this form for the flow parameters into the instant continuity and momentum equations and taking a time average. In Cartesian form, they are expressed by Eq. (4-10) as follows [102]:

$$\frac{\partial \rho}{\partial t} + \frac{\partial}{\partial x_i}\left(\rho u_i\right) = 0 \qquad \text{Eq. (4-10)}$$

$$\frac{\partial}{\partial t}\left(\rho u_i\right) + \frac{\partial}{\partial x_j}\left(\rho u_i u_j\right) = -\frac{\partial p}{\partial x_i} + \frac{\partial}{\partial x_j}\left[\mu\left(\frac{\partial u_i}{\partial x_j} + \frac{\partial u_j}{\partial x_i} - \frac{2}{3}\delta_{ij}\frac{\partial u_i}{\partial x_j}\right)\right] + \frac{\partial}{\partial x_j}\left(-\rho\overline{u_i' u_j'}\right) \qquad \text{Eq. (4-11)}$$

Error! Reference source not found. and **Error! Reference source not found.** are known as the Reynolds-averaged Navier-Stokes (RANS) equations. They have the same fundamental format as the instantaneous Navier-Stokes equations, except that the velocities and other solution variables are now time-averaged. Additional phrases that represent the consequences of turbulence have now appeared. To solve Eq. (4-2) to Eq. (4-4), these Reynolds stresses ($-\rho\overline{u_i' u_j'}$) must be modelled.

The Reynolds-averaged technique to turbulence modelling necessitates accurate modelling of the

Reynolds stresses in **Error! Reference source not found.**. The Boussinesq theory [103] is a typical approach for relating Reynolds stresses to mean velocity gradients, which is shown as Eq. (4-12):

$$-\rho\overline{u_i'u_j'} = \mu_t\left(\frac{\partial u_i}{\partial x_j}+\frac{\partial u_j}{\partial x_i}\right)-\frac{2}{3}\left(\rho k+\mu_t\frac{\partial u_k}{\partial x_k}\right)\delta_{ij} \qquad \text{Eq. (4-12)}$$

The Boussinesq hypothesis is employed in the Spalart-Allmaras model, as well as the $k-\varepsilon$ and $k-\omega$ concepts. The benefit of this method is the minimal computer cost involved with computing the turbulent viscosity, which is shown by μ_t. Only one extra transport equation (representing turbulent viscosity) is addressed in the Spalart-Allmaras approach. In the $k-\varepsilon$ and $k-\omega$ concepts, two extra transport equations are solved. In the case of $k-\varepsilon$ the model, the turbulence kinetic energy (k) and the turbulence dissipation rate (ε) should be solved, while in $k-\omega$ the model the turbulence kinetic energy (k) and the specific dissipation rate (ω) should be resolved. The Boussinesq theory as described has the problem of assuming μ_t is an isotropic scalar quantity, which is not exactly correct [104].

The alternative technique, as incorporated in the RSM, is to calculate transport equations for each term in the Reynolds stress tensor. An additional scale-determining equation is also needed. This implies that five more transport equations must be calculated in 2D models and seven extra transport equations must be resolved in 3D models [105].

In many circumstances, models relying on the Boussinesq hypothesis outperform simulations based on the RSM, and the additional computational cost of the RSM is not justified. The RSM is preferable in cases when turbulence anisotropy has a significant impact on the mean flow [104]. High-swirling flows and stress-driven secondary flows are examples of such circumstances.

Since the shear-stress transport (SST) $k-\omega$ model is used in this study, this concept will be discussed in further detail in the following subsection.

4-2-2- Shear-stress transport (SST) $k-\omega$ model

Menter [100] proposed the shear-stress transport (SST) $k-\omega$ concept to efficiently integrate the resilient and precise formulation of the $k-\varepsilon$ model in the near-wall area with the free-stream

independence of the $k-\varepsilon$ concept in the far-field. The $k-\varepsilon$ model is turned into the $k-\omega$ formulation to accomplish this. The SST model is similar to the standard model, but with the following enhancements [106]:

1- In the ω equation, the SST model includes a damped cross-diffusion derivative factor.

2- The description of turbulent viscosity is changed to account for turbulent shear stress transmission.

3- The modelling constants are not the same.

These properties enable the SST $k-\omega$ approach more precise and consistent for a broader range of flows (e.g., adverse pressure gradient flows, airfoils, and transonic shock waves) than the standard $k-\omega$ model. Other changes include the inclusion of a cross-diffusion factor in the ω equation as well as a blending function to guarantee that the model behaves correctly in both the near-wall and far-field regions.

The transport equations for the SST $k-\omega$ model are given as Eq. (4-13) [107]:

$$\begin{cases} \dfrac{\partial}{\partial t}(\rho k)+\dfrac{\partial}{\partial x_i}(\rho k u_i)=\dfrac{\partial}{\partial x_j}\left(\Gamma_k \dfrac{\partial k}{\partial x_j}\right)+\tilde{G}_k-Y_k+S_k \\ \dfrac{\partial}{\partial t}(\rho \omega)+\dfrac{\partial}{\partial x_i}(\rho \omega u_i)=\dfrac{\partial}{\partial x_j}\left(\Gamma_\omega \dfrac{\partial \omega}{\partial x_j}\right)+G_\omega-Y_\omega+D_\omega+S_\omega \end{cases} \quad \text{Eq. (4-13)}$$

$\tilde{G}_k$ in these equations indicates the production of turbulence kinetic energy caused by mean velocity gradients. G_ω denotes the creation of ω, as discussed. The effective diffusivity of k and ω is represented by Γ_k and Γ_ω, which are determined as detailed below. Y_k and Y_ω reflect the turbulence-induced dissipation of k and ω. The cross-diffusion term, denoted by D_ω, is determined as detailed below. S_k and S_ω are source terms that have been specified by the user.

The effective diffusivities for the SST $k-\omega$ model are provided in Eq. (4-14) [107]:

$$\begin{cases} \Gamma_k = \mu + \dfrac{\mu_t}{\sigma_k} \\ \Gamma_\omega = \mu + \dfrac{\mu_t}{\sigma_\omega} \end{cases} \qquad \text{Eq. (4-14)}$$

where σ_k and σ_ω represent the turbulent Prandtl numbers for k and ω. μ_t is the turbulent viscosity, and it is calculated by Eq. (4-15) [108]:

$$\mu_t = \frac{\rho k}{\omega} \frac{1}{\max\left[\dfrac{1}{\alpha^*}, \dfrac{SF_2}{\alpha_1 \omega}\right]} \qquad \text{Eq. (4-15)}$$

where S denotes the strain rate magnitude. Besides, σ_k and σ_ω are obtained as Eqs. (4-16) and (4-17) [109]:

$$\sigma_k = \frac{1}{\dfrac{F_1}{\sigma_{k,1}} + \dfrac{(1-F_1)}{\sigma_{k,2}}} \qquad \text{Eq. (4-16)}$$

$$\sigma_\omega = \frac{1}{\dfrac{F_1}{\sigma_{\omega,1}} + \dfrac{(1-F_1)}{\sigma_{\omega,2}}} \qquad \text{Eq. (4-17)}$$

The coefficient α^* dampens turbulent viscosity, resulting in a low-Reynolds-number adjustment. It is provided as Eq. (4-18):

$$\alpha^* = \alpha_\infty^* \left(\frac{0.024 + \dfrac{\mathrm{Re}_t}{6}}{1 + \dfrac{\mathrm{Re}_t}{6}} \right) \qquad \text{Eq. (4-18)}$$

in which (Eq. (4-19)):

$$\mathrm{Re}_t = \frac{\rho k}{\mu \omega} \qquad \text{Eq. (4-19)}$$

It is worth noting that in the high-Reynolds-number form of the $k-\omega$ model, $\alpha^* = \alpha_\infty^* = 1$ [109].

Furthermore, the blending functions, F_1 and F_2, are defined by Eqs. (4-20) and (4-21) as follows [110]:

$$\begin{cases} F_1 = \tanh\left\{\left(\min\left[\max\left(\dfrac{\sqrt{k}}{0.09\omega y}, \dfrac{500\mu}{\rho y^2 \omega}\right), \dfrac{4\rho k}{\sigma_{\omega,2} D_\omega^+ y^2}\right]\right)^4\right\} \\ D_\omega^+ = \max\left[2\rho \dfrac{1}{\sigma_{\omega,2}} \dfrac{1}{\omega} \dfrac{\partial k}{\partial x_j} \dfrac{\partial \omega}{\partial x_j}, 10^{-10}\right] \end{cases} \qquad \text{Eq. (4-20)}$$

$$F_2 = \tanh\left\{\left(\max\left[2\frac{\sqrt{k}}{0.09\omega y}, \frac{500\mu}{\rho y^2 \omega}\right]\right)^2\right\} \qquad \text{Eq. (4-21)}$$

where y represents the distance to the adjacent surface, while D_ω^+ denotes the positive portion of the cross-diffusion term, which will be discussed later in this chapter [110].

4-2-2-1- Turbulence generation modelling

As seen in previous equations, $\tilde{G}_k$ denotes the generation of turbulence kinetic energy and is defined by Eq. (4-22) as follows [111]:

$$\tilde{G}_k = \min\left(G_k, 10\rho\beta^* k\omega\right) \qquad \text{Eq. (4-22)}$$

where G_k refers to the kinetic energy produced by turbulence. This term can be defined using the exact equation for the transport of k as Eq. (4-23):

$$G_k = -\rho\overline{u_i' u_j'} \frac{\partial u_j}{\partial x_i} \qquad \text{Eq. (4-23)}$$

To estimate G_k under the Boussinesq theory by Eq. (4-24):

$$G_k = \mu_t S^2 \qquad \text{Eq. (4-24)}$$

where S is the modulus of the mean rate-of-strain tensor, calculated similarly to the $k-\varepsilon$ concept.

Besides, G_ω denotes the generation ω is defined by Eq. (4-25) as follows:

$$G_\omega = \frac{\alpha}{\nu_t}\tilde{G}_k \qquad \text{Eq. (4-25)}$$

This formulation deviates from the standard $k-\omega$ concept. The way the term α_∞ is calculated differs between the two models as well. α_∞ is specified as a constant in the standard $k-\omega$ approach (i.e, 0.52). While α_∞ for the SST $k-\omega$ model is provided by Eq. (4-26) as:

$$\alpha_\infty = F_1\alpha_{\infty,1} + \left(1-F_1\right)\alpha_{\infty,2} \qquad \text{Eq. (4-26)}$$

where $\alpha_{\infty,1}$ and $\alpha_{\infty,2}$ are defined by Eq. (4-27) as follows [111]:

$$\begin{cases} \alpha_{\infty,1} = \dfrac{\beta_{i,1}}{\beta_\infty^*} - \dfrac{0.1681}{\alpha_{\omega,1}\sqrt{\beta_\infty^*}} \\ \alpha_{\infty,2} = \dfrac{\beta_{i,2}}{\beta_\infty^*} - \dfrac{0.1681}{\alpha_{\omega,2}\sqrt{\beta_\infty^*}} \end{cases} \qquad \text{Eq. (4-27)}$$

4-2-2-2- Turbulence dissipation modelling

Y_k denotes the dissipation of turbulence kinetic energy and is calculated in the same way as the standard $k-\omega$ model. The distinction is in how the phrase $f_\beta{}^*$ is assessed. $f_\beta{}^*$ is described as a piecewise function in the standard $k-\omega$ approach. $f_\beta{}^*$ is a constant equal to one in the SST $k-\omega$ concept. Therefore, it can be expressed as Eq. (4-28) [112]:

$$Y_k = \rho\beta^* k\omega \qquad \text{Eq. (4-28)}$$

where Y_ω indicates the dissipation of ω and is derived in the same way as the standard $k-\omega$ approach. The distinction is in how the β_i f_β are assessed. β_i is specified as a constant in the standard

$k-\omega$ concept (i.e., 0.072) [112]. f_β is a constant equal to one in the SST $k-\omega$ model. Hence, Eq. (4-29) is obtained:

$$Y_\omega = \rho\beta\omega^2 \qquad \text{Eq. (4-29)}$$

As opposed to assigning a fixed value β_i, it is provided by Eq. (4-30) as:

$$\beta_i = F_1\beta_{i,1} + (1-F_1)\beta_{i,2} \qquad \text{Eq. (4-30)}$$

whereas shown before, F_1 is obtained from **Error! Reference source not found.**.

4-2-3- Volume Fraction Equation

The answer of a continuity equation for the volume fraction of one of the phases is used to trace the interface between the phases. This formula has the following structure for the q^{th} phase as shown in Eq. (4-31) [113]:

$$\frac{\partial}{\partial t}\left(\alpha_q\rho_q\right) + \nabla.\left(\alpha_q\rho_q\vec{v}_q\right) = S_{\alpha_q} + \sum_{p=1}^{n}\left(\dot{m}_{pq} - \dot{m}_{qp}\right) \qquad \text{Eq. (4-31)}$$

in which $\dot{m}_{qp}$ represents the mass transmission from phase q to phase p and $\dot{m}_{pq}$ reflects the mass transfer from phase p to phase q. The volume fraction equation for the primary phase will not be resolved; instead, the volume fraction for the primary phase will be determined using the given constraint as shown in Eq. (4-32) [114]:

$$\sum_{q=1}^{n}\alpha_q = 1 \qquad \text{Eq. (4-32)}$$

Eq. (4-32) can be calculated either implicitly or explicitly by time discretization.

4-3- Numerical Set up steps

The following steps are implemented in this research in all simulations, and it is based on the provided

information and in this section:

1. Defining the geometry in DesignModeller in ANSYS
2. Finding and choosing the right mesh
3. Set up the Fluent software including choosing the right turbulence model
4. Performing the mesh independence analysis to ensure our results are independent of the mesh size and details
5. If enough accuracy is obtained, perform a time-step independence analysis to ensure our results are independent of the changing in time steps
6. Performing the sensitivity analysis for the parameters like the length of the flume tank and outlets to ensure they have no negative effect on the output results

Chapter: 5 Numerical Modeling

5-1- Introduction

Numerical modelling can provide more detailed information and has no scaling limits compared to practical experiments. The first results provided by CFD must be confirmed against experimental data, which is the primary restriction in numerical CFD modelling. The major findings are verified with [70], and a series of numerical studies on the efficiency of the novel developed converter is then examined in depth. This chapter covers the following:

- Simulation validation and verification including simulation physics set up, mesh and time step independence analysis.
- A summary of the details and set-up of the type of analysis has been done in this thesis which will be discussed in more detail later in Chapter 6.

5-2- Simulation Studies

Based on the findings in Refs [64, 70], a two-dimensional numerical domain is developed to validate the model and evaluate the performance of the novel system to that of the conventional OWC system. Because the pressure required to compress the air density within the system is small, air and water compressibility is regarded as insignificant. Nonetheless, because air compressibility might influence system performance, this factor should be included when analyzing full-scale systems [58]. The numerical domain is divided into three distinct areas, including the water's free surface, the chamber area to model air compression and decompression, and the windcatcher and its surroundings. The domain's length is 4.5m, while its height is considered to be 27.197m. The distance between the boundaries is assumed to be high enough to avoid the unfavourable impact of boundary conditions on the outcomes of probs located within the converter and other measurements for inlet parameters like wind and wave. The front lip of the converter is 14.596m away from the inlet boundary, while the

domain exit is 12.433m away from the backside lip of the system. Moreover, the height of the free surface area is assumed three times the wave height in all calculations. The orifice that models the converter's PTO is 2.5mm in diameter.

The quadrilateral component is developed for the entire domain with a size of 200mm for the air area far from the system, 100mm for the water and windcatcher areas, and 2mm for the areas within the free surface and inside the windcatcher. Due to the extreme priority of having high-quality elements in such places, an aspect ratio of less than 4 was attained. The total number of mesh elements is calculated to be 1582247.

In the Ansys 19 R2 software package, the transient mode of modelling in two-dimensional form has been used for the simulation. An open channel flow with boundary conditions was used to simulate wave propagation, as well as a tank developed for a variety of wind and wave conditions. The calculations employed a linear form of waves with wave heights, wave periods, and water depths of 0.04m, 1.4s, and 0.42m, respectively. The inlet boundary is specified as velocity-inlet, and segregated velocity input was used to model the airflow within the domain, with an initial wind speed of 0.85m/s added to the simulation. Non-slip walls have been used, and the outlet boundary is adjusted to a pressure outlet. The SST $k-\omega$ in the format of a two-equation was used to simulate the turbulent viscosity of incompressible air and water. The multi-phase approach is used to simulate the wave oscillations within the specified tank, with the volume of fluid open channel flow and open channel wave boundary conditions including implicit volume fraction parameters. At the back of the system, a numerical beach of one wavelength length is created and adjusted. Furthermore, the initial condition for water depth, wave height, the wavelength at the inlet boundary, atmospheric pressure, and water depth at the top and outflow boundary conditions are all set. **Error! Reference source not found.** shows the computational domain and the employed mesh for each part of the proposed system.

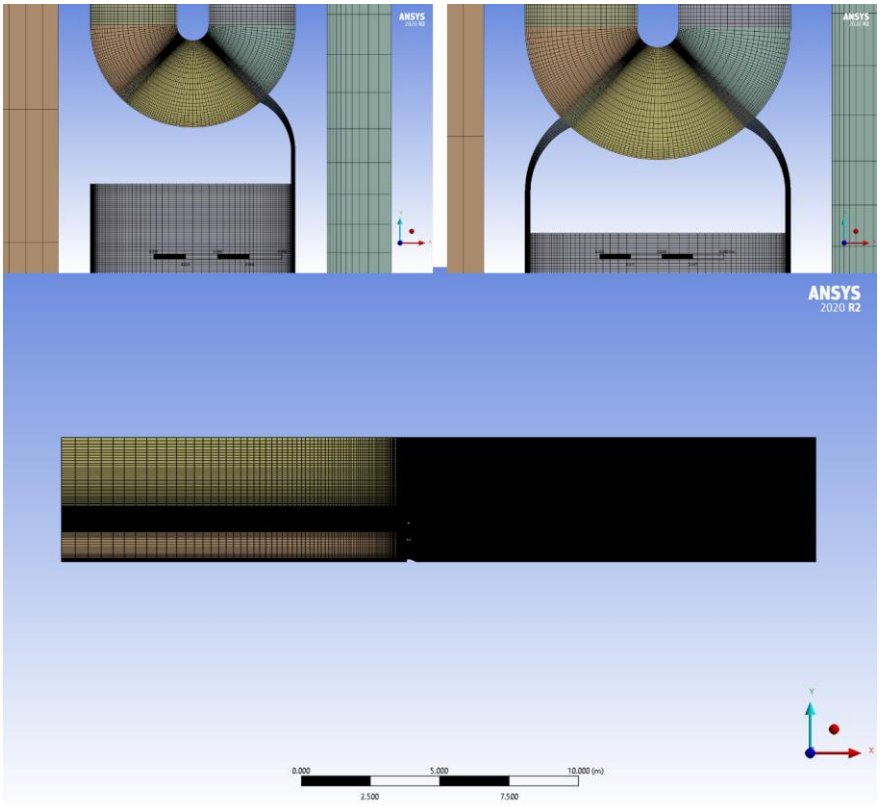

Figure 5-1: Schematic of the innovative OWC integrated with Windcatcher concept.

5-3- Mesh Independence Analysis

Mesh independence evaluation is a critical stage in CFD studies. Besides, mesh independence assessment is performed to demonstrate that a solution is not affected by the geometry grid size. It should be noted that consistency between a predicted simulation and experimental results does not always imply that the result is mesh-independent [115].

Four mesh sizes of 185897 (grid #1), 421813 (grid #2), 745778 (grid #3), and 1772280 (grid #4) were relatively investigated in the mesh independence study conducted. **Error! Reference source not found.** depicts the airflow rate results for the left valve (LV) for simulations of the selected grid sizes. As shown, the simulation results of the grid with sizes of 745778 and 1772280 are in good agreement. However, to fully assure the accuracy of the desired grid size, the maximum error of results of each grid size has been calculated and summarized in **Error! Reference source not found.**. As seen, for the airflow rate results for the left valve, grid #3 has an error of 3.29 per cent compared to grid #4, which

is within the acceptable margin. Considering the computational cost, grid #3 offers a better choice.

Table 5-1: Accuracy comparison of each selected grid size compared to the next grid size for the airflow rate results for the left valve (LV)

	Grid #1 compared to grid #2	Grid #2 compared to grid #3	Grid #3 compared to grid #4
Maximum error (%)	9.97	6.53	3.29

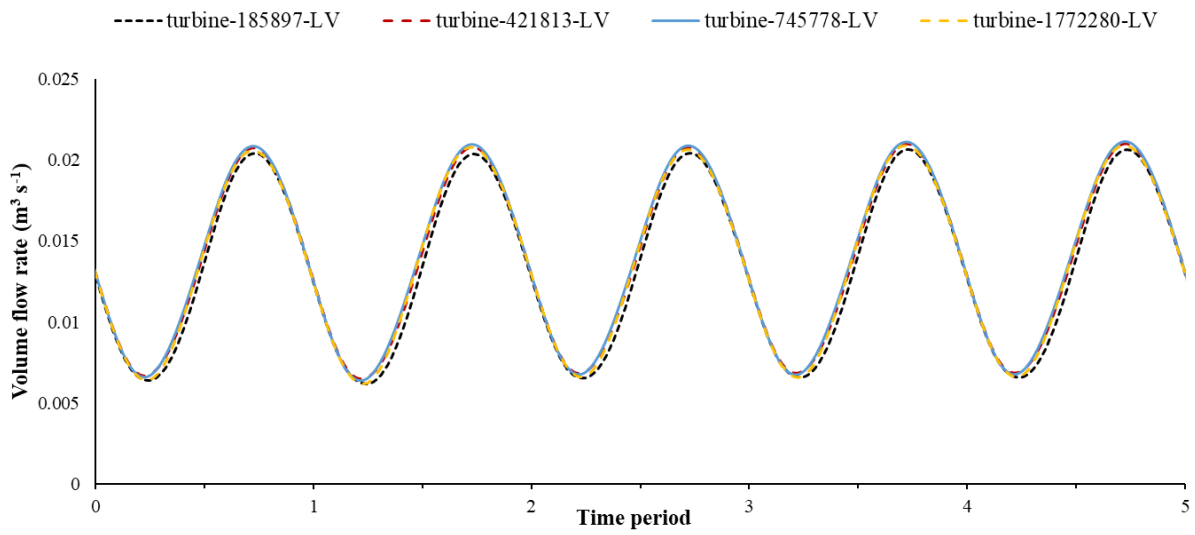

Figure 5-2: Airflow rate results for the left valve (LV) for simulations of four grid sizes of 185897, 421813, 745778, and 1772280.

Error! Reference source not found. displays the airflow rate results for the right valve (RV) for simulations of the chosen grid sizes. The modelling results of the grid with sizes of 745778 and 1772280 are proven to be in good agreement. To ensure that the intended grid size is as accurate as possible, the maximum error of results for each grid size has been determined and reported in **Error! Reference source not found.**. As can be observed, grid #3 has an inaccuracy of 3.51 per cent compared to grid #4 for the airflow rate results for the right valve. Therefore, in terms of computational cost, grid #3 is the superior option.

Table 5-2: Accuracy comparison of each selected grid size compared to the next grid size for the airflow rate results for the right valve (RV).

	Grid #1 compared to grid #2	Grid #2 compared to grid #3	Grid #3 compared to grid #4
Maximum error (%)	13.82	5.02	3.51

Moreover, **Error! Reference source not found.** depicts the wave prob for the right valve (RV) for simulations of the discussed grid sizes. The results of the grid with sizes of 745778 and 1772280 are well matched. To ensure that the selected grid size is as accurate as possible, the maximum error of results for each grid size has been calculated and shown in **Error! Reference source not found.**. As indicated, grid #3 has an error of 0.06 per cent compared to grid #4 for the wave prob for the right valve. Therefore, in terms of computational cost, grid #3 is a desirable choice for the rest of the study.

Table 5-3: Accuracy comparison of each selected grid size compared to the next grid size for the wave prob for the right valve (RV).

	Grid #1 compared to grid #2	Grid #2 compared to grid #3	Grid #3 compared to grid #4
Maximum error (%)	0.15	0.11	0.06

Further, the results of airflow rate inside the turbine for both right and left valves for simulations of the selected grid sizes are shown in **Error! Reference source not found.**. As seen, the results of the grid

with sizes of 745778 and 1772280 are comparatively close. To ensure that the chosen grid size is precise, the maximum error of results for each grid size has been determined and shown in **Error! Reference source not found.**. As shown, grid #3 has an error of 1.04 per cent compared to grid #4 for the airflow rate inside the turbine for both right and left valves. Eventually, by taking into account the computational cost, grid #3 is a better choice for the remaining simulations.

Table 5-4: Accuracy comparison of each selected grid size compared to the next grid size for the airflow rate inside the turbine for both right and left valves.

	Grid #1 compared to grid #2	Grid #2 compared to grid #3	Grid #3 compared to grid #4
Maximum error (%)	5.13	4.32	1.04

Further, **Error! Reference source not found.** demonstrates the results of the pressure inside the chamber for simulations of the selected grid sizes. As per **Error! Reference source not found.**, the results of the grid with sizes of 745778 and 1772280 are in good agreement. The maximum error of results for each grid size has been calculated and summarized in **Error! Reference source not found.**. As shown, grid #3 has an error of 1.04 per cent compared to grid #4 for the pressure inside the chamber. As a result, considering the computational cost, the results of grid #3 is the independent from the grid.

Table 5-5: Accuracy comparison of each selected grid size compared to the next grid size for the pressure inside the chamber.

	Grid #1 compared to grid #2	Grid #2 compared to grid #3	Grid #3 compared to grid #4
Maximum error (%)	7.23	5.65	2.32

As thoroughly presented in **Error! Reference source not found.**, **Error! Reference source not found.**, **Error! Reference source not found.**, **Error! Reference source not found.**, and **Error! Reference source not found.**, according to the obtained results of mesh analysis, grid #3 (i.e., grid with 745778 elements) achieves the maximum errors below 5% in all key performance indicator of the system. Therefore, this grid will be used for the simulations as the grid independence has been achieved for the results.

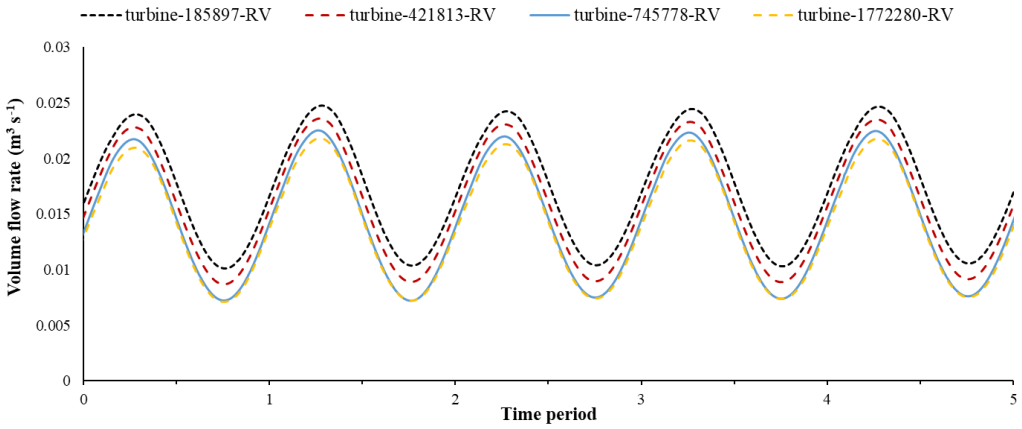

Figure 5-3: Airflow rate results for the right valve (RV) for simulations of four grid sizes of 185897, 421813, 745778, and 1772280.

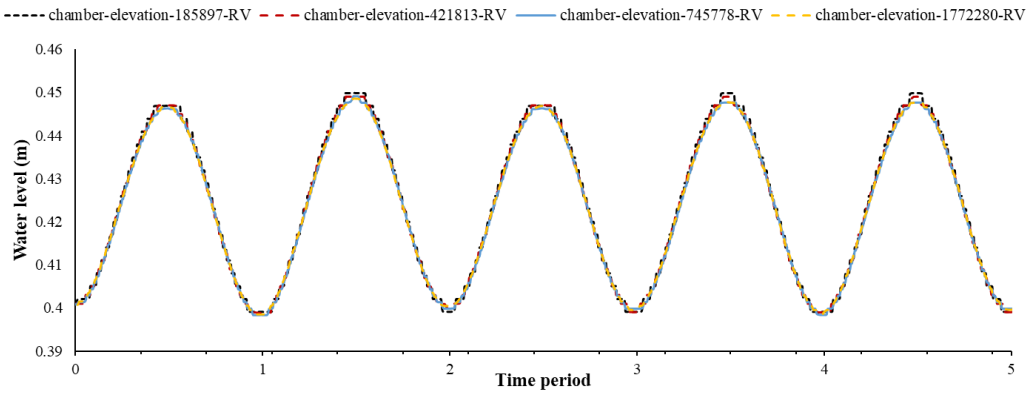

Figure 5-4: Results for the wave prob for the right valve (RV) for simulations of four grid sizes of 185897, 421813, 745778, and 1772280.

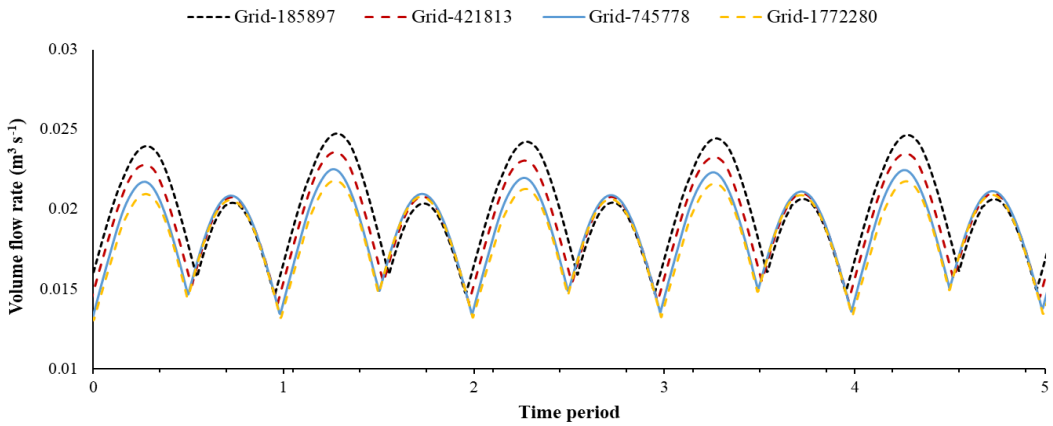

Figure 5-5: Airflow rate inside the turbine for both right and left valves for simulations of four grid sizes of 185897, 421813, 745778, and 1772280.

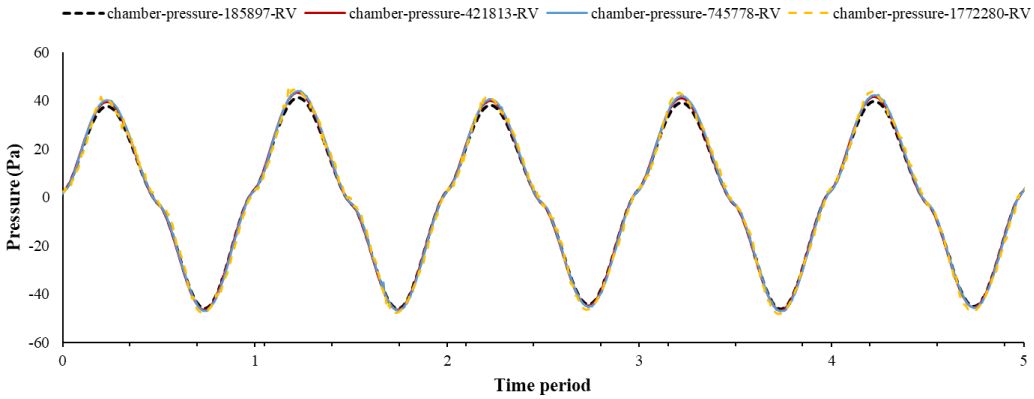

Figure 5-6: Pressure inside the chamber for simulations of four grid sizes of 185897, 421813, 745778, and 1772280.

5-4- Time Step Independence Analysis

In the previous section, grid independence has been achieved. Because this study is transient, the selected time step of the simulation should be analyzed to obtain accurate results. Five time-step settings of 0.0014s, 0.0007s, 0.00056s, 0.00035s, and 0.00028s have been selected, and sensitivity analysis was carried out based on the selected time settings respectively.

Error! Reference source not found. depicts the water elevation inside the chamber for the selected time steps. As seen, the results for time steps of 0.0014s and 0.0007s are devastatingly inaccurate. Furthermore, the water level for time steps of 0.00028s and 0.00035s are in good agreement and fluctuate between 0.39m and 0.45m, approximately. Therefore, the finding of **Error! Reference source**

not found. suggests a time step of 0.00035s as the optimum selection.

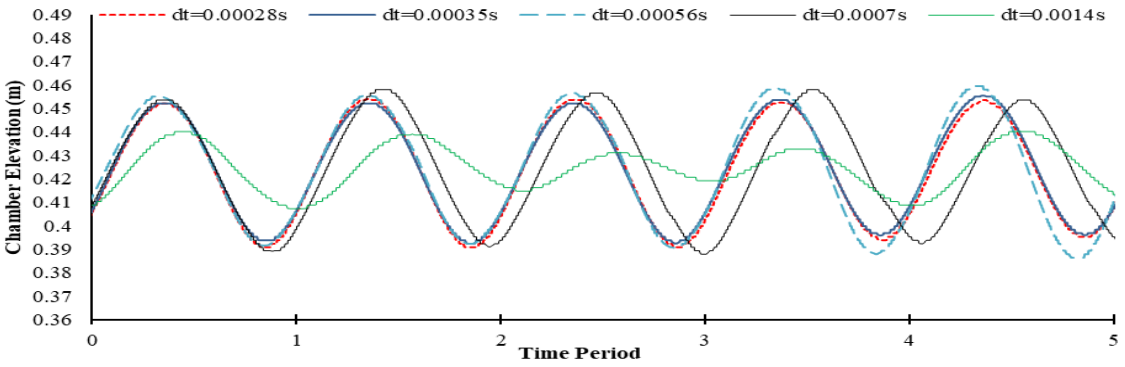

Figure 5-7: Water level inside the chamber for simulations for five time steps of 0.0014s, 0.0007s, 0.00056s, 0.00035s, and 0.00028s.

The pressure inside the chamber for the given time steps is depicted in **Error! Reference source not found.**. The findings for time steps of 0.0014s and 0.0007s are severely inconsistent, as shown. Moreover, the pressure inside the chamber fluctuates between 90Pa and -90Pa for time steps of 0.00028s and 0.00035s and is in good agreement. As a result, similar to the results of water level, **Error! Reference source not found.** implies that a time step of 0.00035s is the best choice.

Error! Reference source not found. depicts the turbine flow rate for the given time steps. As can be seen, the results for time steps of 0.0014s and 0.0007s are quite inconsistent. Furthermore, at time steps of 0.00028s and 0.00035s, the turbine flow rate varies between $0.009 m^3 s^{-1}$ and $0.037 m^3 s^{-1}$, which is in excellent accordance. As a result, **Error! Reference source not found.** demonstrates that a time step of 0.00035s is the optimal choice, similar to the results of water level and pressure inside the chamber.

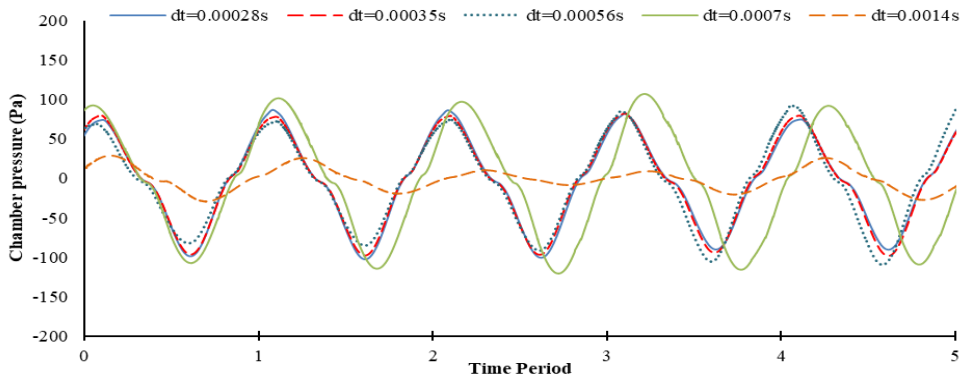

Figure 5-8: Pressure inside the chamber for simulations of five time steps of 0.0014s, 0.0007s, 0.00056s, 0.00035s, and 0.00028s.

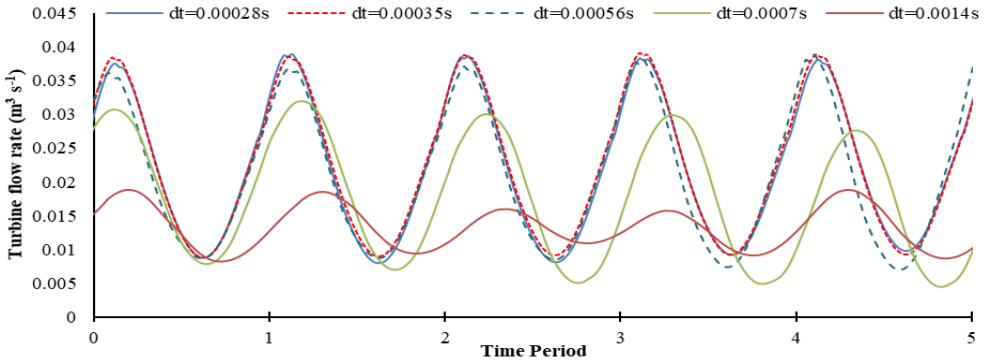

Figure 5-9: Turbine flow rate for simulations of five time steps of 0.0014s, 0.0007s, 0.00056s, 0.00035s, and 0.00028s.

Error! Reference source not found. and **Error! Reference source not found.** are provided to ensure that the results of the simulation with a time step of 0.00035s have an acceptable error. As shown in **Error! Reference source not found.**, the fluctuation of results for water level inside the chamber effectively reduced for time steps of 0.00035s and smaller. Besides, as depicted in **Error! Reference source not found.**, the difference between the results of 0.00035s and 0.00028s time steps is less than 0.5%, so the 0.00035s time step is considered a suitable time step for the simulation.

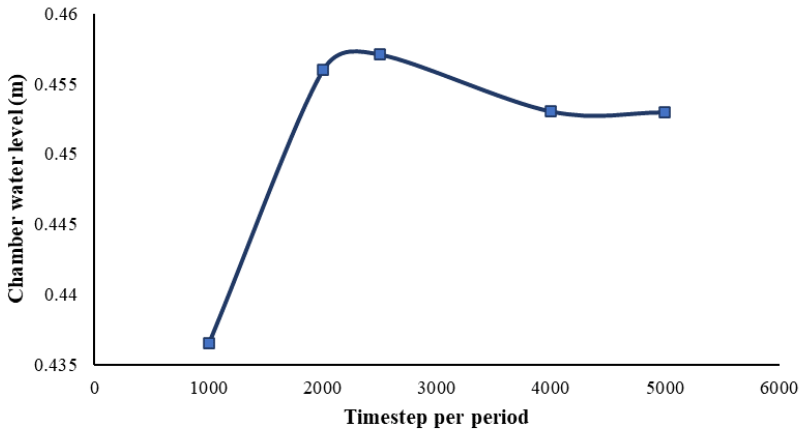

Figure 5-10: The fluctuation of results for water level inside the chamber for different time steps.

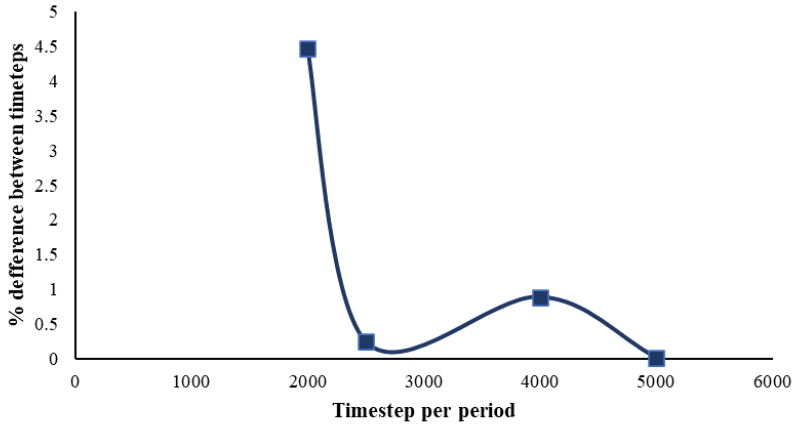

Figure 5-11: The difference between the results of selected time steps.

5-5- Data Validation Results

In this section, the numerical approach used in this study is validated against previous studies. Then, the energy performance of the proposed hybrid wave-wind energy converter is analyzed. The results of the conventional WEC model with experimental [70] and numerical [64] data for wave height H = 40mm, periodicity T = 1.4s, water depth h = 420mm, and orifice width e = 2.5mm, are compared with the proposed study results as presented in **Error! Reference source not found.**. As can be observed, the simulation results of the study correlate well with the experimental and numerical data of previous research [44, 78].

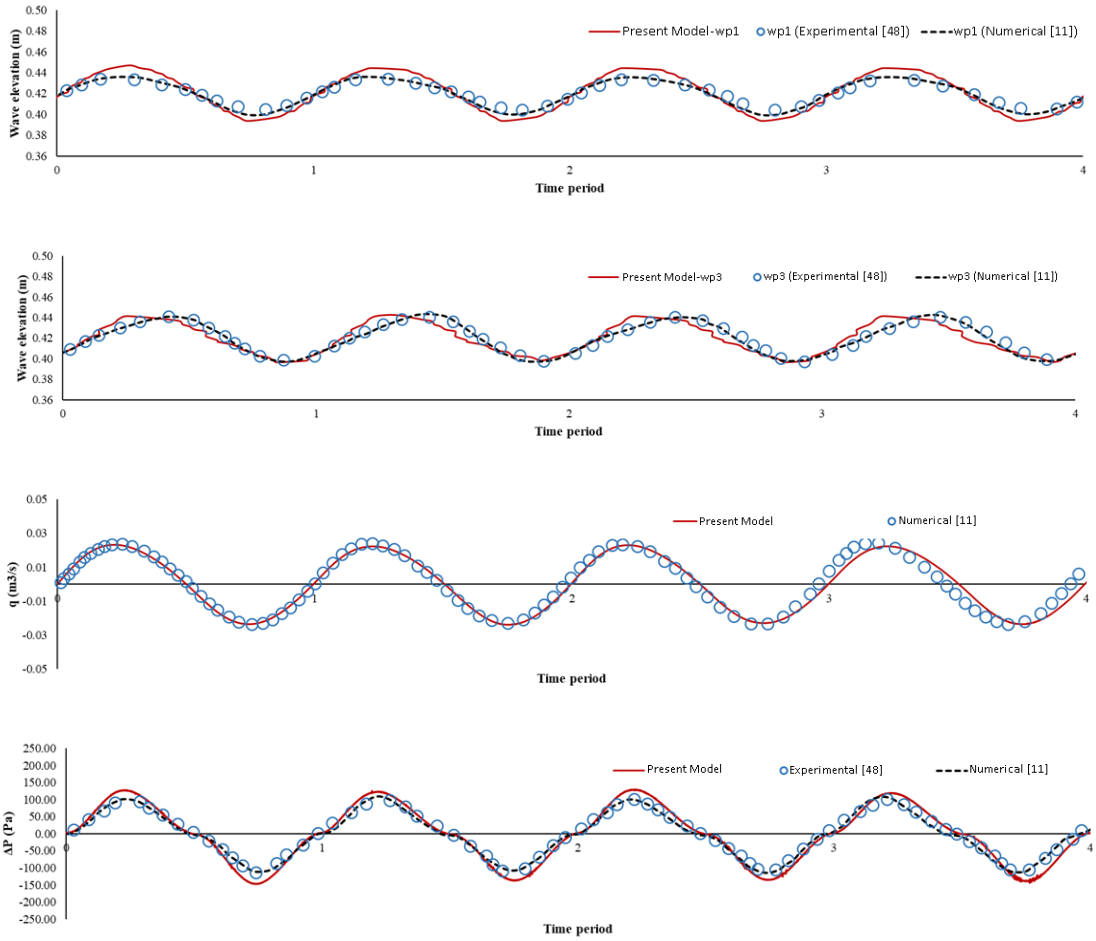

Figure 5-12: Simulation results versus numerical [64] and experimental work [70]: From top to bottom: chamber water height, water level height in wp1 and wp3, flow rate passing through the orifice, and pressure difference of the chamber inside and outside.

5-6- New Hybrid Model Simulation Design

5-6-1- Case Study 1: Wind Speed Impact

A summary of the simulation results related to incorporating the effect of wind into the performance of the new hybrid device and a comparison with the previous studies for OWC is provided. In this study the three wind speeds of 0.7, 0.85 and 1 m/s are applied to the inlet boundary and the performance of the proposed hybrid model is evaluated in each scenario.

5-6-2- Geometry Impact

Table 5-6 shows the details of the Geometrical analysis for the new hybrid model in detail. Turbine height, the width of the orifice and orifice angle changed to three different dimensions to show the effect of changing the main parameters on the output power of the newly proposed mechanism. The outcome of this case study is to show the effect of increasing or decreasing each element to help future work related to this concept and also help readers to have a better understanding of the effect of changing the main effective elements on the device performance.

Table 5-6: Details of the geometry changes used in the analysis.

Geometrical details	**Dimension 1**	**Dimension 2**	**Dimension 3**
Turbine height	0.044 m	0.054 m	0.064 m
Orifice width	0.0025 m	0.0035 m	0.0045 m
Orifice angle (degree)	0	10	20

Chapter: 6 Results and Discussion

6-1- Introduction

The numerical method used to explore the proposed hybrid wave-wind WEC is discussed in the previous chapters, and the model's accuracy is investigated. The numerical results are verified using experimental and numerical data in this chapter. The achievement of the proposed design is then compared to the conventional system in various attributes to offer a more in-depth understanding of the results. Since the conventional WEC designs are not wind-affected, wind flow does not affect their performance. Combining wind energy with WEC, on the other hand, can drastically enhance power generation due to its high energy content. As a result, simulation studies were conducted with several different wind speeds to further analyze the proposed system. The output power, turbine flow rate, orifice, windcatcher flow rate, water level, and pressure within the chamber are all crucial criteria to consider. Moreover, the geometrical parameters of the system have a significant impact on the performance. As a result, to achieve maximum turbine flow, the geometry must be optimized. The chapter also presents the geometric improvements and optimizations of the main design of the hybrid wave-wind wave energy converter introduced in this study, such as orifice output angle, turbine height, windcatcher inlet diameter, the distance between the air inlet and outlet valves, windcatcher inlet height of the turbine, windcatcher width size, and overall windcatcher geometry.

As previously stated, the high level of wind flow in coastal zones motivates the usage of wind energy in conventional WECs. The proposed design's main contribution is the incorporation of wind energy into the system and its combination with wave energy. **Error! Reference source not found.** shows the windcatcher's inlet wind flow rate, the flow rate induced by the movement of the water level within the

chamber, the simulated turbine flow rate, and the maximum turbine flow rate. Since the geometry under consideration is not ideal, there is a mismatch between the simulation result and the maximum turbine flow rate (sum of wind and wave flow). As a result, in order to reach maximum turbine flow rate, the geometry should be improved, and some geometric factors, such as the orifice output angle, need to be adjusted.

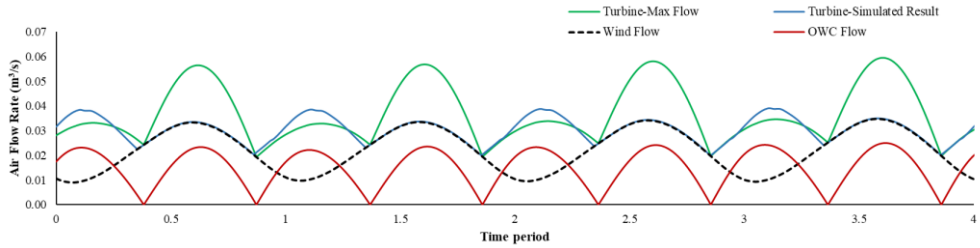

Figure 6-1: The airflow rate generated by wind flow, wave, simulated turbine flow, and maximum turbine flow.

In a conventional OWC, the flow direction on the turbine changes with each period. Therefore, a bidirectional turbine like a Wells turbine is necessary. The proposed new design in this study is intended to avoid airflow direction change. **Error! Reference source not found.** depicts the turbine flow in the conventional OWC system and the hybrid wind-wave energy converter. The integration of wind and wave flow, as indicated, increases net flow through the turbine and the direction of flow through the turbine in both designs. In the hybrid design, the oscillation amplitude of the turbine flow is lowered from an average of $0.047 m^3 s^{-1}$ to $0.02 m^3 s^{-1}$. This reduction enhances power generation homogeneity.

Error! Reference source not found. depicts the water level within the chamber, the pressure difference between the inside and outside of the chamber, the airflow rate through the turbine, and the maximum power production in both conventional and proposed hybrid systems. As wind energy enters the hybrid wind-wave system, the amount of output energy grows. As can be observed, the turbine always has a significant quantity of airflow, suggesting that even when there is no airflow caused by the wave, the wind captured by the windcatcher provides the airflow rate and the system's output power is not zero. Furthermore, this equation is used to compute the maximum output power of typical wind turbines: $P = 0.5 \cdot r \cdot A \cdot V^3$. **Error! Reference source not found.** depicts this feature, which may be concluded that given the unidirectional flow through the turbine, a variety of types of turbines operate better than

Wells turbines can be employed in the proposed design.

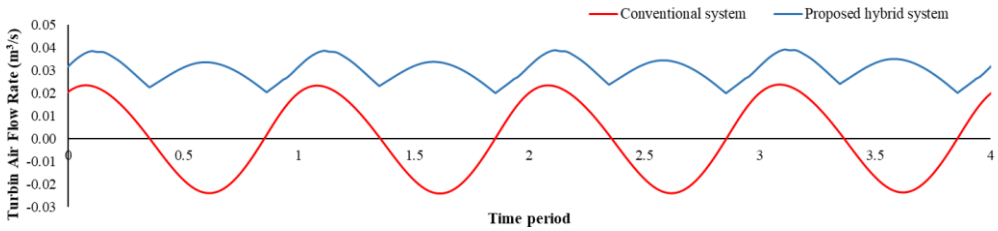

Figure 6-2: The rate of turbine air flow in conventional and proposed hybrid designs.

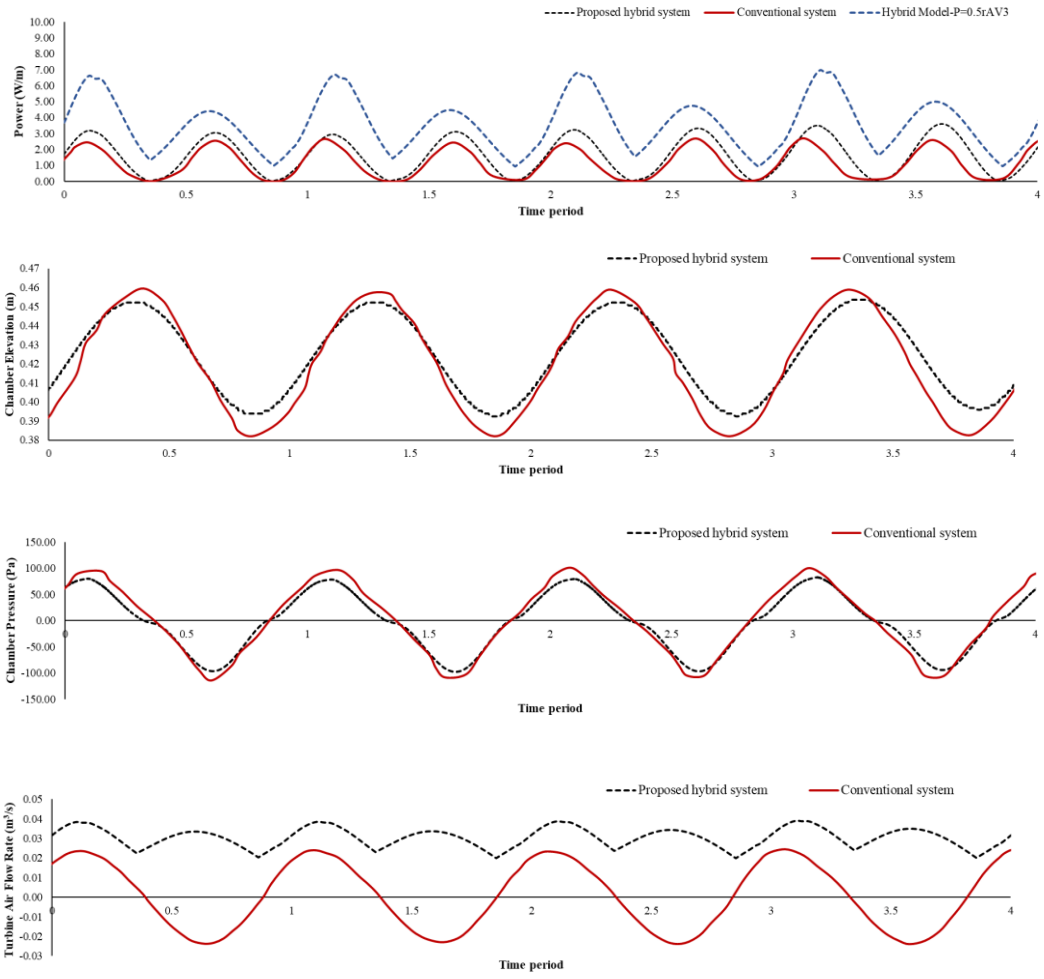

Figure 6-3: Comparison of hybrid model results with the conventional model. Top to down: chamber water level, inside and outside chamber pressure difference, and flow rate through Orifice.

The influence of wind speed on the performance of the proposed system is evaluated at three distinct

wind speeds of 0.7, 0.85, and 1m/s. It is worth noting that the chosen wind speeds are considered based on variable scaling that uses the Froude theory, which is extensively explained by López et al. [70]. The flow rate of air that enters the windcatcher rises as the speed of wind increases. While the airflow rate profile stays unchanged, the average turbine airflow rate increases. Boosting the airflow rate increases the speed of the turbine blades and, as a result, the power output. Therefore, wind speed is an important consideration in this system. It is worth noting that the speed of wind does not affect the airflow delivered by the wave. **Error! Reference source not found.** depicts the impact of modifying the wind speed on the inlet flow to the windcatcher. According to the results, raising the wind speed by 0.85m/s has a more serious impact than raising the wind speed by 0.7m/s. **Error! Reference source not found.** also measures the percentage change in entry flow to the windcatcher caused by changes in the speed of the wind. As presented, increasing the speed from 0.7m/s to 0.85m/s and 0.85m/s to 1m/s leads to an average gain of 12.3% and 26.9% in the inlet flow rate to the windcatcher, respectively, whereas the maximum increase is near 60%.

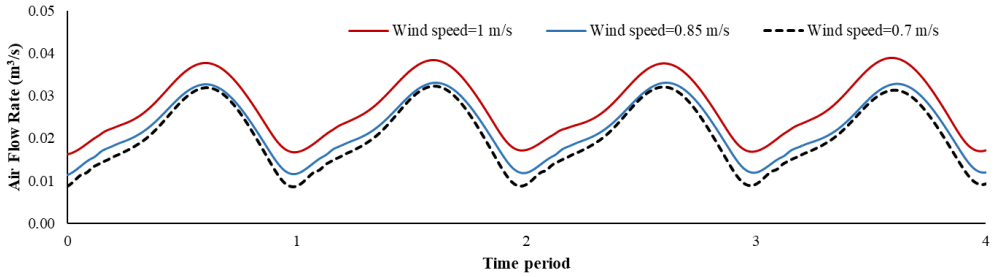

Figure 6-4: The impact of wind speed on the windcatcher's entry flow.

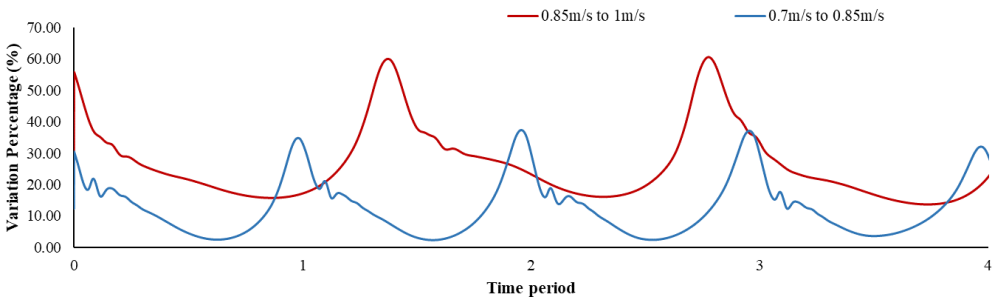

Figure 6-5: Percentage variation in entry flow to the windcatcher caused by changes in wind speed.

Error! Reference source not found. depicts the turbine airflow rate at various wind speeds. As demonstrated, the crossing airflow rate through the turbine would not be zero for the duration of the simulation. The findings show that the turbine's minimum airflow rate is around 50%, 48%, and 45% of its maximum airflow rate for wind speeds of 1 m/s, 0.85 m/s, and 0.7 m/s, respectively. **Error! Reference source not found.** represents the impacts of this constant airflow rate on energy production. The proposed hybrid design, as shown, generates constant power while in operation. Moreover, the wind speed has a major impact on the energy generated, highlighting the importance of integrating a windcatcher into the system. Adapting the orifice angle of the proposed hybrid system leads to more consistent output energy, as shown in the transient results.

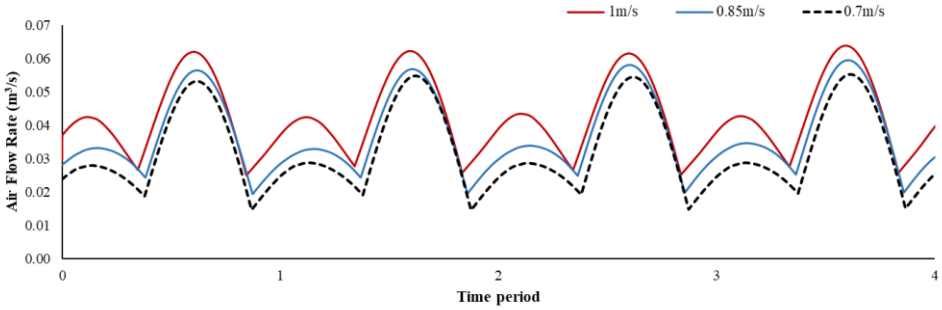

Figure 6-6: Transient results of the turbine flowrate at different wind speeds.

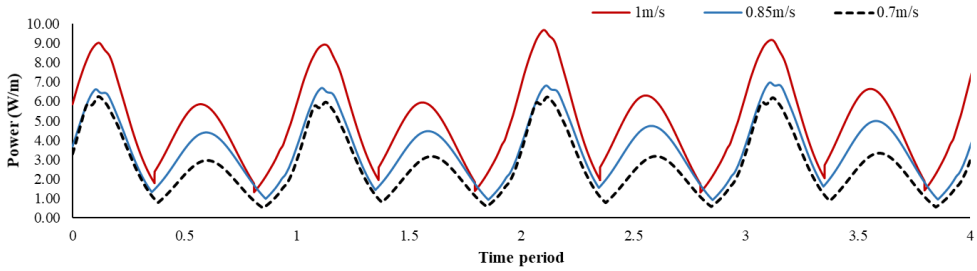

Figure 6-7: Transient results of the output power at different wind speeds.

The wind has no impact on wave output energy production in OWC systems, as previously indicated. To confirm this claim, **Error! Reference source not found.** presents the velocity and fluid fraction contours for two wind speeds of 0.7m/s and 1m/s. As can be observed, the wind has no effect on the height of the water level within the chamber. Therefore, the wind speed variation does not influence the pattern of water velocity or the water elevation in the chamber. Furthermore, the intake and exit airflow

from the chamber stays constant, in contrast to the innovative design proposed in this study, which promotes power generation from wind and wave energies.

Error! Reference source not found. presents the cumulative influence of the velocity distribution generated by the airflow rate of wave motion in the chamber and the windcatcher's airflow rate. Several flow properties arise as a result of this, including a powerful vortex at the lower lip and minor vortices at the top lip and entrance into the chamber. These vortices are generated by an abrupt change in geometries and the interaction of two independent airflows, which separate the flow and progressively release energy from the vortex's centre. Fig. 6-9 shows a transient simulation that verifies that vortex formation reduces with time; nevertheless, vortex formation should be decreased through geometrical improvement.

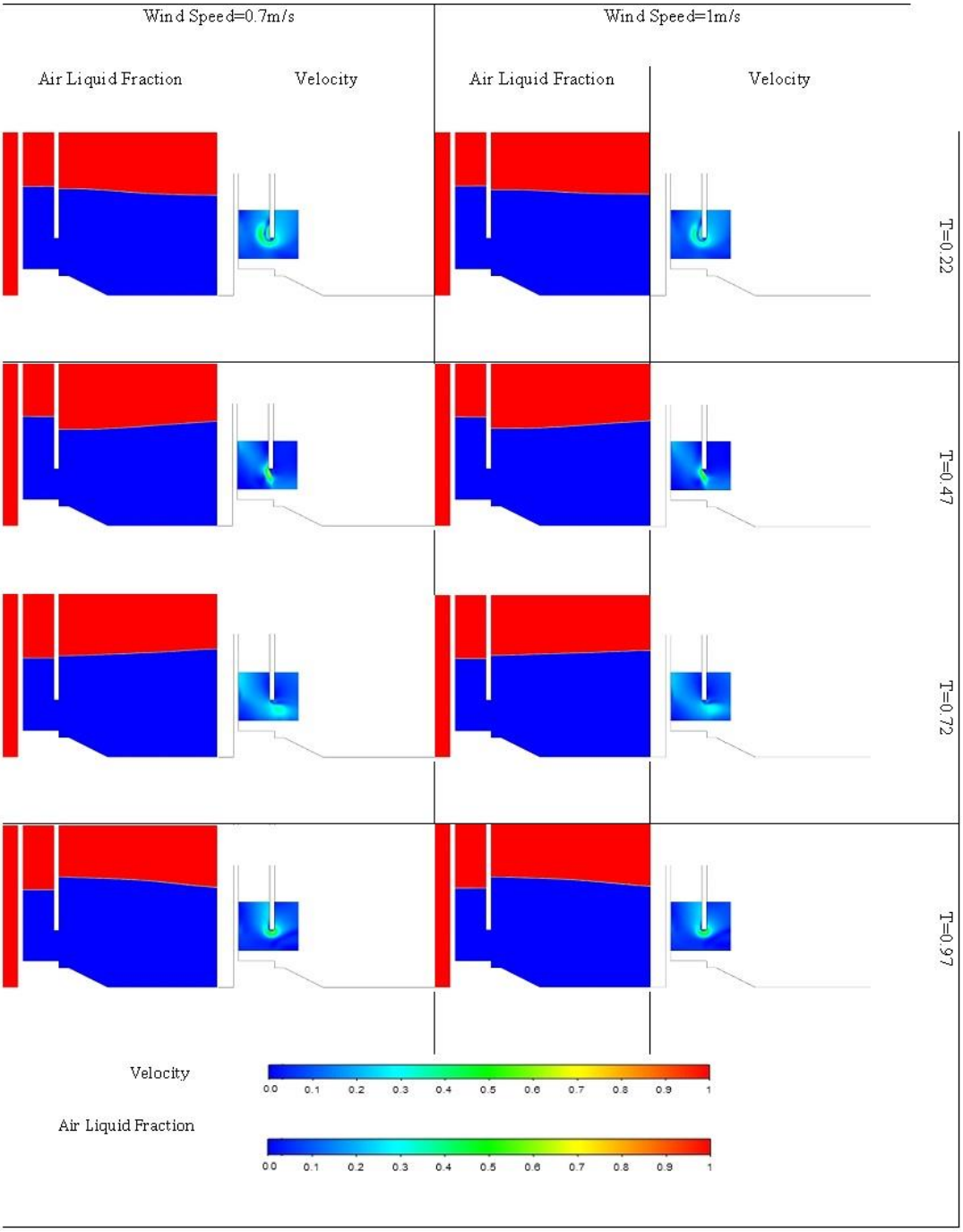

Figure 6-8: Transient results of the turbine flowrate at different wind speeds.

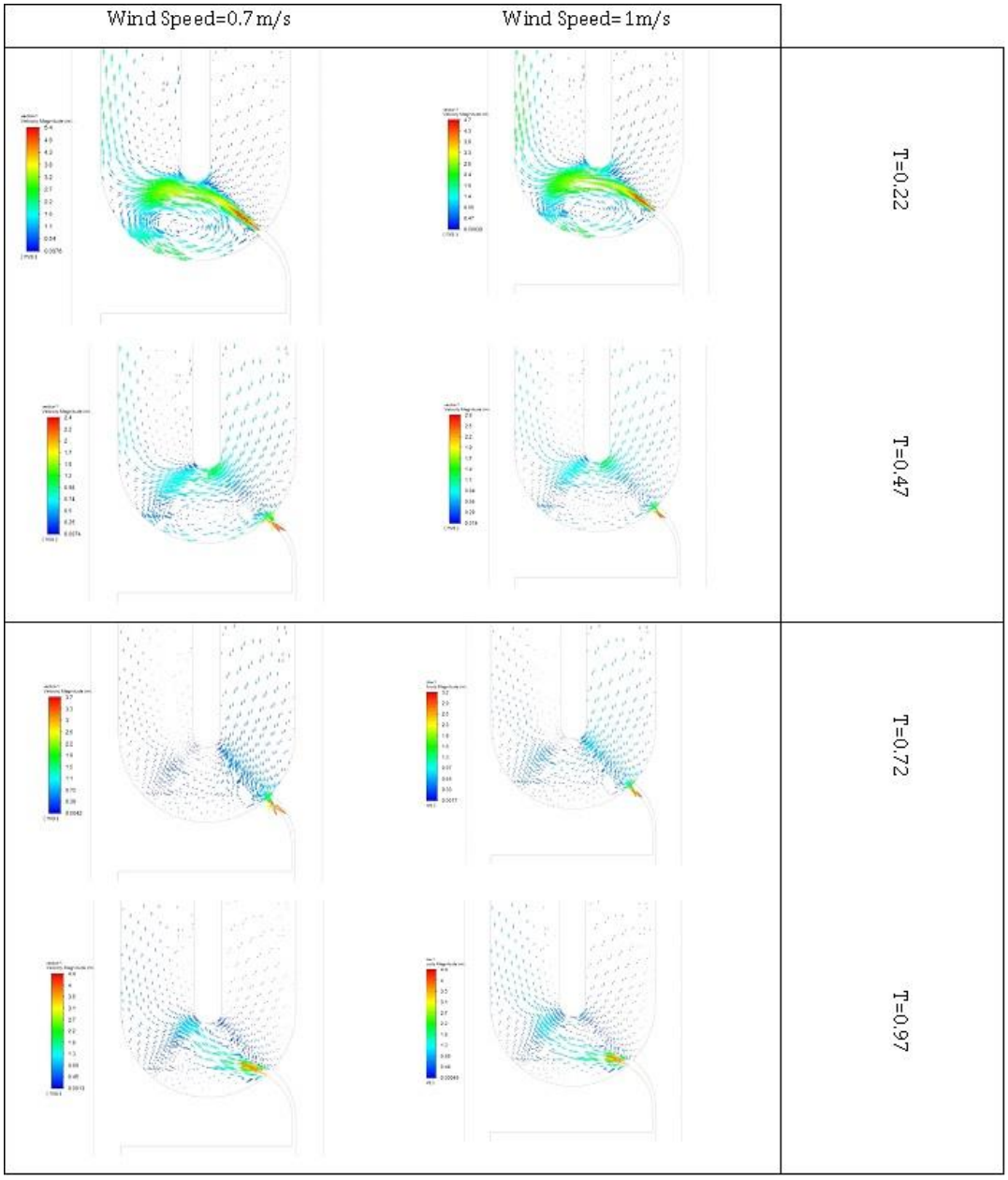

Figure 6-9: Transient results of the turbine flowrate at different wind speeds.

6-2- Geometry Modification Results

In this section, the effect of key geometrical parameters namely turbine height, orifice width, and orifice output angle on the performance of the proposed hybrid system (i.e., orifice flow rate, chamber pressure, turbine flow rate, and power) are examined and discussed.

6-2-1- Effect of turbine aperture height (turbine height)

The flow rate to the windcatcher is affected by the height of the turbine aperture (turbine height). The

simulations confirmed the effect of turbine height on wind energy production in the combined wave-wind system. The wind and wave energies are harvested separately in the proposed hybrid system. As a result, changing the height of the turbine, as seen in previous sections, does not affect the hybrid system's performance in harvesting wave energy and only changes the energy harvested by the wind. **Error! Reference source not found.** and **Error! Reference source not found.** show the orifice flow rate and the pressure inside the chamber, respectively, to demonstrate this claim. As can be seen, changing the height of the turbine does not affect the airflow rate passing through the orifice or the pressure inside the chamber, and the values remained constant at different heights. This shows that changing the structure of the outer part of the chamber to improve the harvested energy by the windcatcher has no negative impact on the energy produced by the wave.

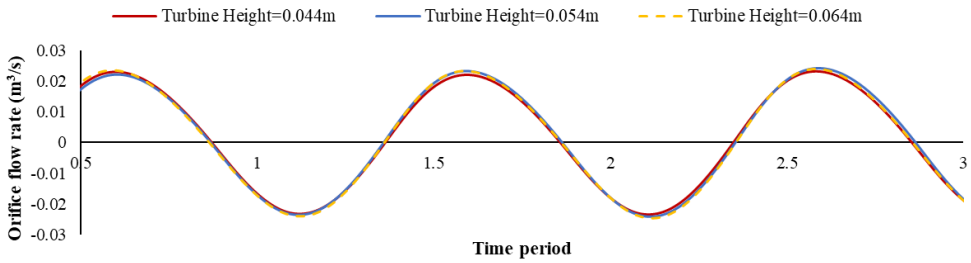

Figure 6-10: Air flow rate passing the orifice for different turbine heights.

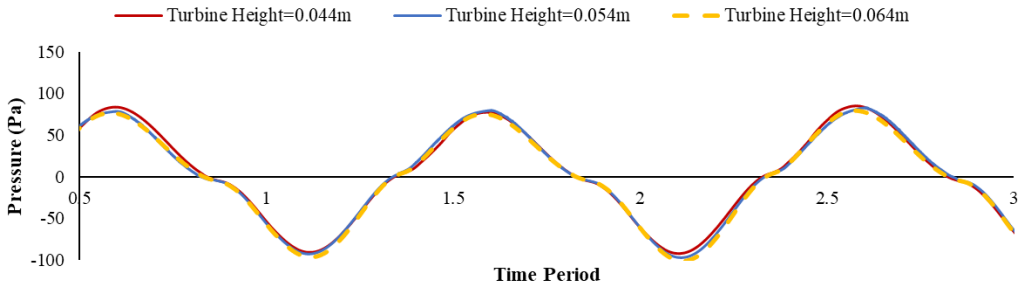

Figure 6-11: Pressure in the OWC chamber for different turbine heights.

Error! Reference source not found. depicts the airflow rate through the turbine at various turbine heights. The turbine airflow rate has decreased as the turbine height has increased. The maximum value of turbine airflow rate for a turbine height of 0.054m is approximately 0.039m^3/s, which is 11.4% higher than the turbine height of 0.044m with a value of 0.035m^3/s. Furthermore, the system with a turbine

height of 0.054m provides a 25.8% more airflow rate when compared to the system with a turbine height of 0.064m, which achieves a maximum flow rate of 0.031m^3/s. Furthermore, **Error! Reference source not found.** illustrates the output power of the turbine for different elevations. A height of 0.064m leads to a decrease in output power compared to a height of 0.054m, while the turbine height of 0.044m results in a minor change in power generation. However, the difference in output power when the chamber is filling, and discharging is visible in the case of 0.044m height as shown in **Error! Reference source not found.**. When the air inside the chamber passes through the right valve (which discharges the chamber), the orifice output is not at the desired angle, blocking some of the orifice output flow from passing through the turbine. This issue prevents the airflow rate produced by the windcatcher from properly mixing with the airflow rate provided by the wave. Eventually, the effect of turbine height on the performance of the proposed system revealed that for different turbine heights, other geometric parameters need to be modified as well. The maximum value of power generation for a turbine height of 0.054m is around 3.2W/m, which is 6.7% higher than the power generation by turbine height of 0.044m with a value of 3W/m. However, as shown in **Error! Reference source not found.**, the transient simulation revealed that the system with a turbine height of 0.044m does not reach its maximum power generation at every period. Moreover, the system with a turbine height of 0.054m produces 45.4% more power when compared to the system with a turbine height of 0.064m, which achieves a maximum power generation of 2.2W/m.

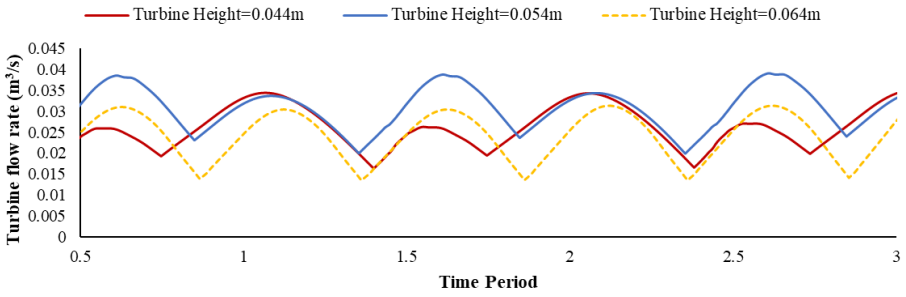

Figure 6-12: Turbine air flow rate for different turbine heights.

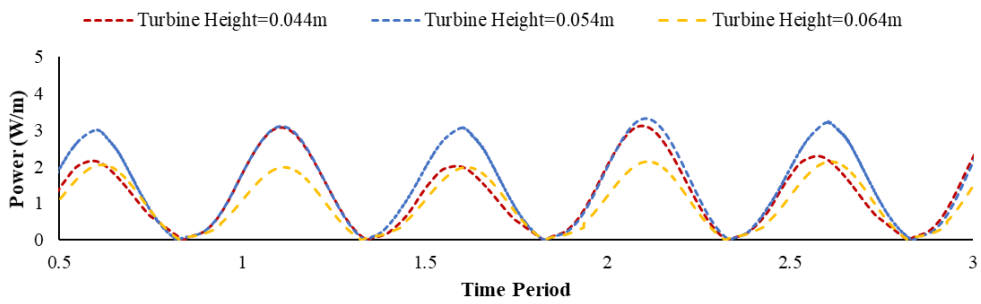

Figure 6-13: Output power generation for different turbine heights.

6-2-2- Effect of orifice size (width)

Based on a prior experimental investigation conducted by Ning et al. [116], the impact of orifice width on hydrodynamic performance is substantial because it has a large effect on the free surface height and pressure of the air inside the chamber. Therefore, in this section, the key performance indicators of the proposed hybrid system have been analyzed for three different orifice widths of 0.0025, 0.0035, and 0.0045m respectively.

Error! Reference source not found. shows the air pressure inside the chamber for the chosen orifice widths. As seen, chamber pressure increases for smaller orifice width. The reasoning behind this is that as the volume of air rises, the air pressure exerted on the water column decreases. As a result, the addition of more air within the chamber serves as a softer spring, extending the water column's natural oscillation duration. As presented in **Error! Reference source not found.**, the maximum chamber pressure for an orifice width of 0.0025m is around 80Pa, which is 45.5% and 89.6% higher than the air pressure inside the chamber for orifice widths of 0.0035m and 0.0045m, respectively.

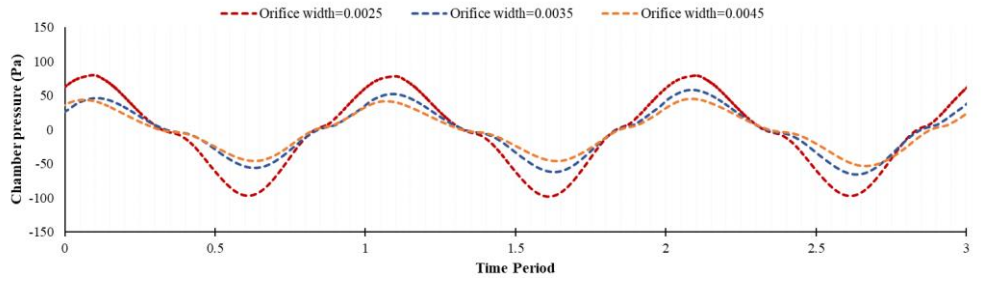

Figure 6-14: Chamber pressure for different orifice widths.

The orifice airflow rate for the selected orifice widths is presented in **Error! Reference source not found.**. As shown, the orifice airflow rate increases for larger orifice widths. The maximum airflow rate for an orifice width of 0.0045m is about 0.031m^3/h, which is 24% and 47.6% higher than the flow rate for orifice widths of 0.0035m and 0.0025m, respectively. Moreover, because the airflow rate is proportional to the vertical velocity of the free surface which may be estimated as the rate of variation in free surface elevation over time, it's been anticipated that the airflow rate would reflect variations in surface elevation within the chamber. To thoroughly demonstrate this, the results of variation in chamber elevation are presented in **Error! Reference source not found.**. As depicted, the chamber elevation increases for larger orifice widths. The maximum elevation of the free surface for orifice width of 0.0045m is about 0.47m, and the minimum is 0.38 m; therefore, the difference between the maximum and minimum elevation of the free surface is 0.09m. This value is 28.6% and 80% higher than the difference between the maximum and minimum elevation of free surface for orifice widths of 0.0035m and 0.0025m, respectively.

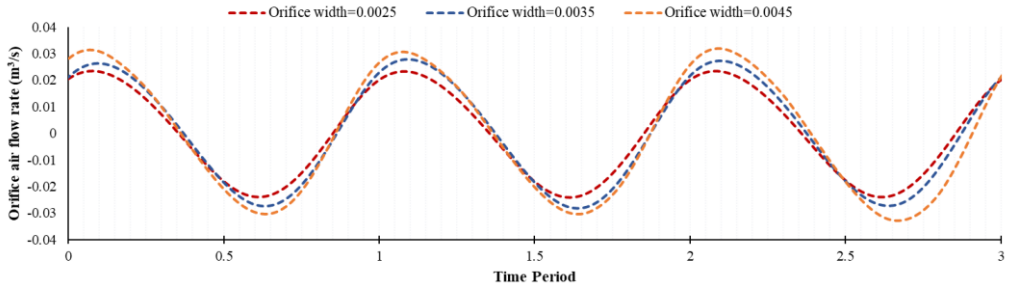

Figure 6-15: Orifice airflow rate for different orifice widths.

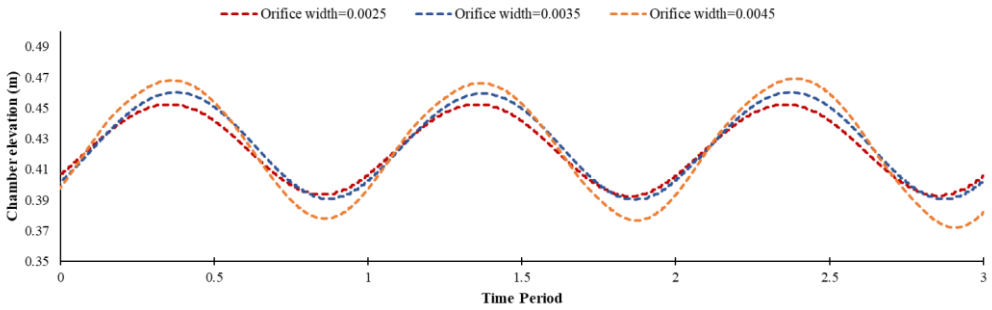

Figure 6-16: Chamber elevation for different orifice widths.

One of the most important factors in comprehensively monitoring the performance of the proposed hybrid system is the amount of power generation of the system. To this aim, the power generation of

the system for different orifice widths is compared and plotted in **Error! Reference source not found.**. As shown, the system with an orifice width of 0.0025m achieves the highest value of power generation when compared to systems with orifice widths of 0.0035m and 0.0045m. The maximum value of power generation for an orifice width of 0.0025m is approximately 3.2W/m, which is 45.4% higher than the orifice width of 0.0035m with a value of 2.2W/m. Furthermore, the system with an orifice width of 0.0025m produces 77.8% more energy when compared to the system with an orifice width of 0.0045m, which achieves a maximum power generation of 1.8W/m.

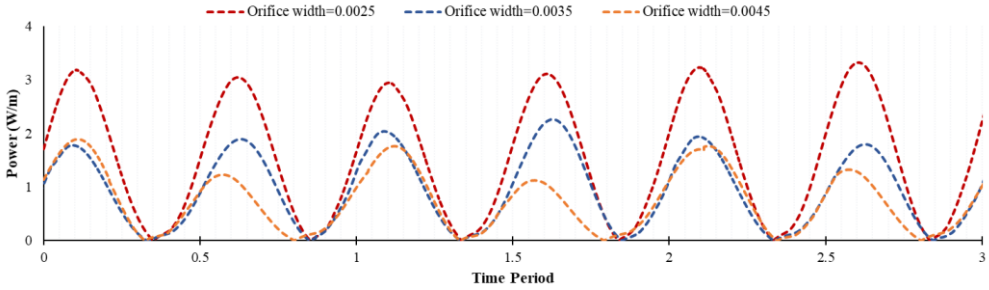

Figure 6-17: Power generation for different orifice widths.

6-2-3- Effect of orifice output angle

The results of the turbine height study revealed that the orifice output angle influences the proposed design's performance. Besides, the results of the turbine height of 0.044m demonstrated that the orifice's output angle relative to the horizon line creates unfavourable conditions for the flow to pass through the turbine. The effect of the orifice angle on the turbine height of 0.044m is investigated in this section by changing this angle.

To investigate the effect of turbine angle on system performance, the system is simulated with three orifice output angles of 0°, 10°, and 20°. **Error! Reference source not found.** shows the 20° orifice output angle compared to the orifice output angle of 0°. This approach is chosen based on the results of the previous section. Because at the initial orifice angle, the output flow from the orifice does not pass completely through the turbine. Therefore, the system performance at an orifice angle of 0° is compared to orifice angles of 10° and 20° respectively.

As previously concluded, changing the geometric parameters of the windcatcher does not affect the

system's performance in harvesting energy from the wave. **Error! Reference source not found.** also demonstrates that changing the orifice angle does not affect the flow rate through the orifice and, as a result, the energy harvested from the wave. The same behaviour is seen in **Error! Reference source not found.** for the pressure inside the chamber because the change of orifice angle does not show a significant effect on the pressure inside the chamber.

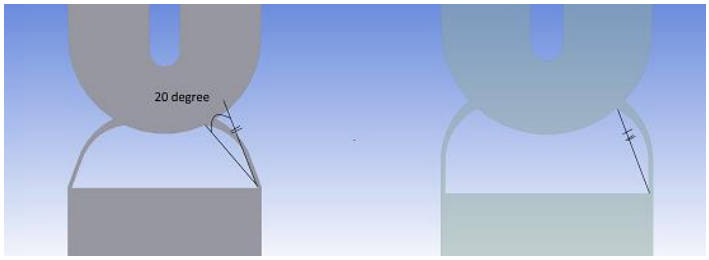

Figure 6-18: The boundaries for the orifice angle to conduct the analysis.

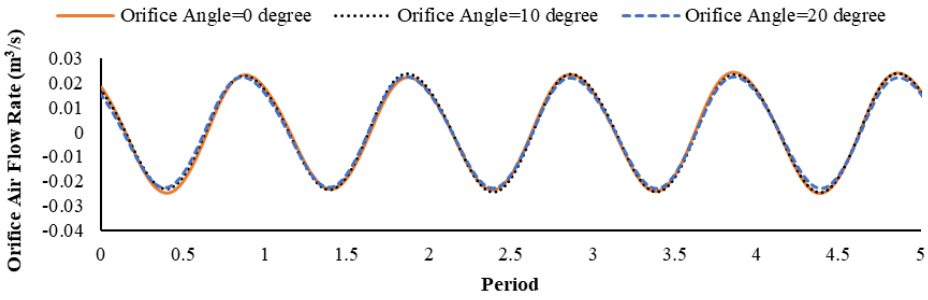

Figure 6-19: Orifice air flow rate for different orifice angles.

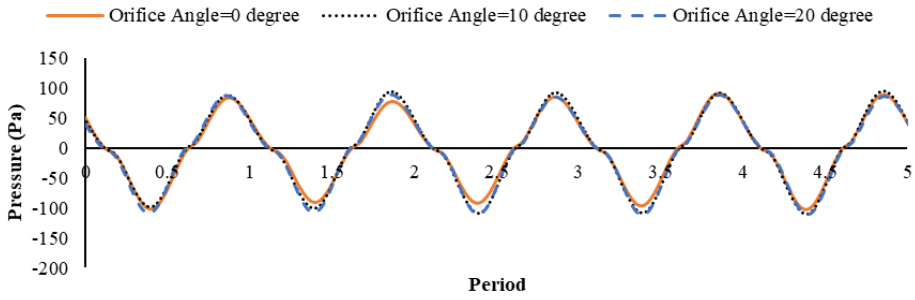

Figure 6-20: Pressure inside the chamber for different orifice angles.

According to the findings of the turbine height study, an improper orifice output angle reduces system performance in harvesting wind energy. Therefore, it is necessary to consider the appropriate orifice output angle according to the turbine height. The flow rate through the turbine is depicted in Figure 4

at two different angles. Modifying the orifice output angle has two effects on the flow rate through the turbine, as shown in **Error! Reference source not found.**. On one hand, it increases the flow rate passing through the turbine because modifying the orifice angle causes all the output airflow rate from the chamber to pass through the turbine. On the other hand, it causes the turbine flow to be equal in both the chamber's filling and discharging states. The consistency of the turbine air flowrate in these two states causes the turbine rotation to be more uniform, which improves the performance of converting mechanical energy to electrical energy. It can be seen in **Error! Reference source not found.** that increasing the orifice output angle increases the peak of output power in both the filling and discharging phases.

Error! Reference source not found. depicts that the maximum value of turbine airflow rate for an orifice angle of 10^0 and 20^0 are 0.039 and 0.045m^3/s, respectively, which are 11.4% and 28.6% higher than the orifice angle of 0° with a value of 0.035m^3/s. Besides, orifice angle of 20^0 produces a more uniform air flow rate. Moreover, **Error! Reference source not found.** depicts that the maximum value of power generation for orifice angles of 10^0 and 20^0 is 4.5 and 4.9W/m, respectively, which are 25% and 36.1% higher than the orifice angle of 0° with a value of 3.6W/m.

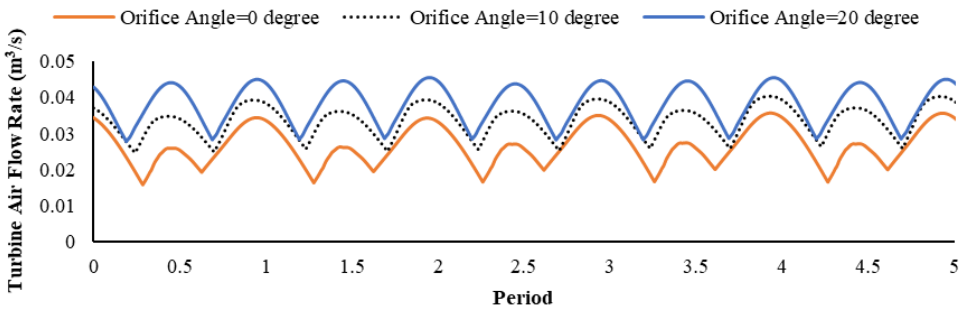

Figure 6-21: Turbine airflow rate for different orifice angles.

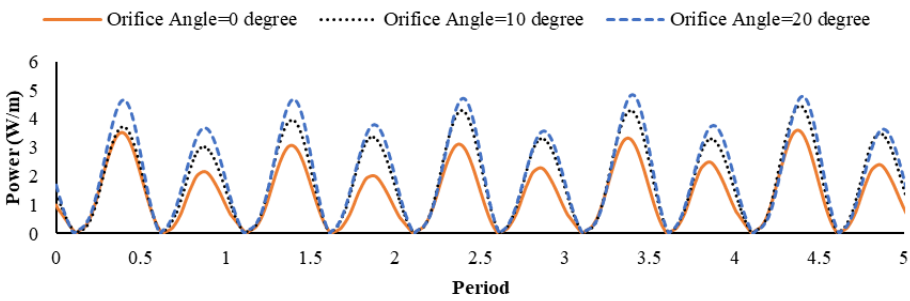

Figure 6-22: Power generation for different orifice angles.

Chapter: 7 Conclusions and Future Work Recommendations

7-1- Conclusions

In this thesis, a novel mechanism and converter were introduced based on incorporating a windcatcher structure to increase the airflow rate through turbine blades. Moreover, two separate valves are designed to ensure that the airflow rate from the chamber of the OWC always flows in one direction. The CFD approach is based on the RANS technique used to simulate the new device characteristics and outcomes. In the first stage, the results for water level elevation, airflow rate passing through the orifice, differential air pressure and output power are validated against previous numerical and experimental models and then a new model is introduced and the outcome is compared with the conventional OWC.

The main contribution of the current research is to introduce a new hybrid model with the ability to use both winds and waves simultaneously which resulted in more airflow rate passing through the turbine blades. Another novelty of this research is creating a bidirectional airflow instead of a unidirectional flow, which enables the use of turbines with higher efficiency and continuous output power. It is found that the turbine in the new hybrid model has always a considerable amount of airflow passing the turbine highlighting the significant contribution of the new design including the windcatcher. In the proposed hybrid system, the oscillation amplitude of the turbine airflow rate is diminished from an average of 0.047 $m^3 s^{-1}$ to 0.02 $m^3 s^{-1}$. This reduction realizes power generation consistency.

Because the given airflow rate by the windcatcher, and consequently the produced power, is heavily influenced by wind speed, the effect of wind speed on the performance of the proposed hybrid model is evaluated at three distinct wind speeds of 0.7, 0.85, and 1 m/s. According to the results, boosting the wind speed by 0.85 m/s caused a more serious impact than raising it by 0.7 m/s. Furthermore, increasing the wind speed from 0.7 m/s to 0.85 m/s and 0.85 m/s to 1 m/s led to an improvement in the intake flow rate to the windcatcher of 12.3% and 26.9%, correspondingly. While the highest possible increase is

roughly 60%.

7-2- Future Work Recommendations

In this research, a novel OWC WEC incorporated with a windcatcher structure was introduced and the current potential of having a hybrid converter has been studied. In addition to adding a windcatcher on top of an OWC, two separate valves are introduced to control the airflow and ensure that the airflow always flows in one direction. To have a complete comprehension of the subject, the preceding elements are recommended for future studies:

1) Geometric adjustments and optimizations of the basic configuration of the hybrid wave-wind wave energy converter presented in this study, such as inlet of the windcatcher, length in between inlet and outlet valves, windcatcher inlet height of the turbine, windcatcher width size, and overall windcatcher geometry.

2) Investigate the wave properties and wind speed patterns and test the new hybrid model under real wave conditions and harsh conditions.

3) Study the impact of air compressibility and scalability on system durability during storm situations. Whereas the findings of this research did not demonstrate a clear indication of scaling impact with incompressible air, scaling impacts from viscous forces and other physical conditions could be expected.

4) Different types of turbines can be assessed based on the new model and considering the advantage of the new hybrid model in having unidirectional airflow.

5) A stationary wave-pulse magnitude should be coupled for every frequency element in a nonlinear-domain method, which brings several complexities to the methodology; while in CFD approaches, correctly resolving a wide variety of frequency elements over a field suitable for lengthy waves increases the computational cost significantly. Therefore, future studies should focus on this issue.

6) Conducting a multi-layer assessment technique in which rapid potential flow calculations are utilized to arrange the reaction and prioritize particular situations for further investigation

using far more costly CFD computations. It will be remarkable to see if a fully nonlinear potential flow regime with a compressible air-flow approach can similarly capture these characteristics.

References

[1] D. Qiao, R. Haider, J. Yan, D. Ning, and B. Li, "Review of Wave Energy Converter and Design of Mooring System," *Sustainability,* vol. 12, no. 19, p. 8251, 2020.

[2] G. Boyle, *Renewable energy: power for a sustainable future*. Oxford University Press, 1996.

[3] E. Rusu and F. Onea, "A review of the technologies for wave energy extraction," *Clean Energy,* vol. 2, no. 1, pp. 10-19, 2018.

[4] IRENA. "Wave Energy Technology Brief." www.irena.org (accessed 19 June, 2021).

[5] K. Gunn and C. Stock-Williams, "Quantifying the global wave power resource," *Renewable Energy,* vol. 44, pp. 296-304, 2012.

[6] A. Clément *et al.*, "Wave energy in Europe: current status and perspectives," *Renewable and sustainable energy reviews,* vol. 6, no. 5, pp. 405-431, 2002.

[7] M. T. Morris-Thomas, R. J. Irvin, and K. P. Thiagarajan, "An investigation into the hydrodynamic efficiency of an oscillating water column," 2007.

[8] E. M. E. C. (EMEC). "Wave Devices." http://www.emec.org.uk/marine-energy/wave-devices/ (accessed June, 2021).

[9] R. Henderson, "Design, simulation, and testing of a novel hydraulic power take-off system for the Pelamis wave energy converter," *Renewable Energy,* vol. 31, no. 2, pp. 271-283, 2006/02/01/ 2006, doi: https://doi.org/10.1016/j.renene.2005.08.021.

[10] "Pelamis, World's First Commercial Wave Energy Project, Agucadoura." https://www.power-technology.com/projects/pelamis/ (accessed.

[11] C. C. Mei. "Hydrodynamic principles of wave power extraction." https://royalsocietypublishing.org/doi/abs/10.1098/rsta.2011.0178 (accessed.

[12] M. Holland, "Oyster 800 at EMEC," 2012. [Online]. Available: https://tethys.pnnl.gov/project-sites/oyster-800-emec.

[13] A. A. Moccia J, Williams D, Phillips J., "Wind in our Sails – The coming of Europe's offshore wind energy industry: a report by the European Wind Energy Association," 2011. [Online]. Available: http://www.ewea.org/fileadmin/files/library/publications/reports/Offshore_Report.pdf.

[14] F. Z. Joyce Lee. "Global Offshore Wind Report 2021." Global World Energy Council. https://gwec.net/global-offshore-wind-report-2021/ (accessed.

[15] A. Colmenar-Santos, J. Perera-Perez, D. Borge-Diez, and C. dePalacio-Rodríguez, "Offshore wind energy: A review of the current status, challenges and future development in Spain," *Renewable and Sustainable Energy Reviews,* vol. 64, pp. 1-18, 2016/10/01/ 2016, doi: https://doi.org/10.1016/j.rser.2016.05.087.

[16] A. Babarit, J.-C. Gilloteaux, G. Clodic, M. Duchet, A. Simoneau, and M. F. Platzer, "Techno-economic feasibility of fleets of far offshore hydrogen-producing wind energy converters," *International Journal of Hydrogen Energy,* vol. 43, no. 15, pp. 7266-7289, 2018/04/12/ 2018, doi: https://doi.org/10.1016/j.ijhydene.2018.02.144.

[17] B. A. Franco, P. Baptista, R. C. Neto, and S. Ganilha, "Assessment of offloading pathways for wind-powered offshore hydrogen production: Energy and economic analysis," *Applied Energy,* vol. 286, p. 116553, 2021/03/15/ 2021, doi: https://doi.org/10.1016/j.apenergy.2021.116553.

[18] A. Pliego Marugán, F. P. García Márquez, and J. M. Pinar Pérez, "A techno-economic model for avoiding conflicts of interest between owners of offshore wind farms and maintenance suppliers," *Renewable and Sustainable Energy Reviews,* vol. 168, p. 112753, 2022/10/01/ 2022, doi: https://doi.org/10.1016/j.rser.2022.112753.

[19] K. Connolly, "The regional economic impacts of offshore wind energy developments in Scotland," *Renewable Energy,* vol. 160, pp. 148-159, 2020/11/01/ 2020, doi: https://doi.org/10.1016/j.renene.2020.06.065.

[20] T. R. Lucas, A. F. Ferreira, R. B. Santos Pereira, and M. Alves, "Hydrogen production from the WindFloat Atlantic offshore wind farm: A techno-economic analysis," *Applied Energy,* vol. 310, p. 118481, 2022/03/15/ 2022, doi: https://doi.org/10.1016/j.apenergy.2021.118481.

[21] H. Acaroğlu and F. P. García Márquez, "High voltage direct current systems through submarine cables for offshore wind farms: A life-cycle cost analysis with voltage source converters for bulk power transmission," *Energy,* vol. 249, p. 123713, 2022/06/15/ 2022, doi: https://doi.org/10.1016/j.energy.2022.123713.

[22] F. Teixeira-Duarte, D. Clemente, G. Giannini, P. Rosa-Santos, and F. Taveira-Pinto, "Review on layout optimization strategies of offshore parks for wave energy converters," *Renewable and*

Sustainable Energy Reviews, vol. 163, p. 112513, 2022/07/01/ 2022, doi: https://doi.org/10.1016/j.rser.2022.112513.
[23] M. Neshat *et al.*, "Layout optimisation of offshore wave energy converters using a novel multi-swarm cooperative algorithm with backtracking strategy: A case study from coasts of Australia," *Energy,* vol. 239, p. 122463, 2022/01/15/ 2022, doi: https://doi.org/10.1016/j.energy.2021.122463.
[24] M. Majidi Nezhad, M. Neshat, G. Piras, and D. Astiaso Garcia, "Sites exploring prioritisation of offshore wind energy potential and mapping for wind farms installation: Iranian islands case studies," *Renewable and Sustainable Energy Reviews,* vol. 168, p. 112791, 2022/10/01/ 2022, doi: https://doi.org/10.1016/j.rser.2022.112791.
[25] E. Gubesch, N. Abdussamie, I. Penesis, and C. Chin, "Effects of mooring configurations on the hydrodynamic performance of a floating offshore oscillating water column wave energy converter," *Renewable and Sustainable Energy Reviews,* vol. 166, p. 112643, 2022/09/01/ 2022, doi: https://doi.org/10.1016/j.rser.2022.112643.
[26] B. Johnston, A. Foley, J. Doran, and T. Littler, "Levelised cost of energy, A challenge for offshore wind," *Renewable Energy,* vol. 160, pp. 876-885, 2020/11/01/ 2020, doi: https://doi.org/10.1016/j.renene.2020.06.030.
[27] M. Bilgili, A. Yasar, and E. Simsek, "Offshore wind power development in Europe and its comparison with onshore counterpart," *Renewable and Sustainable Energy Reviews,* vol. 15, no. 2, pp. 905-915, 2011/02/01/ 2011, doi: https://doi.org/10.1016/j.rser.2010.11.006.
[28] J.-M. Gallardo-Calles, A. Colmenar-Santos, J. Ontañon-Ruiz, and M. Castro-Gil, "Wind control centres: State of the art," *Renewable Energy,* vol. 51, pp. 93-100, 2013/03/01/ 2013, doi: https://doi.org/10.1016/j.renene.2012.09.012.
[29] S. Doyle and G. A. Aggidis, "Development of multi-oscillating water columns as wave energy converters," *Renewable and Sustainable Energy Reviews,* vol. 107, pp. 75-86, 2019.
[30] M. Horko, *CFD optimisation of an oscillating water column wave energy converter*. University of Western Australia, 2007.
[31] C. Xu and Z. Huang, "Three-dimensional CFD simulation of a circular OWC with a nonlinear power-takeoff: Model validation and a discussion on resonant sloshing inside the pneumatic chamber," *Ocean Engineering,* vol. 176, pp. 184-198, 2019.
[32] M. Shalby, A. Elhanafi, P. Walker, and D. G. Dorrell, "CFD modelling of a small–scale fixed multi–chamber OWC device," *Applied Ocean Research,* vol. 88, pp. 37-47, 2019.
[33] A. Iturrioz, R. Guanche, J. Lara, C. Vidal, and I. Losada, "Validation of OpenFOAM® for oscillating water column three-dimensional modeling," *Ocean Engineering,* vol. 107, pp. 222-236, 2015.
[34] G. De Backer, "Hydrodynamic design optimization of wave energy converters consisting of heaving point absorbers," *Department of Civil Engineering, Ghent University: Ghent, Belgium,* 2009.
[35] R. Geer, R. Kaufman, A. Richards, R. Bostrom, and J. McAleer, "Background papers on seafloor engineering. Volume I. National needs in seafloor engineering," National Research Council, Washington, DC (USA). Committee on Seafloor …, 1975.
[36] N. Delmonte, D. Barater, F. Giuliani, P. Cova, and G. Buticchi, "Oscillating water column power conversion: A technology review," in *2014 IEEE Energy Conversion Congress and Exposition (ECCE)*, 2014: IEEE, pp. 1852-1859.
[37] J. L. Lye, D. T. Brown, and F. Johnson, "An investigation into the non-linear effects resulting from air cushions in the Orecon oscillating water column (OWC) device," in *International Conference on Offshore Mechanics and Arctic Engineering*, 2009, vol. 43444, pp. 779-789.
[38] A. F. Falcão, J. C. Henriques, and L. M. Gato, "Self-rectifying air turbines for wave energy conversion: A comparative analysis," *Renewable and Sustainable Energy Reviews,* vol. 91, pp. 1231-1241, 2018.
[39] D. G. Dorrell, M.-F. Hsieh, and C.-C. Lin, "A multichamber oscillating water column using cascaded savonius turbines," *IEEE Transactions on Industry Applications,* vol. 46, no. 6, pp. 2372-2380, 2010.
[40] W. Sheng, T. Lewis, and R. Alcorn, "On wave energy extraction of oscillating water column device," in *Proceedings of the Fourth International Conference on Ocean Energy (ICOE), Dublin, Ireland*, 2012, pp. 17-19.
[41] R. J. Bergillos, C. Rodriguez-Delgado, and G. Iglesias, *Ocean Energy and Coastal Protection: A Novel Strategy for Coastal Management Under Climate Change*. Springer Nature, 2019.
[42] M. Shalby, D. G. Dorrell, and P. Walker, "Multi–chamber oscillating water column wave energy converters and air turbines: A review," *International Journal of Energy Research,* vol. 43, no. 2, pp. 681-696, 2019.

[43] M. Delmonte, P. Ruol, L. Martinelli, F. Giuliani, and P. Cova, "Multi-chamber oscillating water column device for harvesting Ocean Renewable Energy," *Final report, user Project MORE,* vol. 21, p. 2014, 2014.
[44] J. R. Joubert, "Design and development of a novel wave energy converter," *Stellenbosch University, Faculty of Engineering, Doctor of Engineering Thesis,* 2013.
[45] A. F. Falcão and J. C. Henriques, "Oscillating-water-column wave energy converters and air turbines: A review," *Renewable Energy,* vol. 85, pp. 1391-1424, 2016.
[46] J. Fairhurst and J. Van Niekerk, "Development and application of a wave energy conversion simulation model," in *Proceedings of the 12th European Wave and Tidal Energy Conference. Cork, Ireland2017*.
[47] J. Fairhurst and J. L. Van Niekerk, "Modelling, simulation and testing of a submerged oscillating water column," *International journal of marine energy,* vol. 16, pp. 181-195, 2016.
[48] A. Babarit, "A database of capture width ratio of wave energy converters," *Renewable Energy,* vol. 80, pp. 610-628, 2015.
[49] D. Evans and R. Porter, "Hydrodynamic characteristics of an oscillating water column device," *Applied Ocean Research,* vol. 17, no. 3, pp. 155-164, 1995.
[50] K. Rezanejad, J. Bhattacharjee, and C. Guedes Soares, "Analytical and numerical study of nearshore multiple oscillating water columns," *Journal of Offshore Mechanics and Arctic Engineering,* vol. 138, no. 2, 2016.
[51] K. Rezanejad, J. Bhattacharjee, and C. G. Soares, "Stepped sea bottom effects on the efficiency of nearshore oscillating water column device," *Ocean Engineering,* vol. 70, pp. 25-38, 2013.
[52] H. Martins-Rivas and C. C. Mei, "Wave power extraction from an oscillating water column at the tip of a breakwater," *Journal of fluid Mechanics,* vol. 626, p. 395, 2009.
[53] H. Martins-Rivas and C. C. Mei, "Wave power extraction from an oscillating water column along a straight coast," *Ocean engineering,* vol. 36, no. 6-7, pp. 426-433, 2009.
[54] S. Zheng, Y. Zhang, and G. Iglesias, "Coast/breakwater-integrated OWC: A theoretical model," *Marine Structures,* vol. 66, pp. 121-135, 2019.
[55] G. C. Nihous, "Wave power extraction by arbitrary arrays of non-diffracting oscillating water columns," *Ocean engineering,* vol. 51, pp. 94-105, 2012.
[56] J.-R. Nader, S.-P. Zhu, P. Cooper, and B. Stappenbelt, "A finite-element study of the efficiency of arrays of oscillating water column wave energy converters," *Ocean Engineering,* vol. 43, pp. 72-81, 2012.
[57] J.-R. Nader, S.-P. Zhu, and P. Cooper, "Hydrodynamic and energetic properties of a finite array of fixed oscillating water column wave energy converters," *Ocean Engineering,* vol. 88, pp. 131-148, 2014.
[58] A. J. Sarmento and A. d. O. Falcão, "Wave generation by an oscillating surface-pressure and its application in wave-energy extraction," *Journal of Fluid Mechanics,* vol. 150, pp. 467-485, 1985.
[59] I. López, R. Carballo, F. Taveira-Pinto, and G. Iglesias, "Sensitivity of OWC performance to air compressibility," *Renewable Energy,* vol. 145, pp. 1334-1347, 2020.
[60] D. Konispoliatis and S. Mavrakos, "Hydrodynamic analysis of an array of interacting free-floating oscillating water column (OWC' s) devices," *Ocean Engineering,* vol. 111, pp. 179-197, 2016.
[61] D.-z. Ning, Y. Zhou, R. Mayon, and L. Johanning, "Experimental investigation on the hydrodynamic performance of a cylindrical dual-chamber Oscillating Water Column device," *Applied Energy,* vol. 260, p. 114252, 2020.
[62] B. Goeijenbier, J. Bricker, A. Antonini, G. Malara, M. Hendriks, and H. van der Ham, "Structural Optimisation and Behaviour of the Breakwater Integrated Oscillating Water Column Device: A combined 3D CFD and Structural FEM Analysis," *Journal of Coastal and Hydraulic Structures,* vol. 1, 2021.
[63] C. Wang and Y. Zhang, "Hydrodynamic performance of an offshore Oscillating Water Column device mounted over an immersed horizontal plate: A numerical study," *Energy,* vol. 222, p. 119964, 2021.
[64] A. Elhanafi, A. Fleming, G. Macfarlane, and Z. Leong, "Numerical energy balance analysis for an onshore oscillating water column–wave energy converter," *Energy,* vol. 116, pp. 539-557, 2016/12/01/ 2016, doi: https://doi.org/10.1016/j.energy.2016.09.118.
[65] E. Medina-Lopez, A. Moñino, R. J. Bergillos, M. Clavero, and M. Ortega-Sanchez, "Oscillating water column performance under the influence of storm development," *Energy,* vol. 166, pp. 765-774, 2019.
[66] T. Cabral *et al.*, "Performance assessment of a hybrid wave energy converter integrated into a harbor breakwater," *Energies,* vol. 13, no. 1, p. 236, 2020.

[67] P. Cong, B. Teng, W. Bai, D. Ning, and Y. Liu, "Wave power absorption by an oscillating water column (OWC) device of annular cross-section in a combined wind-wave energy system," *Applied Ocean Research,* vol. 107, p. 102499, 2021.
[68] F. Onea and E. Rusu, "The expected efficiency and coastal impact of a hybrid energy farm operating in the Portuguese nearshore," *Energy,* vol. 97, pp. 411-423, 2016.
[69] F. Onea and L. Rusu, "Coastal impact of a hybrid marine farm operating close to the Sardinia Island," in *OCEANS 2015-Genova*, 2015: IEEE, pp. 1-7.
[70] I. López, B. Pereiras, F. Castro, and G. Iglesias, "Performance of OWC wave energy converters: influence of turbine damping and tidal variability," *International Journal of Energy Research,* vol. 39, no. 4, pp. 472-483, 2015/03/25 2015, doi: https://doi.org/10.1002/er.3239.
[71] O. Saadatian, L. C. Haw, K. Sopian, and M. Y. Sulaiman, "Review of windcatcher technologies," *Renewable and Sustainable Energy Reviews,* vol. 16, no. 3, pp. 1477-1495, 2012.
[72] R. M. Kassir, "Passive downdraught evaporative cooling wind-towers: A case study using simulation with field-corroborated results," *Building Services Engineering Research and Technology,* vol. 37, no. 1, pp. 103-120, 2016.
[73] H. Montazeri, F. Montazeri, R. Azizian, and S. Mostafavi, "Two-sided wind catcher performance evaluation using experimental, numerical and analytical modeling," *Renewable Energy,* vol. 35, no. 7, pp. 1424-1435, 2010.
[74] P. Nejat, J. K. Calautit, M. Z. A. Majid, B. R. Hughes, and F. Jomehzadeh, "Anti-short-circuit device: A new solution for short-circuiting in windcatcher and improvement of natural ventilation performance," *Building and Environment,* vol. 105, pp. 24-39, 2016.
[75] F. Jomehzadeh, H. M. Hussen, J. K. Calautit, P. Nejat, and M. S. Ferwati, "Natural Ventilation by Windcatcher: A Review on the Impacts of Geometry, Microclimate and Macroclimate," *Energy and Buildings,* p. 110396, 2020.
[76] W. Sheng and A. Lewis, "Power takeoff optimization to maximize wave energy conversions for oscillating water column devices," *IEEE Journal of Oceanic Engineering,* vol. 43, no. 1, pp. 36-47, 2017.
[77] P. R. Teixeira, R. A. Gonçalves, and E. Didier, "A RANS-VoF Numerical Model to Analyze the Output Power of An OWC-WEC Equipped with Wells and Impulse Turbines in A Hypothetical Sea-State," *China Ocean Engineering,* vol. 34, no. 6, pp. 760-771, 2020.
[78] M. Stovall *et al.*, "Dose to the contralateral breast from radiotherapy and risk of second primary breast cancer in the WECARE study," *International Journal of Radiation Oncology* Biology* Physics,* vol. 72, no. 4, pp. 1021-1030, 2008.
[79] R.-S. Tseng, R.-H. Wu, and C.-C. Huang, "Model study of a shoreline wave-power system," *Ocean Engineering,* vol. 27, no. 8, pp. 801-821, 2000.
[80] E. P. Mansard and E. Funke, "The measurement of incident and reflected spectra using a least squares method," in *Coastal Engineering 1980*, 1980, pp. 154-172.
[81] D. Wang, M. Katory, and Y. S. Li, "Analytical and experimental investigation on the hydrodynamic performance of onshore wave-power devices," *Ocean Engineering,* vol. 29, no. 8, pp. 871-885, 2002.
[82] R. G. Dean and R. A. Dalrymple, *Water wave mechanics for engineers and scientists*. World Scientific Publishing Company, 1991.
[83] M. Folley and T. J. Whittaker, "Identification of non-linear flow characteristics of the LIMPET shoreline OWC," in *The Twelfth International Offshore and Polar Engineering Conference*, 2002: OnePetro.
[84] A. Mendes and W. M. Monteiro, "Performance analysis of a model of OWC energy converter in non-linear waves," 2007.
[85] S. L. Dixon and C. Hall, *Fluid mechanics and thermodynamics of turbomachinery*. Butterworth-Heinemann, 2013.
[86] A. d. O. Falcão and P. Justino, "OWC wave energy devices with air flow control," *Ocean engineering,* vol. 26, no. 12, pp. 1275-1295, 1999.
[87] A. A. Elmualim and H. B. Awbi, "Wind tunnel and CFD investigation of the performance of "Windcatcher" ventilation systems," *International Journal of ventilation,* vol. 1, no. 1, pp. 53-64, 2002.
[88] D. W. Etheridge and M. Sandberg, *Building ventilation: theory and measurement*. John Wiley & Sons Chichester, UK, 1996.
[89] A. CIBSE, "Natural ventilation in non-domestic buildings CIBSE Applications Manual AM10," ed: CIBSE Publications, 2005.
[90] M. E. McCormick, *Ocean wave energy conversion*. Courier Corporation, 2013.

[91] A. Brendmo, J. Falnes, and P. Lillebekken, "Lineår modelling of oscillating water columns including viscous loss," *Applied ocean research,* vol. 18, no. 2-3, pp. 65-75, 1996.
[92] T. Vyzikas, S. Deshoulières, O. Giroux, M. Barton, and D. Greaves, "Numerical study of fixed Oscillating Water Column with RANS-type two-phase CFD model," *Renewable energy,* vol. 102, pp. 294-305, 2017.
[93] W. Chen and W. Liu, "Numerical simulation of the airflow and temperature distribution in a lean-to greenhouse," *Renewable energy,* vol. 31, no. 4, pp. 517-535, 2006.
[94] D. Howe, J.-R. Nader, and G. MacFarlance, "Experimental analysis into the effects of air compressibility in OWC model testing," *AWTEC 2018 Proceedings,* p. 449, 2018.
[95] W. Sheng and T. Lewis, "Energy conversion: A comparison of fix-and self-referenced wave energy converters," *Energies,* vol. 9, no. 12, p. 1056, 2016.
[96] I. Simonetti and L. Cappietti, "The impact of modelling air compressibility in the selection of optimal OWC design parameters in site specific wave conditions," in *International Conference on Offshore Mechanics and Arctic Engineering*, 2019, vol. 58899: American Society of Mechanical Engineers, p. V010T09A041.
[97] C. K. Batchelor and G. Batchelor, *An introduction to fluid dynamics*. Cambridge university press, 2000.
[98] T. C. Rebollo and R. Lewandowski, *Mathematical and numerical foundations of turbulence models and applications*. Springer, 2014.
[99] J. Matsson, *An Introduction to ANSYS Fluent 2020*. SDC Publications, 2020.
[100] F. R. Menter, "Two-equation eddy-viscosity turbulence models for engineering applications," *AIAA journal,* vol. 32, no. 8, pp. 1598-1605, 1994.
[101] P. Sagaut, *Large eddy simulation for incompressible flows: an introduction*. Springer Science & Business Media, 2006.
[102] G. Alfonsi, "Reynolds-averaged Navier–Stokes equations for turbulence modeling," 2009.
[103] J. Hinze, "Turbulence. McGraw-Hill Publishing Co," ed: New York, 1975.
[104] E. A. Spiegel and G. Veronis, "On the Boussinesq approximation for a compressible fluid," *The Astrophysical Journal,* vol. 131, p. 442, 1960.
[105] P. Durbin, "A Reynolds stress model for near-wall turbulence," *Journal of Fluid Mechanics,* vol. 249, pp. 465-498, 1993.
[106] F. R. Menter, "Influence of freestream values on k-omega turbulence model predictions," *AIAA journal,* vol. 30, no. 6, pp. 1657-1659, 1992.
[107] A. Hellsten, "Some improvements in Menter's k-omega SST turbulence model," in *29th AIAA, Fluid Dynamics Conference*, 1998, p. 2554.
[108] A. Hellsten, S. Laine, A. Hellsten, and S. Laine, "Extension of the k-omega-SST turbulence model for flows over rough surfaces," in *22nd atmospheric flight mechanics conference*, 1997, p. 3577.
[109] P. Hu, Y. Li, C. Cai, H. Liao, and G. Xu, "Numerical simulation of the neutral equilibrium atmospheric boundary layer using the SST k-omega turbulence model," *Wind and Structures,* vol. 17, no. 1, pp. 87-105, 2013.
[110] T. P. Dhakal and D. K. Walters, "Curvature and rotation sensitive variants of the K-Omega SST turbulence model," in *Fluids Engineering Division Summer Meeting*, 2009, vol. 43727, pp. 2221-2229.
[111] A. Issakhov, "Modeling of synthetic turbulence generation in boundary layer by using zonal RANS/LES method," *International Journal of Nonlinear Sciences and Numerical Simulation,* vol. 15, no. 2, pp. 115-120, 2014.
[112] D. C. Wilcox, *Turbulence modeling for CFD*. DCW industries La Canada, CA, 1998.
[113] C. Hernandez, G. Beaupre, T. Keller, and D. Carter, "The influence of bone volume fraction and ash fraction on bone strength and modulus," *Bone,* vol. 29, no. 1, pp. 74-78, 2001.
[114] D. Quemada, "Rheological modelling of complex fluids. I. The concept of effective volume fraction revisited," *The European Physical Journal-Applied Physics,* vol. 1, no. 1, pp. 119-127, 1998.
[115] H. K. Esfeh, A. Azarafza, and M. Hamid, "On the computational fluid dynamics of PEM fuel cells (PEMFCs): an investigation on mesh independence analysis," *RSC advances,* vol. 7, no. 52, pp. 32893-32902, 2017.
[116] D.-Z. Ning, R.-Q. Wang, Q.-P. Zou, and B. Teng, "An experimental investigation of hydrodynamics of a fixed OWC Wave Energy Converter," *Applied energy,* vol. 168, pp. 636-648, 2016.